Chemodynamical Analyses of the Milky Way Satellites Sagittarius II and Aquarius II with GHOST: Challenges in Detecting Dark Matter in Ultra-Faint Systems

by

Dasha Zaremba
B.Sc., Kyiv-Mohyla Academy, Ukraine 2023

A Thesis Submitted in Partial Fulfillment of the
Requirements for the Degree of

MASTER OF SCIENCE

in the Department of Physics and Astronomy

University of Victoria
We acknowledge and respect the Lək̓ʷəŋən (Songhees and Xʷsepsəm/Esquimalt) Peoples on whose territory the university stands, and the Lək̓ʷəŋən and W̱SÁNEĆ Peoples whose historical relationships with the land continue to this day.

Chemodynamical Analyses of the Milky Way Satellites Sagittarius II and Aquarius II with GHOST: Challenges in Detecting Dark Matter in Ultra-Faint Systems

by

Dasha Zaremba
B.Sc., Kyiv-Mohyla Academy, Ukraine 2023

Supervisory Committee

Dr. Kim Venn, Supervisor
(Department of Physics and Astronomy)

Dr. Alan W. McConnachie, Departmental Member
(Department of Physics and Astronomy)

Dr. Julio F. Navarro, Departmental Member
(Department of Physics and Astronomy)

Dr. Holger Baumgardt, Outside Member
(University of Queensland)

ABSTRACT

Deep photometric surveys have revealed numerous faint Milky Way satellites with absolute V-band magnitudes $M_V \gtrsim -5$. Distinguishing whether these systems are dark matter-dominated ultra-faint dwarf galaxies (UFDs) or purely baryonic globular clusters (GCs) remains a key challenge. In this thesis, we explore the diagnostic power of detailed chemical abundances using high-resolution Gemini/GHOST spectra of five stars in two low surface brightness satellites – Sagittarius II (Sgr2) and Aquarius II (Aqu2). For Aqu2, the kinematics and metallicities of two stars support a dark matter-dominated UFD origin. The abundance patterns – low Na, Sr, Ba, and enhanced K – indicate inefficient star formation from only a few supernovae, possibly with enrichment from super-AGB stars. In contrast, Sgr2 shows unresolved velocity and metallicity dispersions, and its stars exhibit typical metal-poor abundance ratios with little spread. One exception is the discovery of an r-process-enhanced star (Sgr2584, [Eu/Fe] $= +0.7 \pm 0.2$), which does not clarify its nature, as such stars are found in both UFDs (Tuc III, Tuc IV, Grus II) and GCs (M15 and M92). However, radial mass segregation offers modest support for a GC classification. Motivated by this ambiguity, we examine the "Valley of Ambiguity" – the region below $M_V \lesssim -5$ in the size–luminosity (r_h-M_V) plane – by dividing it into five zones of shared properties. We identify observational caveats and propose diagnostics to address UFD–GC overlap in each. We argue that only a multi-faceted approach – combining kinematic (e.g., velocity dispersions of member stars, tidal streams kinematics), dynamical (e.g., tidal resilience, mass function slopes, detections of mass segregation), and chemical diagnostics (e.g., metallicity spreads, heavy elemental deficiencies, carbon enhancement) – offers the most robust path to classification. Coupled with N-body modeling, this strategy is essential for interpreting ambiguous systems in the era of large-scale photometric and spectroscopic surveys.

Contents

List of Tables

List of Figures

ACKNOWLEDGEMENTS

I would like to thank:

My Supervisor, Kim Venn, for her unwavering support, thoughtful mentorship, and for sharing both her wisdom and heart with me.

Mitacs Globalink, for giving me the opportunity to meet these incredible people three years ago, and for providing the funding that made this journey possible today.

The Armed Forces of Ukraine, for their continued resistance and for protecting my loved ones back home.

DEDICATION

To my friend Dmytro – a brilliant scientist whose path was cut short in defense of our country. I carry this milestone for both of us.

Chapter 1

Introduction

1.1 Galactic Archaeology: Reconstructing the Milky Way's Formation History

One of the central questions in modern astrophysics is how our Milky Way galaxy formed and evolved over cosmic time. The prevailing theoretical framework, the Lambda Cold Dark Matter (ΛCDM) cosmological model, predicts hierarchical structure formation – whereby large galaxies like the Milky Way grow through the successive accretion and disruption of smaller systems. As with any galaxy, the Milky Way consists of two fundamental components: baryonic (stellar) matter and non-baryonic (dark) matter. These accreted systems vary in their contributions to each component, ranging from luminous, star-forming dwarf galaxies to dark subhaloes devoid of stars.

The challenge lies in uncovering and interpreting these ancient "fossil records" in practice – to trace back the Milky Way's complex accretion history. Fortunately, these past mergers leave behind enduring spatial, chemical, and kinematic signatures, particularly within the stellar halo, where long dynamical timescales preserve the memory of progenitor orbits in phase space (Helmi & Tim de Zeeuw, 2000). As a result, the stellar halo acts as a fossil record of the Milky Way's assembly and a direct observational window into the nature of early, now-destroyed, dwarf galaxies (see e.g., Johnston et al., 2008; Helmi, 2008; Belokurov, 2013; Deason et al., 2015).

Reconstructing the Galaxy's past by studying the remnants of its progenitor systems lies at the heart of Galactic archaeology. The advent of the *Gaia* mission (Gaia Collaboration et al., 2016) – delivering precise all-sky astrometry, including stellar positions, parallaxes, and proper motions – together with wide-field spectroscopic

surveys such as APOGEE (Majewski et al., 2017), GALAH (Buder et al., 2021), and H3 (Conroy et al., 2019), has revolutionized our ability to probe the structure and substructure of the Milky Way. These datasets offer an unprecedented view into the kinematic and chemical properties of stars across the Galaxy (see review Deason & Belokurov, 2024).

Signatures of past accretion events are imprinted in features such as tidal streams, stellar debris, and dynamically and/or chemically distinct satellite populations (Helmi et al., 1999; Ibata et al., 2001; Belokurov et al., 2006; Nissen & Schuster, 2010; Myeong et al., 2018). By studying these components – especially the most ancient and least chemically evolved – we can directly explore the earliest epochs of galaxy formation (Freeman & Bland-Hawthorn, 2002; Tolstoy et al., 2009; Gallart et al., 2019).

Among the most informative of these relics are the Milky Way's satellite systems: globular clusters and dwarf galaxies. These objects offer complementary perspectives on the Galaxy's assembly history. Dwarf galaxies retain extended star formation histories and reside within substantial dark matter halos, contributing to the Milky Way's dark matter growth (Read et al., 2006; Tolstoy et al., 2009; Simon, 2019a). In contrast, globular clusters do not contribute to the Galactic dark matter halo, but reflect the conditions of early star formation (Kruijssen, 2015; VandenBerg et al., 2013). Additionally, those of accreted origin – which, according to different classification schemes, may constitute 40–60% of the Milky Way's globular cluster population (Massari, D. et al., 2019; Belokurov & Kravtsov, 2023) – serve as fossil records of their now-disrupted host galaxies.

In recent years, deep, wide-field photometric surveys such as the Sloan Digital Sky Survey (SDSS; York, 2000; Abazajian et al., 2009), the Dark Energy Survey (DES; Abbott et al., 2018), and the Panoramic Survey Telescope and Rapid Response System (PS1; Chambers et al., 2016) have significantly expanded the census of Milky Way satellites. Each successive survey has pushed the luminosity threshold lower, leading to the discovery of ultra-faint systems that occupy the transitional regime between globular clusters and dwarf galaxies. This growing overlap has driven the need for sharper observational and theoretical criteria to distinguish between the two classes.

In the following sections, I explore the differences between these systems and discuss why distinguishing them is crucial for understanding galaxy formation and evolution within a broader cosmological framework. I then summarize the key classification criteria – both theoretical and observational – before introducing the two

faint Milky Way satellites analyzed in this thesis as illustrative examples.

1.2 Milky Way Satellites: Star Clusters vs. Dwarf Galaxies

Our Milky Way galaxy hosts a number of companions, including two major groups of stellar systems: globular clusters and dwarf galaxies. Globular clusters are dense, spherical collections of stars, containing from about 10,000 to as many as one million stars. Currently, approximately 150 globular clusters associated with the Milky Way are known, most of which are concentrated toward the Galactic center.

Although their formation pathways and environments are not fully understood or universally agreed upon, globular clusters have been proposed to form within giant molecular clouds in host dwarf galaxies (McKenzie & Bekki, 2021). This implies that some of their properties (e.g., age, size, metallicity, metallicity dispersion) may depend on the characteristics of their host galaxies. While most globular clusters appear broadly similar, a few extremely dense and massive examples – such as M54, ωCen, and NGC2419 – stand out. These objects are thought to be remnant nuclei of former dwarf satellite galaxies (Mackey & van den Bergh, 2005; Cohen et al., 2011; Mucciarelli et al., 2012; Pfeffer et al., 2021).

Thus, although they may be related to globular clusters through a potential 'parenting' relationship, dwarf galaxies constitute a fundamentally different class of Milky Way satellites. Their defining feature is the presence of a dark matter halo. This contributes to their typically more dispersed and often elliptical appearance (shaped by a combination of tidal effects and the stabilizing influence of dark matter) and enables them to remain gravitationally bound with fewer stars.

According to the ΛCDM model, their formation traces back to the early Universe, when the first dark matter overdensities began to emerge. Through subsequent accretion and merger events, these initial overdensities grew into larger dark matter halos, within whose potential wells luminous matter became embedded (White & Rees, 1978). Given this hierarchical structure formation, the smallest galaxies (and, also, the faintest - which usually go hand in hand) serve as unique fossil records of the early Universe. Indeed, it has been shown that in the faintest (ultra-faint dwarf, UFD) galaxies , up to 80% of their stellar mass had already formed by redshift $z \sim 6$ (Sacchi et al., 2021). Altogether, this makes UFD galaxies the least chemically en-

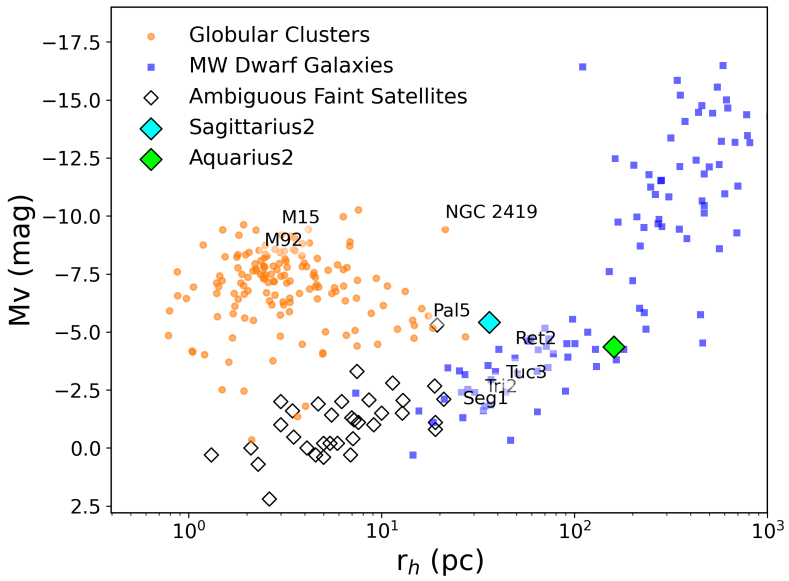

Figure 1.1: M_V vs. r_h diagram for Milky Way satellites. Globular clusters from Harris (2010) are plotted as orange circles, dwarf galaxies from McConnachie (2012) are shown as blue squares. Diamonds represent satellites with ambiguous classifications (see McConnachie & Venn 2020 and references therein, as well as Mau et al. 2020; Cerny et al. 2021; Gatto et al. 2021; Cerny et al. 2023a,b). Aqu2 and Sgr2 are depicted in lime and cyan, respectively.

riched, most dark matter–dominated, and oldest satellites of the Milky Way (Simon, 2019b).

The brightest representatives of both classes are easily distinguishable, even 'visually' (photometrically). As already mentioned, properties such as size, shape, and density can provide a good first-look estimate of a system's origin. To illustrate this, we show known Milky Way satellites in the size–luminosity plane (half-light radius, r_h, versus absolute V-magnitude, M_V) in Fig. 1.1.

As the figure shows, the separation between the two classes dilutes below $M_V \sim -5$ – a threshold that leads into the so-called *'valley of ambiguity'* (Gilmore et al., 2007) or *'trough of uncertainty'* (Conn et al., 2018), populated by 'ambiguous faint satellites.' The emergence of this new group of satellites has been made possible in recent years by significant advances in observational capabilities. In addition to the previously mentioned SDSS, DES, and PS1, more recent efforts such as DELVE (Drlica-Wagner et al., 2021), UNIONS (see Jensen et al., 2021; Smith et al., 2023), and Euclid (e.g., Hunt et al., 2024) have enabled the discovery of extremely faint Milky Way satellites with $M_V > -5$. In this faint regime, determining the true physical

nature of these systems remains challenging (e.g., UNIONS1/UMaIII, Smith et al. 2024; EridanusIII and DELVE1, Simon et al. 2024). Some of the new systems are likely UFDs, with $M_\star < 10^5 M_\odot$ (Simon, 2019b). Alternatively, some may represent (potentially disrupted) star clusters(e.g., Malhan & Ibata, 2018; Ji et al., 2020a; Li et al., 2022b; Martin et al., 2022).

1.3 Ultra Faint Dwarf Galaxies and Key Cosmological Questions

A natural question that arises is: why invest effort in classifying these faintest systems? Why not simply treat them as a distinct subclass of Milky Way satellites? The answer lies in their potential to address key cosmological questions that manifest on the smallest galactic scales.

The ΛCDM cosmological model has been remarkably successful in explaining cosmic structure across a wide range of redshifts, accurately reproducing the observed properties of galaxies, including their number counts, clustering, colors, morphologies, and evolutionary trends over time (Vogelsberger et al., 2014; Schaye et al., 2015). However, the agreement between simulation predictions and observations appears to break down on subgalactic scales (∼1 Mpc), giving rise to the so-called 'small-scale challenges' to the ΛCDM paradigm (Bullock & Boylan-Kolchin, 2017). Key questions include:

Missing satellites problem: The mass function of dark matter halos – describing the number density of halos as a function of mass – follows a steep power-law distribution, $\mathrm{d}n/\mathrm{d}M \propto M^{-1.9}$ (e.g., Moore et al., 1999; Jenkins et al., 2001; Gao et al., 2004; Tinker et al., 2008). This implies that low-mass halos vastly outnumber their more massive counterparts, a key prediction of the hierarchical structure formation scenario within the ΛCDM framework. However, N-body simulations predict an overabundance of low-mass dark matter subhalos relative to the number of known satellite galaxies. A possible explanation is that galaxy formation becomes increasingly inefficient in low-mass haloes. This leads to a fundamental question in galaxy formation: what is the minimum halo mass capable of hosting a luminous galaxy – or put simply, how small can a galaxy be?

Too big to fail: This problem highlights not only the discrepancy in the number of low-mass satellites predicted by cosmological models versus those observed, but

also the puzzling absence of more massive, LMC-sized satellites. Why do galaxies fail to form in the most massive subhalos, while successfully forming in lower-mass dark matter satellites?

Cores versus Cusps: Cold dark matter (CDM) simulations predict that dark matter haloes form hierarchically and develop steep, centrally concentrated (cuspy) density profiles. A widely cited example is the Navarro–Frenk–White (NFW) profile (Navarro et al., 1996), characterized by a density scaling of $\rho \propto r^{\alpha}$ with $\alpha = -1$ near the center. Remarkably, the NFW profile emerged universally in dissipationless simulations, appearing independent of both cosmological parameters and mass scale. However, observational studies of dwarf galaxies have challenged this prediction, with some systems exhibiting flatter, constant-density cores instead of cusps (see, e.g., Walker & Peñarrubia, 2011). Investigating the inner density profiles of the smallest and most dark matter-dominated UFDs offers a unique testbed for addressing this discrepancy. Such studies help determine whether the observed cores arise from baryonic feedback processes or suggest the need for alternative dark matter models (for a review, see Del Popolo & Le Delliou, 2021).

The smallest galaxies also offer critical insights into the faint end of the galaxy luminosity function, allow us to test the persistence of known scaling relations for galaxies (e.g., luminosity–size, mass–metallicity; Kirby et al. 2013b), and provide stronger constraints on abundance matching between stellar and dark matter components at the lowest mass scales.

Moreover, these systems serve as exceptional laboratories for testing dark matter physics. As the most dark matter-dominated objects known, they exhibit the highest J-factors – a measure of the expected signal strength from dark matter annihilation – making them prime targets for indirect detection experiments and for placing meaningful constraints on the nature of dark matter particles (Martinez, 2015; Geringer-Sameth et al., 2015; Bonnivard et al., 2015b,a). The lowest-mass dark matter satellites are particularly valuable for testing models such as self-interacting dark matter and weakly interacting particle scenarios (see Nadler et al., 2021; Correa et al., 2021; Dalal & Kravtsov, 2022; Bechtol et al., 2022).

While UFDs offer unique leverage on dark matter physics, faint star clusters, though lacking (significant) dark matter content, are likewise valuable astrophysical probes. These low-luminosity stellar systems trace a different set of properties: they serve as sensitive indicators of their host galaxy's gravitational potential, assembly history, and early chemical enrichment processes (e.g., Kravtsov & Gnedin, 2005;

Mészáros et al., 2015; Gaia Collaboration et al., 2018; Li et al., 2019). As such, they provide complementary insight into galaxy evolution from the perspective of baryonic structure.

1.4 Discriminating Between Star Clusters and Dwarf Galaxies

1.4.1 Observable Proxies for Dark Matter Halo

Apart from their photometric properties, dwarf galaxies can be distinguished from globular clusters by either direct or indirect measurement of a dark matter halo. One approach to achieving this is by measuring their radial velocity dispersion, which is directly correlated with dark matter content (Willman & Strader, 2012; Walker et al., 2023). In rotating spiral galaxies, the circular velocity at a given radius provides a direct measure of the enclosed mass. However, in dwarf galaxies, ordered rotation is dynamically negligible. Instead, these systems are primarily supported against gravity by the random motions of their stars.

Wolf et al. (2010) demonstrated that in dispersion-supported stellar systems, the dynamical mass within the half-light radius can be estimated using the velocity dispersion:

$$M_{1/2} = 930 \left(\frac{\sigma_{los}}{\mathrm{km\,s^{-1}}}\right) \left(\frac{R_{1/2}}{\mathrm{pc}}\right) M_{\odot} \tag{1.1}$$

where σ_{los} is the line-of-sight (radial) velocity dispersion, and $R_{1/2}$ is the two-dimensional projected half-light radius[1]. In dark matter-dominated dwarf galaxies, the velocity dispersions are higher than in purely baryonic systems of similar luminosity, reflecting their elevated mass-to-light ratios.

Another useful indicator of a dark matter halo is the metallicity ([Fe/H]) dispersion – i.e., the spread in the average abundance of elements heavier than helium among the member stars of a system. Metallicity dispersion is associated with extended star formation and chemical evolution (e.g., Leaman, 2012; Hasselquist et al., 2021;

[1]In a later work, Errani et al. (2018) proposed a slightly modified estimator for the mass enclosed within 1.8 times the projected half-light radius: $M_{\rm est}(< 1.8R_h) \approx 3.5 \times 1.8R_h\, G^{-1}\langle\sigma^2_{\rm los}\rangle$. This expression yields results nearly identical to those of Wolf et al. (2010) for the mass within the 3D half-light radius. It is derived from the projected virial theorem and ensures that the estimate is independent of the velocity anisotropy.

Walker et al., 2023). In dwarf galaxies, deeper gravitational potentials – due to the presence of dark matter – enable them to retain the products of stellar feedback, thereby preserving signatures of self-enrichment in the form of significant metallicity spreads.

However, in the new exceptionally faint systems, the robustness of these measurements is challenging. This is primarily due to: (i) the small number of confirmed members, (ii) only a handful of stars bright enough for spectroscopic follow-up, (iii) limited precision in individual [Fe/H] and radial velocities, and (iv) potential velocity dispersion inflation caused by unidentified binaries (e.g., McConnachie & Côté, 2010). Additionally, *"microgalaxies"*, i.e., heavily stripped remnants of early accreted satellites, which can reach arbitrarily low luminosities (see Errani & Peñarrubia, 2020), could have such small velocity dispersions that they are indistinguishable from kinematically cold globular clusters – unless a precision of $<$100 m s^{-1} can be obtained (see Fig. 7 in Errani et al., 2024a).

1.4.2 Indirect Evidence for Dark Matter Halo

Given the critical role of the smallest galaxies in addressing key questions in cosmology, the faintest galaxies and galaxy candidates require a more complex approach to answering the question *"Is there a dark matter halo?"*. One alternative is to indirectly infer the presence of a dark matter halo by studying the stability of the stellar system within the Milky Way tidal field. This can be tested by comparing the system's average density:

$$\bar{\rho}_{\rm h} \approx \frac{M_\star}{(4\pi/3) r_{\rm h}^3} \ , \tag{1.2}$$

to the mean density of the Galaxy at the pericenter of the system's orbit:

$$\bar{\rho}_{\rm peri} = \frac{V_c^2}{(4\pi G/3) r_{\rm peri}^2} \ . \tag{1.3}$$

For a self-gravitating star cluster that lacks dark matter, these two densities are expected to be comparable. This can be further tested with complementary N-body modeling of individual systems with known orbital parameters (see Errani et al. 2024b for UNIONS1/Ursa MajorIII and Errani et al. 2022 for the stellar stream C-19). This method is particularly valuable when observational limits do not constrain the internal velocity dispersion sufficiently, or, where the internal velocity dispersion may

be inflated by the presence of binary stars. (e.g., Errani et al., 2024a,b).

Another approach is to examine stellar mass segregation, as expected in globular clusters due to energy equipartition, which redistributes stars based on their mass (Baumgardt et al., 2022).

Two-body relaxation and dynamical friction in a star cluster cause massive stars to lose their speed and therefore sink towards the centre of the cluster. Subsequently, as a result of striving for energy equipartition, the low-mass stars gain more speed enabling them to travel farther from the cluster centre. This is the mechanism through which dynamical mass segregation occurs (Bonnell & Davies, 1998) In contrast, dark-matter-dominated UFDs often have relaxation times exceeding a Hubble time, making significant mass segregation unlikely. The presence of dark matter alters the gradient of the gravitational potential well, making it less clumpy than in self-gravitating star clusters. Baumgardt et al. (2022) estimated that, by approximating the relaxation process as dynamical friction of stars against much lighter dark matter particles, the relaxation time scales approximately with the square root of the dark-to-luminous mass ratio:

$$t_{\rm relax} \propto \sqrt{\frac{M_{\rm DM}}{M_\star}}\,. \tag{1.4}$$

For a system with 1000 times more dark matter than stellar mass, this implies a relaxation time roughly 30 times longer than in a purely stellar system.

1.4.3 Chemical Differences

Detailed chemical analyses of the brightest stars in an UFD galaxy or faint star cluster can also be invaluable in exploring the nature of an ambiguous system. High-resolution spectroscopy enables robust metallicity measurements through numerous iron lines, and detailed chemistry can be used to search for distinguishing features.

In globular clusters, these may include specific star-to-star variations in light elements (C, N, O, Na, Mg, Al, and some s-process elements) due to multiple populations (Gratton et al., 2012; Bastian & Lardo, 2018). Although these systems typically exhibit negligible spreads in overall metallicity ($\sigma_{rv} < 0.1$ dex), they can show pronounced anticorrelations among specific light elements—products of hydrogen burning in asymptotic giant branch (AGB) stars via the CNO cycle, as well as the NeNa and MgAl chains. Stars enriched in Na and Al but depleted in O and Mg (Population II) are believed to have formed after those with more 'primordial'

abundance patterns (Population I).

Another potential distinguishing feature of GCs is the presence of a so-called metallicity floor: to date, no known Milky Way GC has been observed with a metallicity below [Fe/H] $\approx$ ˘2.5. This threshold likely reflects the minimum host galaxy mass and the maximum redshift required for GCs to form and survive (the formation pathway of GCs was discussed earlier in Sec. 1.1).

In UFDs, typical chemical signatures found to-date include low ratios of α-capture elements (e.g., O, Mg, Si, Ca), low ratios of some iron-group elements (e.g., Zn, Mn), low neutron-capture element abundances and/or ratios (e.g., Sr, Ba, and/or [Sr/Ba]), and carbon-rich stars (e.g., Venn et al., 2004, 2012; Berg et al., 2015; Frebel & Norris, 2015; Salvadori et al., 2015; Ji et al., 2019; Monty et al., 2020, 2024; Sitnova et al., 2021a; Tarumi et al., 2021; de los Reyes et al., 2022; Rossi et al., 2023; Lucchesi et al., 2024). These features collectively reflect the imprints of ancient star formation histories and early chemical evolution in the universe (Koposov et al., 2009; Starkenburg et al., 2013; Frebel & Norris, 2015). Carbon enhancement (defined as [C/Fe]$>$ 0.7) is thought to reflect the nucleosynthetic signatures of early generations of massive stars. This is the reason it is frequently observed in the most metal-poor stars (e.g., Lucatello et al., 2006; Norris et al., 2013; Salvadori et al., 2015; de Bennassuti et al., 2017). The marked deficiency of heavy neutron-capture elements ($<\sim$ 1 dex than seen in halo stars of comparable metallicity) may be attributed to limited impact of certain enrichment sources (e.g., massive rotating stars, electron-capture supernovae, metal-poor binaries), or to an initial mass function (IMF) skewed toward intermediate-mass stars in galaxies with low SFRs (Tarumi et al., 2021; Sitnova et al., 2021b). Although no single explanation is definitive, these scenarios may account for the distinctive abundance patterns observed in UFDs compared to GCs and MW halo. Notably, some stars in UFDs deviate from the general chemical trends, reflecting variations in star formation histories or enrichment pathways. This chemical diversity suggests that UFDs are, in general, less chemically homogeneous than GCs.

Overall, chemical abundances provide a powerful means of distinguishing between systems of different origins. While the interpretation of certain abundance patterns can be complex, the observed differences offer invaluable insights –particularly in cases where dynamical analyses are uncertain or potentially biased.

1.5 Case Study: Aquarius II and Sagittarius II

In this work, we focus on two low surface brightness Milky Way satellites: Sagittarius II (Sgr2) and Aquarius II (Aqu2). The position of these two systems are shown on the size-luminosity plane for MW satellites; see Fig. 1.1. Sgr2 presents an intriguing scientific case as it is positioned precisely between star clusters and dwarf galaxies ($M_V = -5.7$, $r_h = 36$ pc). On the other hand, Aqr2 stands out for its unusually large half-light radius relative to its faintness ($M_V = -4.4$, $r_h = 159$ pc).

Sgr2 was discovered by Laevens et al. (2015) in PS1, where it was identified as an old (12.5 Gyr), metal-poor ([Fe/H] = -2.20) dwarf galaxy candidate. A deeper photometric study with Magellan/Megacam (Mutlu-Pakdil et al., 2018) revealed structural parameters more consistent with a globular cluster classification. Using DEIMOS spectroscopy and the metallicity-sensitive, narrow-band photometry provided by the Pristine survey, Longeard et al. (2020, hereafter L20) measured a velocity dispersion $\sigma_{v_r}^{\rm L20} = 2.7^{+1.3}_{-1.0}$ km s^{-1} suggesting the presence of a low-mass dark matter halo and therefore the UFD scenario; however, they also found a very low metallicity dispersion $\sigma_{[Fe/H]}^{\rm L20} = 0.10^{+0.06}_{-0.04}$ dex. Subsequently, Longeard et al. (2021, hereafter L21) supplemented the L20 dataset with 19 new members identified with *VLT*/FLAMES spectroscopy. This revealed a lower velocity dispersion of $\sigma_{v_r}^{\rm L21} = 1.7^{+0.5}_{-0.5}$ km s^{-1}, consistent with that of MW globular clusters of similar luminosity. The metallicity dispersion of this latter dataset was unresolved at $\sigma_{[Fe/H]}^{\rm L21} < 0.20$ dex at the 95% confidence level. To date, Sgr2 is classified as an exceptionally large stellar cluster and an analysis by Errani et al. 2024b suggests that its high density contrasts with the Milky Way halo at pericentre (where the density of Sgr2 is $\bar{\rho}_{\rm h} \approx 3.7 \times 10^7 \frac{\rm M_\odot}{\rm kpc^3}$ vs. the density of the MW halo at pericentre, $\bar{\rho}_{\rm peri} = 1.0 \times 10^6 \frac{\rm M_\odot}{\rm kpc^3}$) such that Sgr2 would not be significantly affected by tidal perturbations, even without a dark matter halo.

Aqu2 is less ambiguous in its classification, yet still presents challenges. Discovered by Torrealba et al. (2016, hereafter T16) using *SDSS* and VST ATLAS photometry from Shanks et al. (2015) with *Keck*/DEIMOS spectroscopy, the system was initially classified as an UFD simply due to its large r_h. Using 9 spectroscopically confirmed member stars (including 5 BHB), T16 derived a systemic velocity $v_r^{T16} = -71.1 \pm 2.5$ km s^{-1}with a large velocity dispersion $\sigma_{v_r}^{\rm T16} = 5.4^{+3.4}_{-0.9}$ km s^{-1}, and $[{\rm Fe/H}]_{T16} = -2.3 \pm 0.5$ dex with no resolved metallicity dispersion. Bruce et al. (2023, hereafter B23) revisited these measurements using *Magellan*/IMACS spectroscopy for 8 RGB stars. They found a lower systemic velocity ($v_r^{B23} = -65.3 \pm 1.8$

km s^{-1}) and smaller velocity dispersion $\sigma_{v_r}^{\rm B23} = 4.7^{+1.8}_{-1.2}$ km s^{-1}, as well as slightly lower metallicity and metallicity dispersion ([Fe/H]$_{B23} = -2.57$ dex, with $\sigma_{[Fe/H]}^{\rm B23} = 0.36^{+0.2}_{-1.4}$ dex). Given these measurements, both groups classified the system as an very metal-poor and very dark-matter dominated UFD. B23 noted that two stars (Gaia DR3 2609109756631321472 and Gaia DR3 2609061687357323776, hereafter Aqu2472 and Aqu2776 respectively) dominated their results. Removing Aqu2472 lowered the velocity dispersion by nearly half to $\sigma_{v_r}^{\rm B23^*} = 2.7^{+1.6}_{-1.2}$ km s^{-1}, while excluding Aqu2776 reduced the metallicity dispersion by nearly 10x, to $\sigma_{[Fe/H]}^{\rm B23^*} = 0.04^{+0.08}_{-0.02}$ dex. The tidal resilience analysis by Errani et al. (2024b) reveals that without dark matter, Aqu2's mean density ($\bar{\rho}_{\rm h} \approx 1.2 \times 10^5 \frac{\rm M_\odot}{\rm kpc^3}$) closely matches the Milky Way's at pericentre ($\bar{\rho}_{\rm peri} = 1.4 \times 10^5 \frac{\rm M_\odot}{\rm kpc^3}$), which suggests that Aqu2 may show signs of tidal interaction.

Using high-resolution spectra from the newly commissioning *Gemini*/GHOST spectrograph (McConnachie et al., 2024; Kalari et al., 2024), we revisit the analyses of Sgr2 and Aqu2. Our targets include two previously confirmed members of Sgr2, one new member of Sgr2, and two of the brightest stars in Aqu2. Our objectives include: (i) refining constraints on the velocity and metallicity dispersions of these systems, (ii) performing a detailed chemical analysis for the first time in these two faint systems, and (iii) increasing the observational epochs per star to assess any binary characteristics. These endeavors are to contribute to the discussion on the classification of these ambiguous systems as dark matter dominated UFDs or faint stellar clusters.

Chapter 2

GHOST observations

The high-resolution spectra for the five targets were obtained during the GHOST commissioning run in June 2022. The observations were conducted using the standard resolution mode with 2x4 binning. Targets Sgr2656 and Sgr2936, as well as Aqu2776 and Aqu472, were observed simultaneously using the two integrated field units (IFUs). The observation of Sgr2584 was performed separately in single IFU mode. For more details on the observations per exposure, see the Appendix.

2.1 Overview of the GHOST Spectrograph

GHOST is a fiber-fed, high-resolution echelle spectrograph on the Gemini South 8.1-meter telescope. Covering a broad wavelength range from 347–1060 nm (optimized for 363–950 nm), GHOST enables detailed chemical abundance studies and precision radial velocity measurements (McConnachie et al., 2024; Kalari et al., 2024).

It operates in two modes: a standard-resolution mode ($R \approx 56{,}000$) for simultaneous dual-object observations within a 7.5 arcmin field, and a high-resolution mode ($R \approx 75{,}000$) for single-object observations. Light is coupled into the spectrograph via 1.2" integral field units, each equipped with microlens arrays that reformat the beam into pseudo-slits. These microlenses enhance fiber coupling efficiency, improve spatial uniformity, and stabilize the input illumination. A white-pupil design combined with dichroic beam splitters directs light into blue and red arms, each equipped with Volume Phase Holographic gratings and optimized CCD detectors (McConnachie et al., 2024). This configuration minimizes light losses and allows for efficient, simultaneous coverage of the broad wavelength range .

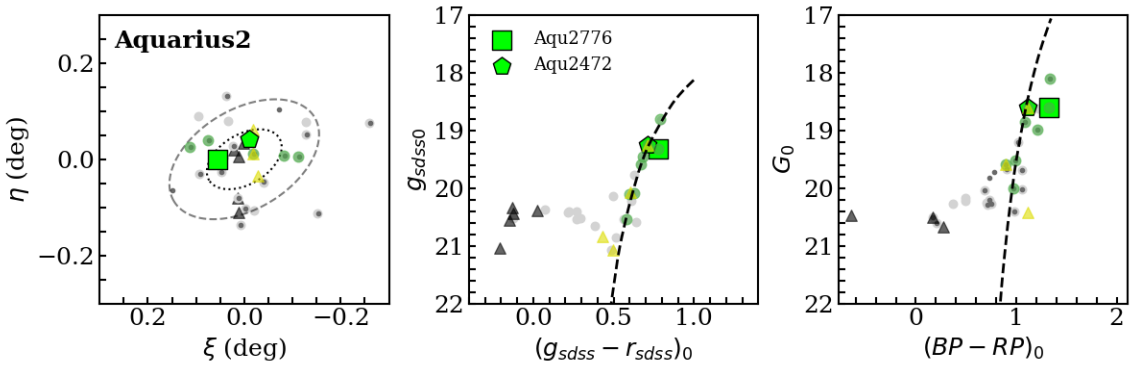

Figure 2.1: Spatial distribution (left; dotted and dashed ellipses indicate $2r_h$ and $3r_h$, respectively) and color-magnitude diagrams from SDSS (middle) and Gaia DR3 (right) photometry for Aqu2 member stars. Overlaid on the CMDs are Dartmouth isochrones of 12.5 Gyr and [Fe/H] $= -2.5$. Yellow triangles represent members identified by (Torrealba et al., 2016), with BHB stars in black. Green circles are members from (Bruce et al., 2023). Dark grey dots are stars with membership probability $P > 0.1$, selected using the algorithm described by (Jensen et al., 2024), while pale grey are stars from (Pace et al., 2022), also with $P > 0.1$, selected using DECaLS photometry. Targets analyzed in this paper are shown in larger lime markers.

GHOST features a simultaneous ThXe calibration source and active environmental control, enabling radial velocity precision of $\sim 1\tilde{}10$ m/s (McConnachie et al., 2024; Kalari et al., 2024). Commissioned in 2022, it has demonstrated the ability to achieve S/N ≈ 10 for $V \approx 20$ stars in one hour, making it well-suited for observations of UFDs and other low-luminosity systems (Kalari et al., 2024). Its dual-object capability in standard mode also increases observing efficiency (McConnachie et al., 2024). Finally, the deep blue sensitivity and sufficiently high S/N enable detection of key absorption lines from heavy elements, critical for tracing nucleosynthetic processes and chemical evolution in ancient stellar populations.

2.2 Target Selection

The targets were selected using a Bayesian inference method to identify highly probable members in UFDs, as described in (Jensen et al., 2024). The membership probabilities were estimated based on Gaia DR3 photometry and astrometry, considering projected spatial positions, systemic proper motion, and positions in the color-magnitude diagram (CMD) of the likely members. The Gaia DR3 source ID, RA, DEC, G, A_G, and BP-RP values for each target are presented in Table 2.1. The

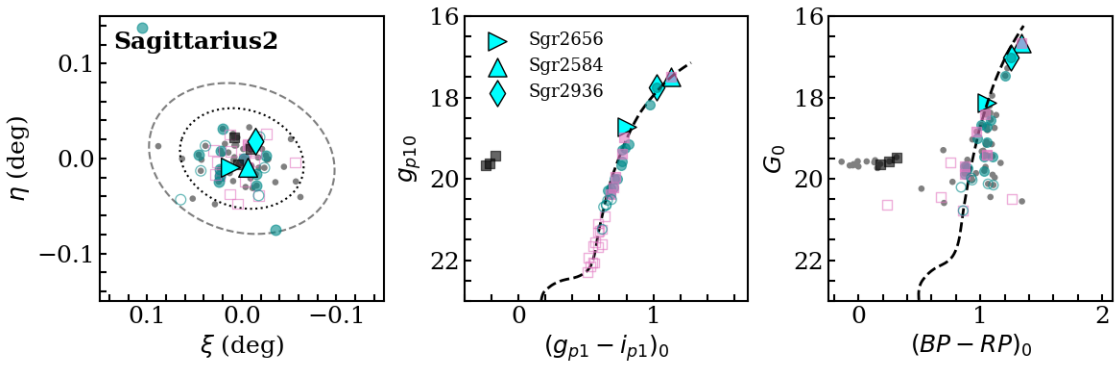

Figure 2.2: Spatial distribution (left; dotted and dashed ellipses indicate $2r_h$ and $3r_h$, respectively) and color-magnitude diagrams from PS1 (middle) and Gaia DR3 (right) photometry for Sgr2 member stars. Overlaid on the CMDs are Dartmouth isochrones of 12 Gyr and [Fe/H] $= -2.35$. Pink squares are from (Longeard et al., 2020), black for BHB stars; cyan circles from (Longeard et al., 2021). Open markers show stars with CaHK photometric metallicity only, solid markers indicate stars with spectroscopic metallicity from Ca triplet lines. Grey dots are high probability ($P > 0.5$) members identified with the algorithm described by (Jensen et al., 2024). Targets analyzed in this paper are highlighted with larger cyan markers.

Table 2.1: Members of Aqu2 and Sgr2 with GHOST spectra. Heliocentric distances are: Sgr2 at $73.1^{+1.1}_{-0.7}$ kpc (Longeard et al., 2020), Aqu2 at $107.9^{+3.3}_{-3.3}$ kpc (Torrealba et al., 2016).

Target	Gaia DR3 sourceID	RA	DEC	G	BPRP	A_G[1]	g_0[2]	r_0/i_0^b	pmra	pmdec
Aqu2776	2609061687357323776	338.5352	-9.3278	18.78	1.4	...	19.32	18.54	-0.446	-0.359
Aqu2472	2609109756631321472	338.4696	-9.2859	18.79	1.2	0.00	19.25	18.54	-0.552	-0.541
Sgr2584	6864047652495955584	298.1624	-22.0775	16.96	1.48	0.85	17.50	16.37	-0.704	-0.939
Sgr2656	6864047583776582656	298.1815	-22.0773	18.41	1.19	0.04	18.72	17.92	-0.837	-0.911
Sgr2936	6864423788550679936	298.1534	-22.0496	17.31	1.39	0.55	17.76	16.64	-0.852	-0.918

spatial positions of the targets, along with their locations on the CMDs are shown in Fig 2.1 and Fig 2.2. Similar way of selecting targets has been highly successful in selecting members without medium resolution spectroscopy (McConnachie & Venn, 2020; Sestito et al., 2023a; Waller et al., 2023; Hayes et al., 2023; Sestito et al., 2023b). In addition, these targets tested the faint limits of GHOST acquisitions and science exposures as well as the single and dual IFU target modes.

2.3 GHOST Data Reductions

The GHOST spectra were reduced using an early and developing version of the Gemini DRAGONS pipeline (see comments in Hayes et al., 2023). DRAGONS is a Python package that performs standard data reduction such as flat-fielding, bias subtraction, and corrections for heliocentric motion (Labrie et al., 2023). A full list of the GHOST data files used for the reduction of each target in Aqu2 and Sgr2 is provided in Table A.1.

For each camera, the DRAGONS pipeline produced 1D spectra for each exposure of each object. For each object, the exposures were then co-added by taking their median, per camera. This resulted in two (blue and red) 1D spectra for each object, with improved signal-to-noise ratios. The co-added spectra were continuum normalized by a two-step process. The first step estimates the continuum using median filtering and divide the spectrum by the estimated continuum. The second step would adjust the position of the continuum per wavelength via asymmetric k-sigma clipping, as the median filtering step underestimates the continuum in the presence of strong lines. Samples of the final spectra for all five targets are shown in Fig 2.3.

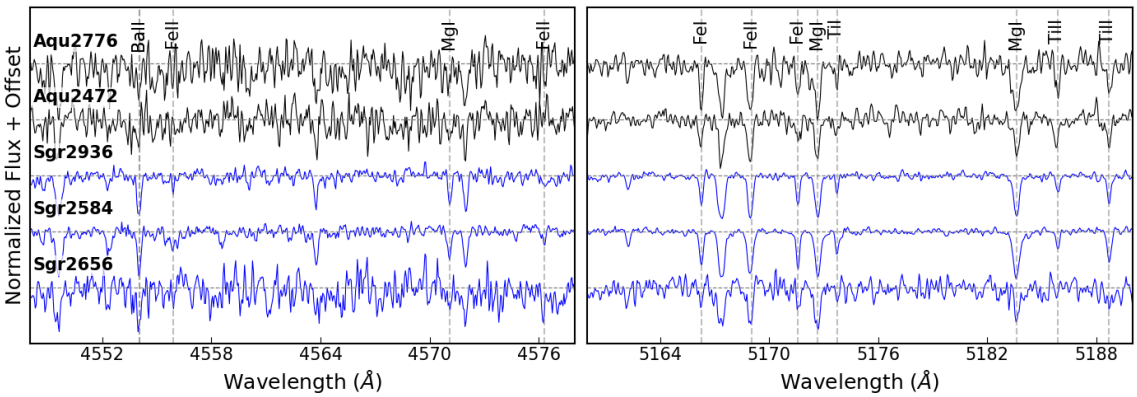

Figure 2.3: Samples of the GHOST spectra for our targets in Sgr2 and Aqu2, highlighting specific spectral lines (BaII λ4554, MgI λ4571, and the Mgb triplet).

2.4 Radial Velocities (v_r)

Radial velocities were determined using cross-correlation (IRAF/*fxcor*) with the GHOST spectrum of the standard star HD 122563, commonly used as a benchmark for metal-poor stars. The spectral region from 3800 to 6700 Å was used, as the SNR worsens at shorter wavelengths and the sky/telluric lines are poorly correlated at longer wavelengths. Our radial velocities per target are given in Table 3.1. The v_r for our GHOST spectrum of HD122563 is -26.3 km s^{-1} (see Hayes et al., 2023), in excellent agreement with Gaia DR3 and results in the literature. All target v_r are measured from template fitting using this standard star as a reference. We did not apply any zero-point corrections to the velocity measurements, as our derived values show excellent agreement with those obtained from other spectrographs for the same stars. GHOST's velocity precision – reaching meters per second (McConnachie et al., 2024; Kalari et al., 2024) – also surpasses that of comparable instruments.

Chapter 3

Method: New PY_LOOPER Notebooks

The spectral analysis was conducted using a new set of jupyter notebooks, `Py_Looper`[1], which offer a semi-automated routine for high-resolution spectral analysis based on equivalent widths (EW). This process starts by determining the metallicity ([Fe/H]) from iron lines, using an initial set of stellar parameters based on photometric calibrations (see Section 3.3). Spectral parameters ($T_{\rm eff}$, $\log g$, $\upsilon_{\rm mic}$, [M/H]) can be refined adopting both 1DLTE and 1DNLTE analyses. Subsequently, the routine measures other spectral lines, applying necessary corrections, including NLTE corrections from precalculated grids (see Section 3.6.2), and hyperfine structure corrections[2] (HFS) for odd-Z elements. Overall, this method includes error propagation from uncertainties in metallicity and the derived stellar parameters throughout the analysis. For the line measurement errors, we use the line-to-line scatter in Fe I for the other elements as this is a good indicator of impact of the SNR. To validate the `Py_Looper` method, we conducted a line-by-line comparison of EWs and abundances for Fe lines in the HD222925 standard star (see the Appendix) against the literature values reported by Roederer et al. (2018).

For measuring EWs, `PyLooper` employs a modified version of `pyEW`[3], which applies derivative spectroscopy to enhance weak signals and resolve blended lines. Higher-order derivatives narrow peak widths, making otherwise obscured features more distinct in derivative spectra[4] Yu et al. (2024) (and references therein). After identifying

[1] https://github.com/dashazaremba/PyLooper

[2] HFS corrections were calculated for odd-Z elements only. For elements where isotopic ratios depend on r/s-process dominance (e.g., Ba II, Eu II), HFS corrections were calculated directly from spectrum syntheses.

[3] https://github.com/madamow/pyEW

[4] Each derivative is calculated by dividing the difference between the original spectrum $f(\lambda)$ and a

lines, each fit is performed in small, user-defined spectral ranges around $\lambda \pm$ offset using either single-Gaussian, multi-Gaussian, or Voigt profiles.

`PyLooper` provides local continuum re-normalization through either an automated or manual process. In the automatic routine, a polynomial of a specified order is fit to the spectrum using the random sample consensus (RANSAC) method, which iteratively excludes outliers based on a threshold calculated from local noise. This process continues until the set of retained points stabilizes or a maximum number of iterations is reached. The spectrum is then normalized by dividing the flux by the fitted continuum. This method proved to be more effective for higher SNR spectra compared to our targets. For manual re-normalization, small local scaling adjustments are applied, raising or lowering the continuum by 2-5% at a time to achieve a more accurate best fit. In this analysis, Voigt profile fitting was disabled, and multi-Gaussian fits were applied only to blended lines. Most lines were fitted with a single Gaussian after manual continuum re-normalization (rescaling) within a wavelength range of ±3-5 Å. Abundances were then measured using the Python wrapper `q2` Ramírez et al. (2014) for MOOG (version 2019).

To reduce systematic errors, we compare results for our target stars to two standard stars with well-established stellar parameters, HD122563 and HD222925, which differ in metallicity and T_{eff}. The initial parameters were sourced from the literature Roederer et al. (2018); Giribaldi et al. (2023) and subsequently analyzed using the same methodology applied to our targets for consistency. The final stellar parameters with their associated uncertainties for the standards are presented in Table 3.1. The same Fe line list was used for both the standards and the targets. For other elements, the lines were first measured for the two standards, with only moderately strong and strong lines retained, as weaker lines could be too contaminated by noise in our spectra. This refined line list was then consistently applied to the target stars.

3.1 `Py_Looper` validation

To ensure that the new `Py_Looper` Jupyter notebooks provide reliable abundance measurements, a comparative analysis was conducted using the standard star HD 222925, focusing on Fe lines. The analysis included: (i) comparing EWs measured manually with IRAF to those measured with `Py_Looper`; (ii) comparing EWs re-

shifted version $f(\lambda+\Delta\lambda)$ by $\Delta\lambda$, yielding $\frac{df}{d\lambda}(\lambda+\frac{1}{2}\Delta\lambda)$. Higher derivatives are obtained by iterating this process the required number of times.

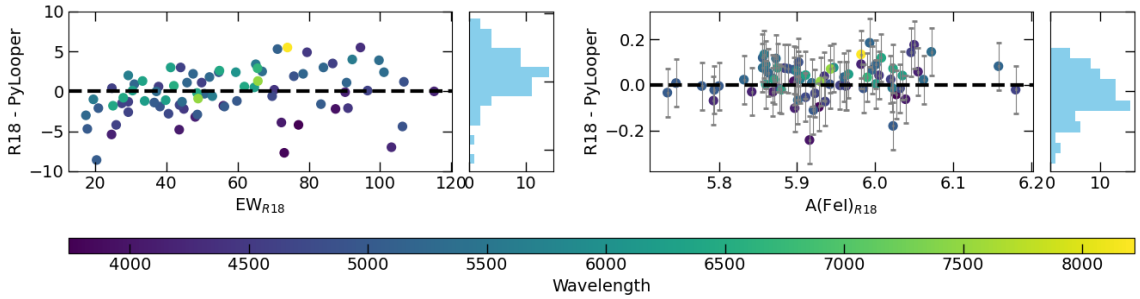

Figure 3.1: Line-by-line analysis of equivalent width (EW) measurements and derived abundances for FeI in HD222925, performed to validate the `Py_Looper` method. *Left*: Comparison of EWs measured using the `Py_Looper` notebooks with those reported by Roederer et al. (2018) (R18). *Right*: Absolute FeI abundances derived in this work vs abundances reported by R18. In this analysis, only lines with 20 <EW < 140 mÅ and EP > 1.4 eV were retained.

ported by Roederer et al. (2018) (R18) to those measured with `Py_Looper`; and (iii) comparing abundances derived with `Py_Looper`, including error analysis, to those reported by R18. All three tests demonstrated good agreement within $\sim 2\sigma$, with higher discrepancies observed at the bluest end due to the lower SNR of the GHOST spectrum in this region. `Py_Looper` proved to be much more efficient and consistent compared to manual measurements. A comparison of the FeI lines EWs and A(FeI) values with data from R18 are shown in Fig. 3.1.

3.2 Model Atmospheres Analysis

Chemical abundances are determined in this thesis from a classical model atmospheres analysis of the spectral features in each star. Model atmospheres from the MARCS website Gustafsson et al. (2008) were adopted, particularly the OSMARCS spherical models given that all the targets are giants, with log$g$ < 3.5.

The 1DLTE radiative transfer code MOOG[5] Sneden (1973); Sobeck et al. (2011) was used to convert EWs into chemical abundances and to perform spectrum syntheses.

[5]MOOG (2019) is available at `http://www.as.utexas.edu/~chris/moog.html`

3.3 Stellar Parameters

Surface temperatures (T_{eff}) were found using the colour-temperature calibrations for Gaia photometry from Mucciarelli & Bellazzini (2020). The input parameters include the *Gaia* DR3 de-reddened (BP−RP) colour and a metallicity estimate. The 2D reddening map[6] from Schlafly & Finkbeiner (2011) was used to correct the photometry for extinction[7]. As input metallicities, the mean [Fe/H] = −2.6 and −2.3 for Aqu2 and Sgr2 from Torrealba et al. (2016) and Longeard et al. (2020) were adopted, respectively.

Surface gravities were found using the Stefan-Boltzmann equation (Sestito et al., 2023a). This step required T_{eff}, the *Gaia* DR3 de-reddened G magnitude, bolometric corrections on the flux (Andrae et al., 2018), and a heliocentric distance[8]. A Monte Carlo algorithm was employed to propagate uncertainties in the input parameters and estimate the total and correlated uncertainties in the derived stellar parameters. The input uncertainties are as follows: 0.05 for the BP_RP color index, 0.5 dex for metallicity, 100 K for T_{eff}, and 1.0 kpc (Sgr2) and 3.3 kpc (Aqu2) for the distance. The input quantities were then randomised within 1σ each using a Gaussian distribution, except for the stellar mass. The latter is treated with a flat prior from 0.5 to 0.8 $M_{\odot}$, which is consistent with the mass of long-lived very metal-poor stars.

Initial microturbulence values were estimated using the calibrations for red giants in MW satellites by Mashonkina et al. (2017).

The stellar parameters from these calculations are listed in Table 3.1, and all targets with derived parameters are plotted on the Kiel diagram in Fig 3.2.

3.4 Spectral Lines Analysis

Our spectral analysis is based on the line list provided in the Appendix. This line list was compiled from our analyses of two standard stars, HD122563 (Venn et al., 2025) and HD222925 (Hayes et al., 2023). Spectral lines from a variety of sources (Yong et al., 2013; Norris et al., 2017; Kielty et al., 2021; Lucchesi et al., 2022; Roederer

[6] 2D reddening map at `https://irsa.ipac.caltech.edu/applications/DUST/`

[7] To convert from the E(B-V) map to *Gaia* extinction coefficients, the $A_V/E(B-V) = 3.1$ (Schultz & Wiemer, 1975) and the $A_G/A_V = 0.85926$, $A_{BP}/A_V = 1.06794$, $A_{RP}/A_V = 0.65199$ relations (Marigo et al., 2008; Evans et al., 2018) are used.

[8] Heliocentric distances are Sgr2 at $73.1^{+1.1}_{-0.7}$ kpc (Longeard et al., 2020), Aqu2 at $107.9^{+3.3}_{-3.3}$ kpc (Torrealba et al., 2016).

Table 3.1: Stellar parameters for the targets in Aqu2 and Sgr2, and two standard stars

Target	$T_{eff\ phot}$ (K)	$\log g_{\ phot}$ (cgs)	$T_{eff\ spec}$ (K)	$\log g_{\ spec}$ (cgs)	ξ ($km\,s^{-1}$)	$[Fe/H]_{LTE}$ (dex)	$[Fe/H]_{NLTE}$ (dex)	RV ($km\,s^{-1}$)
Aqu2776	4499 ± 78	1.23 ± 0.07	4499 ± 98	1.15 ± 0.25	1.6 ± 0.2	-1.87 ± 0.06	-1.80 ± 0.06	-64.34 ± 0.03
Aqu2472	4858 ± 94	1.46 ± 0.06	4858 ± 98	1.48 ± 0.30	2.4 ± 0.2	-2.66 ± 0.09	-2.52 ± 0.09	-55.98 ± 0.11
Sgr2656	4975 ± 100	1.72 ± 0.05	4975 ± 102	1.71 ± 0.20	2.2 ± 0.1	-2.35 ± 0.08	-2.23 ± 0.08	-177.33 ± 0.10
Sgr2584	4472 ± 77	0.87 ± 0.06	4472 ± 99	0.82 ± 0.30	2.2 ± 0.2	-2.36 ± 0.06	-2.24 ± 0.04	-176.18 ± 0.10
Sgr2936	4618 ± 83	1.12 ± 0.06	4618 ± 63	1.05 ± 0.28	2.4 ± 0.2	-2.47 ± 0.04	-2.36 ± 0.04	-175.70 ± 0.10
HD122563	...	...	4615 ± 28	1.30 ± 0.12	2.0 ± 0.1	-2.84 ± 0.01	-2.72 ± 0.01	-26.3 ± 0.1[9]
HD222925	...	...	5636 ± 99	2.54 ± 0.12	2.2 ± 0.1	-1.47 ± 0.01	-1.30 ± 0.01	-38.5 ± 0.1

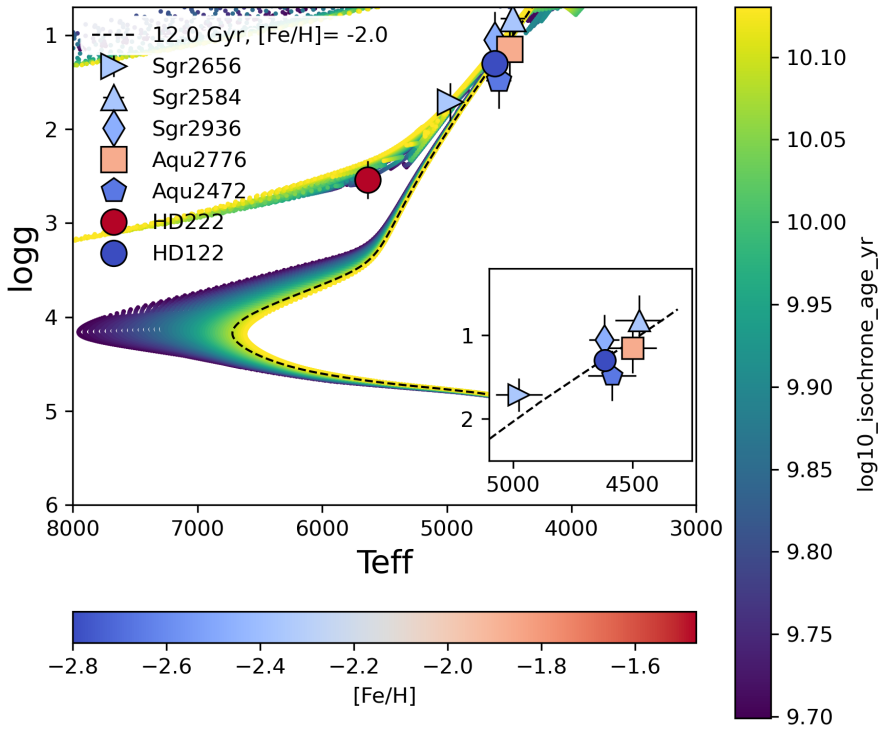

Figure 3.2: Aqu2 and Sgr2 targets with measured stellar parameters, along with two standards HD222925 and HD122563 used for differential analysis. Markers are color-coded by metallicity derived from LTE analysis of Fe lines. MIST isochrones span ages up to 13.5 Gyr at a fixed metallicity of [Fe/H] = -2. The dashed line is the 12 Gyr isochrone, the estimated age for Sgr2 (12 ± 0.5 Gyr, Longeard et al., 2020).

et al., 2022; Sestito et al., 2024) were examined in these standard stars and their equivalent widths (EWs) compared to those in the literature. All atomic data was adopted from the `linemake` compilation[10] Placco et al. (2021).

Our analysis is primarily an EW analysis, with spectrum synthesis included in two ways: (1) as a check on the line profile fit in each EW measurement, and (2) to calculate some blended line abundances (e.g., Eu) or carbon (e.g., CH from the G band). We note that strong lines with EW$>$ 150 mÅ were excluded from the 1DLTE abundances, except for certain species (e.g., NaI, KI, BaII, EuII) for which no weaker lines were available.

3.5 Metallicity [Fe/H]

FeI and FeII abundances were measured using both resonance and subordinate lines, with only those lines having equivalent widths in the range $20 < \mathrm{EW} < 150\,\mathrm{m\AA}$ retained. Initial stellar parameters for the MARCS model atmospheres were estimated from photometry, as detailed in Sec 3.3. Subsequently, the stellar parameters were refined based on iron lines spectroscopy. Specifically, v_{mic} was adjusted to flatten the slope of the absolute iron abundances, A(Fe), vs the reduced equivalent width ($\log\left(\frac{\mathrm{EW}}{\lambda}\right)$), using linear interpolation. Additionally, we examined the effect of adjusting $\log g$ to achieve ionization equilibrium between FeI and FeII lines in NTE analysis. For most targets, the $\log g$ values were kept nearly unchanged compared to the photometric estimates, as the Fe $\mathrm{I_{NLTE}}$ abundances were found to agree with the FeII abundances – which are not affected by NLTE – within $\pm 1\sigma$. However, the scatter was substantial, typically around 0.2–0.3 dex, due to the low SNR. The only exception was Aqu2776, where reducing $\log g$ by 0.07 improved the ionization equilibrium by 0.04 dex, and also reduced the scatter of some derived elemental abundances. Thus, we adopted this slightly lower $\log g$ value for Aqu2776. For Aqu2472, a 0.29 dex discrepancy was observed between the mean $\mathrm{FeI_{NLTE}}$ and FeII abundances. Increasing $\log g$ by 0.3 only reduced this discrepancy by 0.06 dex. Given the large intrinsic scatter (0.3 dex) among the Fe lines and that we only have 2 FeII lines for this star, we decided to retain the photometric $\log g$ value. T_{eff} was not adjusted in the spectroscopic analysis, as the slope of the linear interpolation of A(Fe) vs excitation potential (χ) was found to be flat (within the range 0.00 - 0.05) for all targets.

[10]Linemake available at https://github.com/vmplacco/linemake

Spectroscopic stellar parameter uncertainties were derived by adjusting each parameter with a Δ step (e.g., $T_{\rm eff} \pm \Delta T_{\rm eff}$, $\log g \pm \Delta \log g$, $v_{\rm mic} \pm \Delta v_{\rm mic}$), then recalculating iron lines statistics (absolute abundances A(FeI), A(FeII), the slopes `ep_slope`, `rew_slope`, ionization equilibrium of $\mathrm{A(FeI)_{NLTE}}$ and A(FeII)) at each step. Changes in these statistics were averaged for each parameter adjustment and propagated to determine parameter errors. Final uncertainties in metallicity were calculated by averaging the differences from these parameter adjustments and adding the statistical error from the iron lines in quadrature.

The final derived stellar parameters with uncertainties, as well as the weighted average metallicities from FeI and FeII lines (in both LTE and NLTE), are presented in Table 3.1 as:

$$[\mathrm{Fe/H}] = \frac{[\mathrm{FeI/H}]\cdot N_1 + [\mathrm{FeII/H}]\cdot N_2}{N_1+N_2}$$

$$\mathrm{err}_{[\mathrm{FeI/H}]} = \frac{\sigma_{\rm feh1}}{\sqrt{N_1}},$$

$$\mathrm{err}_{[\mathrm{FeII/H}]} = \frac{\sigma_{\rm feh2}}{\sqrt{N_2}},$$

$$\mathrm{err}_{[\mathrm{Fe/H}]} = \sqrt{\frac{\mathrm{err}^2_{[\mathrm{FeI/H}]}\cdot N_1 + \mathrm{err}^2_{[\mathrm{FeII/H}]}\cdot N_2}{N_1+N_2}}.$$

An example of the stellar parameter determination for the highest-SNR star in our sample, Sgr2936, is shown in Fig. 3.3.

3.6 Other Elements

Spectral lines of C to Eu are available for chemical abundance measurements in this sample. Some elements requires spectrum syntheses or additional corrections; e.g., due to isotopic splitting, hyperfine structure corrections, and/or NLTE corrections. We do not consider 3D effects in this thesis.

3.6.1 Isotopic & Hyperfine corrections

Isotopic and hyperfine structure corrections for odd-Z elements (ScI, MnI) were applied automatically within `PyLooper` routine (see Section **??**). For BaII and EuII, HFS corrections were determined through spectrum synthesis, adopting r-process isotopic ratios from Sneden et al. (2008).

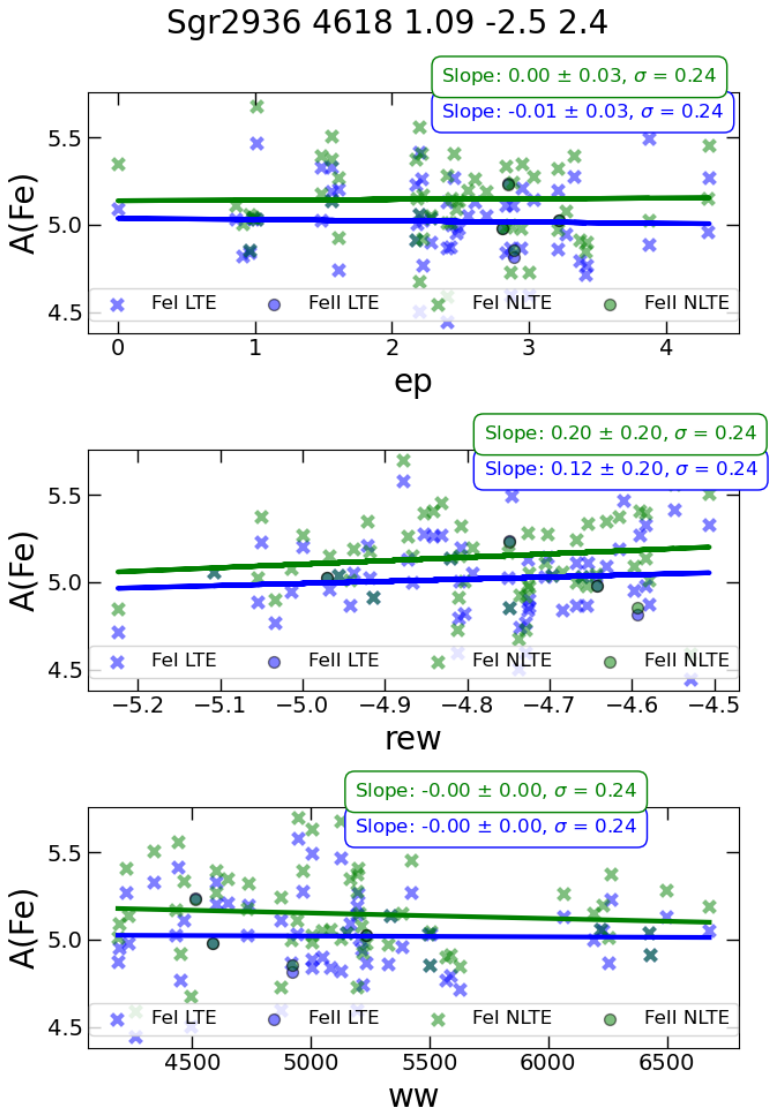

Figure 3.3: logϵ (absolute abundances, A) of Fe I (circles) and Fe II (crosses) lines used for the parameter determination of Sgr2936, shown as a function of excitation potential (top), reduced equivalent width (middle), and wavelength (bottom). Blue and green markers represent LTE and NLTE abundances, respectively. NLTE corrections were sourced from the INSPECT database as part of the `PyLooper` routine. The slope of the linear fit, as well as the scatter relative to the fitted line, is shown in each panel.

3.6.2 NLTE corrections

NLTE corrections for Ca, Mg, Ti, Mn, Si, and Fe are obtained from the MPIA webtool database[11]. Corrections for Na are from the INSPECT database[12] Lind et al. (2011). A python wrapper to extract these corrections for our stars is available[13]. For K, we apply the NLTE correction grid from Reggiani et al. (2019). Ba NLTE corrections are from Mashonkina & Belyaev (2019). All NLTE line corrections are presented in Table **??** (Fe lines) and Table **??** (other elements) in the Appendix.

The average NLTE abundances for each species are presented in Table 4.2. While not all elements have NLTE corrections, they are included nonetheless, as the Fe NLTE corrections contribute to their [X/Fe] ratios.

[11] http://nlte.mpia.de
[12] http://inspect-stars.com
[13] https://github.com/anyadovgal/NLTE-correction

Chapter 4

Chemical Abundances

In this chapter, we present the chemical abundances derived from spectra of five member stars across the two systems. Our analysis includes the application of non-local thermodynamic equilibrium (NLTE) corrections, hyperfine structure (HFS) and isotopic splitting corrections, and a comparison with other systems and MW halo stars from the literature.

Since different elements/groups of elements originate in distinct stellar environments and/or evolutionary phases, it is useful to categorize them based on common nucleosynthetic production sites. Comparing the abundances of each element group, as well as their abundance ratios both within the systems and relative to those of other UFDs/GCs and MW halo stars, provides valuable insights into the systems' chemical enrichment histories and, ultimately, their nature.

Chemical abundances below are compared to the Sun using standard notation $[X/Y] = \log n(X)/n(Y)_* - \log n(X)/n(Y)_\odot$, where n(X) and n(Y) are column densities (in cm^{-2}). We adopt the solar abundances from Asplund et al. (2009).

For comparison with Milky Way halo stars, we use abundance data from Roederer (2013); Roederer et al. (2014); Aoki et al. (2013); Yong et al. (2013, 2021); Li et al. (2022a).

We also compare to metallicities and chemistries of red giant stars in other dwarf galaxies; shown in Fig. 4.2. The UFD galaxies with literature abundance measurements are: Bootes I (Feltzing et al., 2009; Norris et al., 2010; Gilmore et al., 2013; Ishigaki et al., 2014; Waller et al., 2023), Bootes II (Ji et al., 2016), Carina II (Ji et al., 2020b), Carina III (Ji et al., 2020b), Cetus II (Webber et al., 2023), Coma Berenices (Frebel et al., 2010; Vargas et al., 2013; Waller et al., 2023), Grus I (Ji et al., 2019), Grus II (Hansen et al., 2020), Hercules (Koch et al., 2008; Adén et al., 2011; Vargas

Table 4.1: 1DLTE Abundances

	[X/Fe] $\pm \sigma_{err}(N_{lines})$				
species	Aqu2472	Aqu2776	Sgr2936	Sgr2584	Sgr2656
CH[1]	-0.16 ± 0.30	-0.32 ± 0.30	-0.22 ± 0.30	-0.21 ± 0.10	0.00 ± 0.50
NaI	-1.08 ± 0.35 (2)	-1.32 ± 0.26 (2)	-0.07 ± 0.20 (2)	0.08 ± 0.21 (2)	0.20 ± 0.41 (2)
MgI	0.39 ± 0.37 (3)	0.61 ± 0.39 (3)	0.69 ± 0.20 (3)	0.50 ± 0.17 (4)	0.20 ± 0.08 (2)
KI	0.79 ± 0.43 (2)	1.12 ± 0.21 (1)	0.51 ± 0.10 (1)	0.73 ± 0.16 (1)	< 0.91
CaI	0.59 ± 0.30 (5)	0.21 ± 0.19 (10)	0.43 ± 0.10 (10)	0.48 ± 0.12 (14)	0.69 ± 0.21 (8)
ScII	< 0.11	0.28 ± 0.43 (2)	0.26 ± 0.14 (4)	0.27 ± 0.24 (3)	0.36 ± 0.19 (3)
TiI	1.04 ± 0.48 (6)	-0.29 ± 0.25 (5)	0.33 ± 0.17 (9)	0.26 ± 0.23 (11)	0.60 ± 0.26 (4)
TiII	0.67 ± 0.14 (4)	0.81 ± 0.30 (4)	0.56 ± 0.11 (11)	0.71 ± 0.10 (14)	0.25 ± 0.24 (3)
VI	...	...	-0.23 ± 0.13 (1)	0.61 ± 0.24 (1)	...
CrI	-0.15 ± 0.49 (4)	-0.28 ± 0.29 (9)	-0.16 ± 0.15 (7)	0.00 ± 0.21 (11)	< 0.06
MnI	...	-0.67 ± 0.17 (1)	-0.28 ± 0.10 (1)	-0.22 ± 0.18 (2)	...
FeI	-2.66 ± 0.07 (19)	-1.88 ± 0.05 (31)	-2.48 ± 0.03 (59)	-2.36 ± 0.03 (42)	-2.35 ± 0.05 (23)
FeII	-2.89 ± 0.17 (2)	-1.63 ± 0.11 (5)	-2.48 ± 0.09 (4)	-2.23 ± 0.16 (5)	-2.10 ± 0.18 (3)
NiI	0.16 ± 0.53 (3)	-0.28 ± 0.15 (8)	0.25 ± 0.13 (7)	0.20 ± 0.14 (10)	0.19 ± 0.13 (2)
NdII	< 1.60	< 0.76	< 0.52	0.31 ± 0.08 (2)	< 1.83
ZnI	...	0.29 ± 0.10 (1)	0.44 ± 0.04 (1)	0.46 ± 0.04 (2)	...
SrII	< -1.58	< -2.10	0.08 ± 0.12 (1)	0.09 ± 0.06 (1)	0.37 ± 0.10 (1)
YII	< 0.07	...	0.03 ± 0.10 (1)	-0.18 ± 0.05 (1)	< 0.41
BaII	< -0.90	< -1.33	-0.13 ± 0.16 (3)	-0.14 ± 0.11 (4)	-0.26 ± 0.14 (2)
LaII	...	...	<0.92 ± 0.11 (1)	< 0.44 ± 0.07 (1)	< 1.39
EuII	...	...	< 0.30	0.65 ± 0.20 (2)	< 0.60

et al., 2013; François et al., 2016), Horologium I (Nagasawa et al., 2018), Leo IV (Simon et al., 2010; François et al., 2016; Vargas et al., 2013), Pisces II (Spite et al., 2018), Reticulum II (Ji et al., 2016; Hayes et al., 2023), Segue 1 (Norris et al., 2010; Frebel et al., 2014), Segue 2 (Roederer & Kirby, 2014), Triangulum II (Venn et al., 2017b; Kirby et al., 2017; Ji et al., 2019), Tucana II (Ji et al., 2016; Chiti et al., 2018; Chiti et al., 2023), Tucana III (Hansen et al., 2017; Marshall et al., 2019), Tucana V (Hansen et al., 2024), Ursa Major I (Waller et al., 2023), Ursa Major II (Frebel et al., 2010).

Measured LTE abundances for targets in both systems are presented in Table 4.1.

4.1 Carbon

Carbon abundances are determined by fitting the CH G-band (4290–4315 Å). A $^{12}C/^{13}C$ ratio between 6 and 11 was included in our synthetic spectra, consistent with values expected for stars at the tip of RGB Szigeti et al. (2018). To account for the evolutionary depletion of carbon, the [C/Fe] corrections from Placco et al. (2014) were applied to derive the natal carbon abundances. The uncertainties were estimated

Table 4.2: 1DNLTE Abundances

	[X/Fe]$_{\rm NLTE}$ $\pm$ $\sigma_{err}(N_{lines})$				
species	Aqu2472	Aqu2776	Sgr2936	Sgr2584	Sgr2656
CH	-0.30 ± 0.30	-0.39 ± 0.30	-0.33 ± 0.30	-0.33 ± 0.10	0.12 ± 0.50
NaI	-1.32 ± 0.35 (2)	-1.52 ± 0.26 (2)	-0.53 ± 0.20 (2)	-0.53 ± 0.34 (2)	-0.45 ± 0.41 (2)
MgI	0.32 ± 0.37 (3)	0.55 ± 0.39 (3)	0.54 ± 0.20 (3)	0.49 ± 0.17 (4)	0.21 ± 0.09 (2)
KI	0.48 ± 0.43 (2)	0.90 ± 0.21 (1)	0.16 ± 0.10 (1)	0.43 ± 0.16 (1)	< 0.54
CaI	0.45 ± 0.30 (5)	0.20 ± 0.19 (10)	0.41 ± 0.10 (10)	0.48 ± 0.12 (14)	0.73 ± 0.21 (8)
ScII	< -0.10	0.27 ± 0.43 (2)	0.12 ± 0.14 (4)	0.13 ± 0.24 (3)	0.23 ± 0.19 (3)
TiI	1.44 ± 0.48 (6)	0.28 ± 0.25 (5)	0.75 ± 0.17 (9)	0.77 ± 0.23 (11)	1.16 ± 0.27 (4)
TiII	0.55 ± 0.14 (4)	0.71 ± 0.30 (4)	0.48 ± 0.11 (11)	0.63 ± 0.10 (14)	0.14 ± 0.24 (3)
VI	...	...	-0.37 ± 0.13 (1)	0.48 ± 0.24 (1)	...
CrI	0.01 ± 0.49 (4)	-0.03 ± 0.29 (9)	0.15 ± 0.15 (7)	0.35 ± 0.21 (11)	< 0.28
MnI	...	-0.68 ± 0.17 (1)	-0.42 ± 0.10 (1)	-0.13 ± 0.18 (2)	...
FeI	-2.51 ± 0.07 (19)	-1.79 ± 0.05 (31)	-2.35 ± 0.03 (59)	-2.22 ± 0.03 (42)	-2.21 ± 0.05 (23)
FeII	-2.86 ± 0.17 (2)	-1.63 ± 0.11 (5)	-2.48 ± 0.09 (4)	-2.22 ± 0.16 (5)	-2.10 ± 0.18 (3)
NiI	-0.05 ± 0.53 (3)	-0.29 ± 0.15 (8)	0.11 ± 0.13 (7)	0.07 ± 0.14 (10)	0.06 ± 0.13 (2)
NdII	< 1.38	< 0.74	< 0.38	0.18 ± 0.08 (2)	< 1.71
ZnI	...	0.28 ± 0.10 (1)	0.30 ± 0.04 (1)	0.33 ± 0.04 (2)	...
SrII	< -1.79	< -2.12	-0.06 ± 0.12 (1)	-0.04 ± 0.06 (1)	0.25 ± 0.10 (1)
YII	< -0.14	...	-0.12 ± 0.10 (1)	-0.32 ± 0.05 (1)	< 0.29
BaII	< -1.11	< -1.34	-0.24 ± 0.16 (3)	-0.14 ± 0.15 (5)	-0.39 ± 0.20 (2)
LaII	...	...	<0.78 ± 0.11 (1)	<0.33 ± 0.07 (1)	< 1.27
EuII	...	...	< 0.19	0.53 ± 0.20 (2)	< 0.48

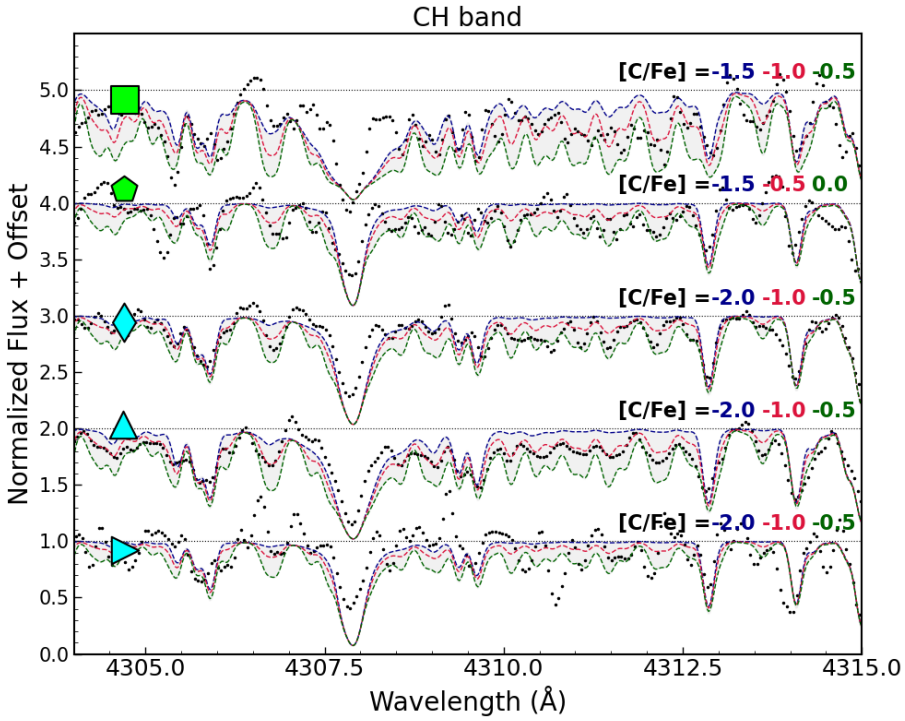

Figure 4.1: GHOST spectra of targets in Aqu2 and Sgr2, centered on the CH molecular band region. The colors represent synthetic spectra with varying [C/Fe] abundances, as indicated in the plots. The abundances shown are uncorrected for evolutionary effects

by varying the carbon abundances within ± 0.5 dex and examining synthetic fits; see Fig 4.1.

4.2 Alpha Elements (Mg, Ca, Ti)

The production of α-elements primarily occurs through core-collapse supernovae, with a smaller contribution to some from Type Ia supernovae (e.g., approximately 39% of Ca)Kobayashi et al. (2020).

The MgI, CaI, TiI, and TiII abundances in these stars are determined from a combination of strong resonance and weak subordinate lines. NLTE and HFS corrections help to reduce line-to-line scatter per element, however we still find an offset between TiI and TiII. This has been discussed as overly simple NLTE corrections and 3D stellar model effects by Mallinson et al. (2022). As these effects are expected to be smaller in the TiII lines, then we prioritize the use of TiII throughout the rest of

this analysis.

4.3 Odd-Z Elements (Na, K, Sc)

Odd-Z elements are excellent tracers of metal-poor core-collapse supernovae due to the odd-even effect in the predicted yields Heger & Woosley (2010); Nomoto et al. (2013); Kobayashi et al. (2020); Ebinger et al. (2020). We discuss the formation sites for Na and K in more detail in Section **??**.

Sodium abundances are derived from the two strong Na I D resonance lines near 5890 and 5895 Å, via EW and spectrum synthesis analyses. These lines typically exhibit strong NLTE departures: for Sgr2936/Sgr2656, Δ_{NLTE} for Na is -0.3/ -0.5, respectively. For Sgr2584, the value is smaller (-0.2), however we had to calculate the NLTE corrections with a higher logg value (by 0.2) due to unavailability in the NLTE parameters grid.

The Na I abundances in Aqu2 are extremely low when compared to other red giants in the MW halo and nearby dwarf galaxies; see Fig. 4.2. The more metal-poor star, Aqu 2472, has a very small NLTE correction (only $\Delta_{NLTE} = -0.03$), while the more metal-rich star, Aqu 2776, was slightly larger (-0.2). This latter value may be an overcorrection however as we had to increase EWs to be withihn the NLTE grid parameter space (i.e., 30 and 70 mÅ more) of INSPECT. Regardless of uncertainties in these NLTE Na corrections, the two targets in Aqu2 have remarkably low Na abundances. This is discussed further (below) in Section 5.2.1.

On the other hand, potassium in both Aqu2 and Sgr2 appears to be larger than in the MW halo red giants. The KI resonance line at 7699 Å has been corrected for NLTE effects. For Aqu2776, we also use the KI line at 7664 Å, however this line is blended with telluric in the other targets.

The ScII lines at 4324.996, 4415.557, 5031.01, 5526.77 Å have been corrected for isotopic and HFS corrections.

4.4 Iron-Peak Elements (Cr, Mn, Ni, Zn)

Iron-peak elements are synthesized during the thermonuclear explosions of Type Ia supernovae, as well as during incomplete or complete Si-burning in core-collapse supernovae Kobayashi et al. (2006). Abundances of Mn and Ni have recently been

reviewed as potential ways to identify MW halo stars that formed in dwarf galaxies de los Reyes et al. (2022).

MnI is determined from both resonance and subordinate lines, with both isotopic and HFS corrections.

Our CrI, MnI, and NiI look similar to the MW halo, to within errors. Possibly the higher metallicity star in Aqu2 shows slightly lower abundances.

We add ZnI to this discussion, determined from two lines at 4722 and 4810 Å. No corrections are applied, and it seems well correlated with other metal-poor stars in the MW and dGs (see Fig. 4.2).

4.5 Neutron-capture Elements (Sr, Ba, Eu)

Neutron-capture elements from through both slow and rapid neutron capture events (merging neutron star binaries and a range of Type II supernovae). Eu has been shown to be 98% r-process Simmerer et al. (2004), such that [Sr, Ba/Eu] can be used to examine the rise of the s-process in metal-poor galactic stars.

Europium has two naturally occurring isotopes ^{151}Eu and ^{153}Eu. Using the r-process isotopic fractions from Sneden et al. (2008), we synthesize Eu II lines at 4129.725 Å and 4205.04 Å. The strong Eu II lines at 4129 and 4205 Å are prominent in Sgr 2584, while only an upper limits are available from these lines in Sgr 2936. For Sgr 2656, which has the lowest SNR in the sample, the 4129 Å line is heavily contaminated by noise, so that the upper limit is estimated from only Eu II 4205 Å. The Eu II 4435 Å line is blended with Ca I 4435 Å throughout, so we exclude it from our analysis. The Eu II 6645 Å was too weak in our spectra to be detected.

The Ba II 4554 Å line is quite strong, and has significant isotopic shifts and HFS corrections that must be included. For Sgr2584, the HFS correction for this line is -0.2 dex, which brings it into better agreement with other Ba II lines at 5853, 6141, and 6496 Å. The Ba II 4934 line is blended with an iron line, so we excluded it from the analysis. The largest NLTE correction for Sgr2 members is observed for the line at 6496 Å, with a value of ~ -0.2 dex for all members, whereas for other lines, the correction is < -0.1 dex.

Sr II is determined from the two resonance lines at 4077 and 4215 Å, with no corrections applied.

The heavy element abundances in Aqu2 and Sgr2 (including sample spectrum syntheses) are discussed further in Sections 5.2 and 6.2.

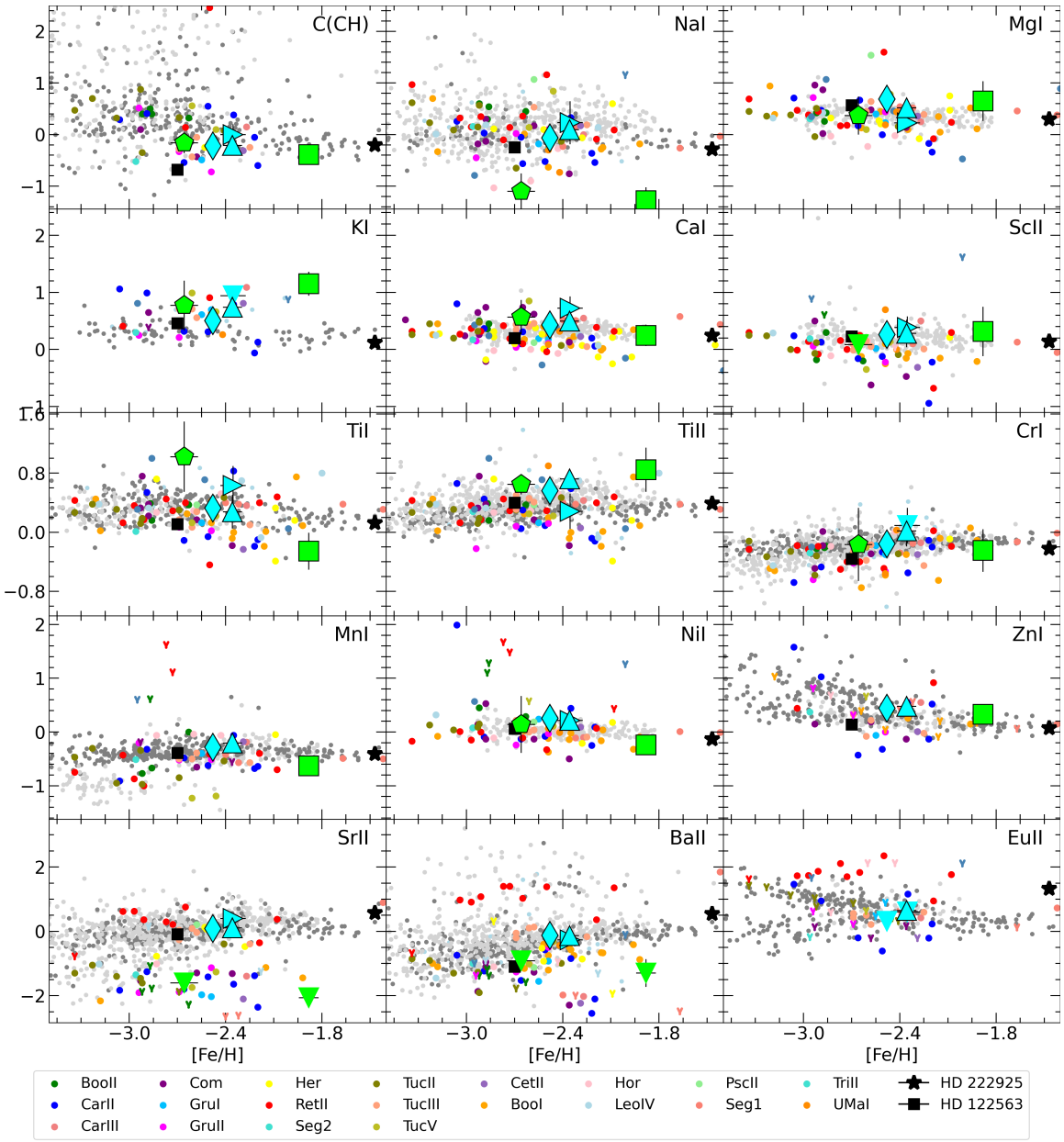

Figure 4.2: Derived 1DLTE abundances for Aqu2 (lime markers) and Sgr2 (cyan markers) compared to stellar abundances from the MW halo from Li et al. (2022a); Roederer (2013); Aoki et al. (2013); Yong et al. (2013, 2021) (light gray) and Roederer et al. (2014) (dark gray), and other UFD galaxies (colored dots according to legend, see text for references). Upper limits are marked with downward pointing triangles.

Chapter 5

Results for Aqu2

Our results for two stars in Aqu2 are compared to measurements from lower resolution spectra in the literature - specifically, Bruce et al. 2023 (B23) and Torrealba et al. 2016 (T16). Targets are shown in an isophotal contour map of Aqu2 in Fig. 5.1.

5.1 [Fe/H] and v_r dispersions

The two targets analyzed in this work were previously observed by B23, with one of them (Aqu 2472) also observed by T16. Our [Fe/H] and v_r measurements (see Table 3.1) for both stars show excellent agreement with those of B23, as illustrated in Fig 5.2. This agreement allows us to combine B23's data with our measurements for overlapping stars to derive systemic dispersions in [Fe/H] and v_r for Aqu2. Interestingly, both targets emerge as outliers, with Aqu2776 in metallicity and Aqu2472 in velocity.

For Aqu2472, the radial velocity is offset by $+9\ \mathrm{km\,s^{-1}}$ from the systemic velocity, consistent with the findings in B23. For Aqu2776, the radial velocity is also consistent with B23 and in good agreement with the other members; however, it is offset in metallicity by +0.6 dex above the systemic value. When compared to B23, we find no evidence for binarity (which may have affected these parameters), validating B23's results which were based on only a single exposure. B23 previously noted the substantial impact of Aqu2776 on the systemic metallicity dispersion of Aqu2, which decreases by a factor of 9 when this star is excluded. The elevated metallicity of Aqu2776 also accounts for the star's offset from the best-fit isochrone on both CMDs in Fig. 2.1. Contrary to B23's assumption, this deviation is not due to excess carbon,

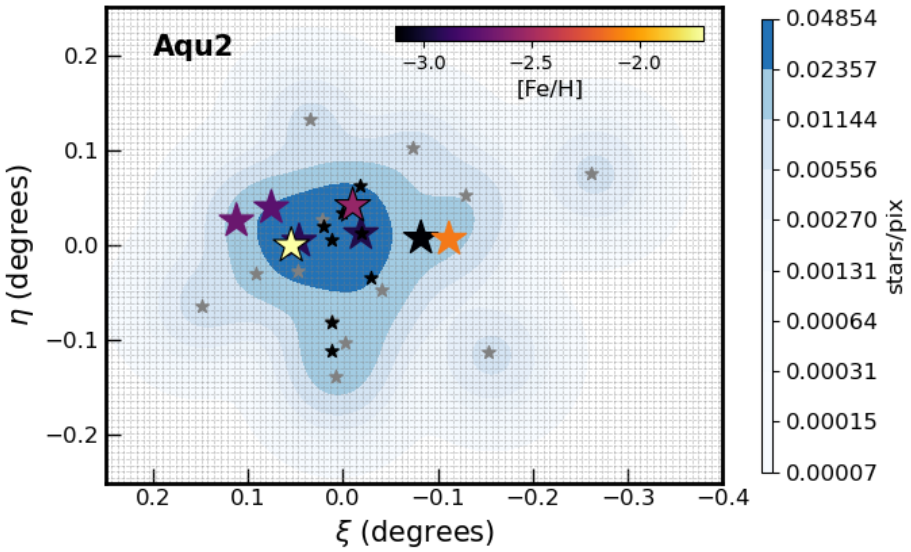

Figure 5.1: Isophote contour map of Aqu2, generated from the projected coordinates of member stars. Member stars are from Torrealba et al. (2016) (black), Bruce et al. (2023) (larger stars color-coded by metallicity), and member candidates from Jensen et al. (2024) with membership probability > 0.1 (grey). Targets from this study are also color-coded by metallicity, with black edges for distinction. The density of stars per pixel is represented by contour levels in shades of blue, with levels calculated logarithmically from approximately 0.0015 to the maximum density. The central surface brightness, based on the total magnitude, m_V, of 15.8, is approximately 26.0 mag arcsec^{-2}, while the outermost contour corresponds to a surface brightness of approximately 33.1 mag arcsec^{-2}. Each pixel in the map measures 0.5 arcmin $\times$ 0.5 arcmin, inferred from binning the projected coordinates (ξ, η) into a grid of 50 x 50 bins, shown with gray lines.

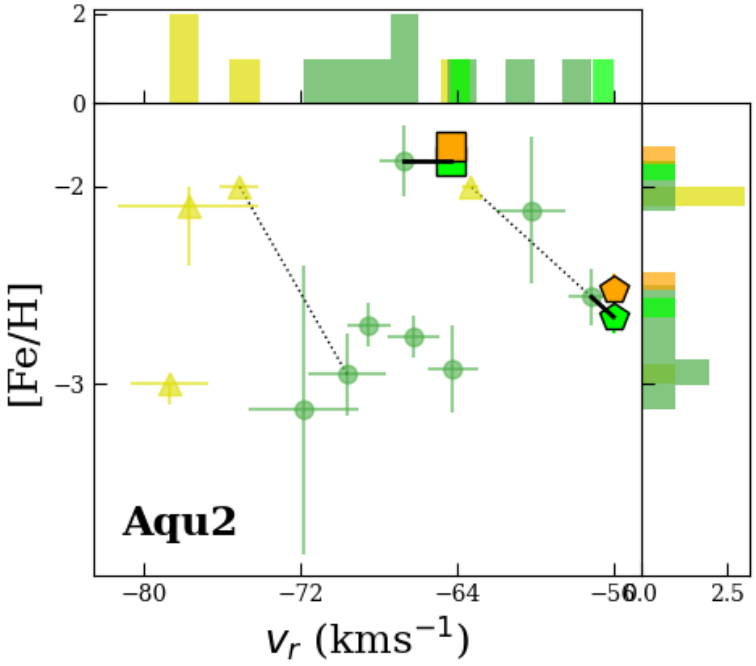

Figure 5.2: Radial velocity (v_r) and metallicity ([Fe/H]) distribution of Aqu2 members (Aqu2776/square, Aqu2472/pentagon). Yellow triangles represent data from T16 (excluding BHB stars), while green symbols indicate members from B23. Dotted lines connect overlapping stars between T16 and B23, and solid black lines highlight stars overlapping between our sample and B23. Lime/orange symbols are for our 1DLTE/NLTE metallicities.

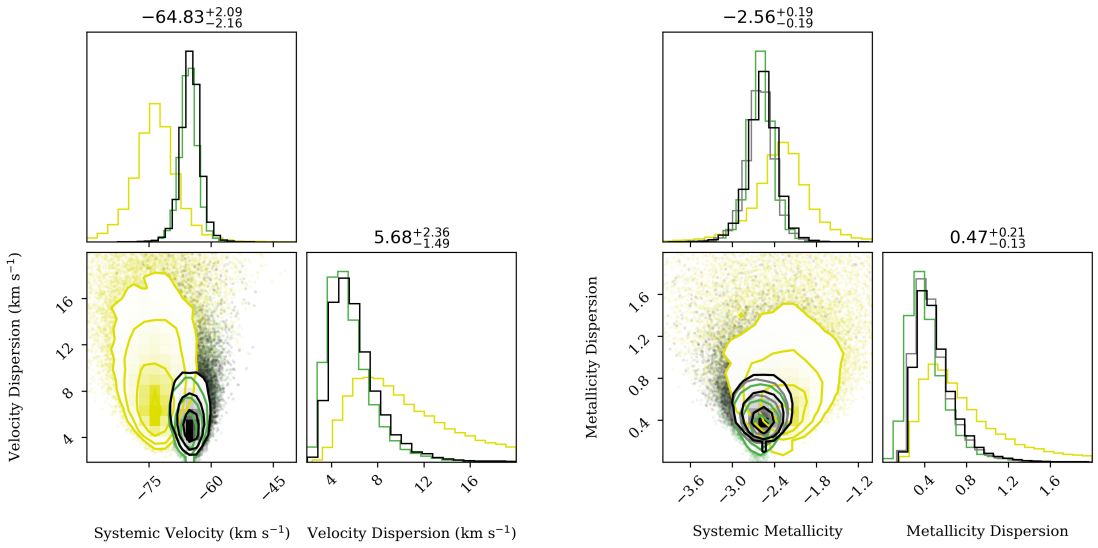

Figure 5.3: Two-dimensional joint PDFs of systemic velocity and metallicity with their dispersions for Aqu2, derived from running an MCMC sampler and likelihood function described in Section 5.1. Data from T16 (excluding BHB stars) is shown in yellow, and B23 data in green. Black represents the combined dataset from B23 and this work, with our measurements used for overlapping stars. In the metallicity panel, grey contours represent LTE, while black contours represent NLTE metallicities. The printed values correspond to the black PDFs

as we show in Section 4.1. Alternatively, we suggest this elevated [Fe/H] is due to inhomogeneous mixing in an unevolved UFD galaxy (see Section 5.2.1).

We recalculate the systemic velocity, $v_{\rm sys}$, and metallicity, $[{\rm Fe/H}]_{\rm sys}$, along with their dispersions σ_v and $\sigma_{\rm [Fe/H]}$, employing a Bayesian approach using Markov Chain Monte Carlo (Hastings (1970), MCMC) to sample from a posterior distribution of these parameters. The log-likelihood function is given by

$$\log \mathcal{L} = -0.5 \times \sum \left(\frac{({\rm value} - {\rm value_{sys}})^2}{\sigma^2} + \ln(\sigma^2) \right)$$

where "value" corresponds to either $v_{\rm sys}$ or $[{\rm Fe/H}]_{\rm sys}$, and $\sigma^2 = {\rm value}^2_{error} + \sigma^2_{\rm value}$. Uniform priors are applied to these parameters, constraining the systemic velocity between $-90 < v_{\rm sys} < -30$, systemic velocity dispersion between $0 < \sigma_v < 20$ km s^{-1}, metallicity between $-4 < [{\rm Fe/H}]_{\rm sys} < -1$, and metallicity dispersion from $0 < \sigma_{\rm [Fe/H]} < 2.0$. Any values outside these ranges are assigned $-\infty$ in the prior. The resultant posterior distribution functions (PDFs) for different data samples are shown in Fig. 5.3.

When combining this work with other targets from B23, our systemic velocity and velocity dispersion for Aqu2 are $v_{\rm sys} = -64.83^{+2.09}_{-2.16}$ km s^{-1} and $\sigma_v = 5.68^{+2.36}_{-1.49}$ km s^{-1}, in good agreement with B23. Similarly, our systemic metallicity and metallicity dispersion are $[{\rm Fe/H}]_{\rm sys} = -2.56 \pm 0.19$, and $\sigma_{\rm [Fe/H]} = 0.47^{+0.21}_{-0.13}$, which are also in excellent agreement with the values reported by B23. Finally, we note no significant difference in the systemic metallicity nor its dispersion when comparing measurements with and without NLTE corrections applied to our data.

5.2 Chemistry in Aqu2

The derived 1DLTE abundances for Aqu2 targets are shown in Fig. 4.2 in comparison to those of red giants in the MW halo and UFDs. Aqu2 has a clear metallicity range, one of our targets has [Fe/H] = -2.66, while the other is [Fe/H] = -1.87 dex. Yet the majority of the element ratios [X/Fe] resemble stars in the MWG. The most clear exceptions are low Na, Sr, Ba, and high K. These chemical features are similar to other unevolved UFDs with a “one-shot" enrichment event, i.e., where the Pop II stars retain the chemical yields of the initial Pop III supernovae, without subsequent pollution from Type Ia SNe or AGB stars (Frebel & Bromm, 2012). The intense feedback from core-collapse supernovae halts further star formation, leaving Pop II

stars with a unique chemical signature preserved in their atmospheres.

As an unevolved UFD, then the observed high [Fe/H] variation between our two stars could result from incomplete metal mixing, due to the rapid formation of Pop II stars at the center of the proto-galaxy. Indeed, both stars are located near the system's core, as shown by the isophotes in Fig 5.1. The disruption in the isophotes for this small system are also consistent with evacuation from supernova feedback in a shallow potential. Thus, the central positioning and brief Pop II star formation timescales support that the metallicity variations reflect gas inhomogeneities rather than late-stage chemical evolution.

Other examples of unevolved systems are Segue 1 (Frebel et al., 2014), Coma Berenices (Frebel et al., 2018; Waller et al., 2023), Hercules (Koch et al., 2008). In Fig. 5.4, we present the average abundances of Sr and Ba for selected UFDs, along with the predicted levels for unevolved systems. We highlight Segue 1 (in red) as an example of an unevolved system with a relatively large sample of spectroscopic members with detailed abundance measurements across a wide range of metallicities. This aligns with the suggestion by Ji et al. 2019 that low n-capture abundances can serve as a defining characteristic of the faintest dwarfs. Systems in Fig.5.4 that do not exhibit such deficiencies (Sgr2, Tuc III) will be discussed in the following sections.

We compare our chemical abundances for Aqu2472 to Population III model yields from Heger & Woosley 2010, 2012 update. In Fig. 5.5, an excellent fit was found when combining the yields from two Pop III SN using StarFit[1]. These two stars included an 18.4 $M_\odot$ SN with typical energy (2.4 x 10^{51} erg), combined with a 90 $M_\odot$ SN with excess energy (10 x 10^{51} erg), both with mild mixing fractions. Ti was excluded from the fit in Fig. 5.5, as its NLTE corrections may be insufficient (Mallinson et al., 2022, 2024);

including Ti increases the χ^2 value to 0.82. We note that our Ti abundance can be reproduced by including a third source, particularly with a significant r-process yield; however, the required additional model would also lead to an overproduction of Sr and Ba relative to our upper limit estimates, making such a scenario unlikely. For Aqu2776, none of the tested combinations of 2-3 Pop III SN yields provided a satisfactory fit (with $\chi^2 \geq 0.8$). Given its proximity to the system's center, as shown in Fig. 5.1, and its overall higher metallicity, we attribute this to enrichment from more Pop III stars, and most likely pollution from super-AGB stars (discussed below in Section 5.2.1).

[1]StarFit: https://starfit.org/

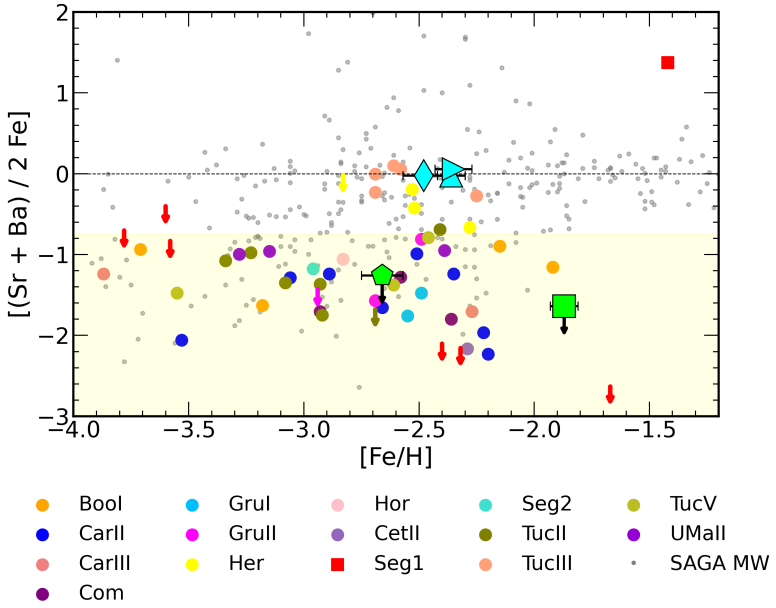

Figure 5.4: Average n-capture abundances, expressed as [(Sr + Ba)/2 Fe], plotted against [Fe/H] for selected UFDs and MW halo stars (references in Fig. 4.2). Upper limits for Aqu2 are indicated in lime, Sgr2 stars are in cyan, and Segue 1 is highlighted in red. The pale yellow region indicates the level predicted for unevolved systems Frebel & Bromm (2012), with [Sr/Fe] < -0.5 and [Ba/Fe] < -1.

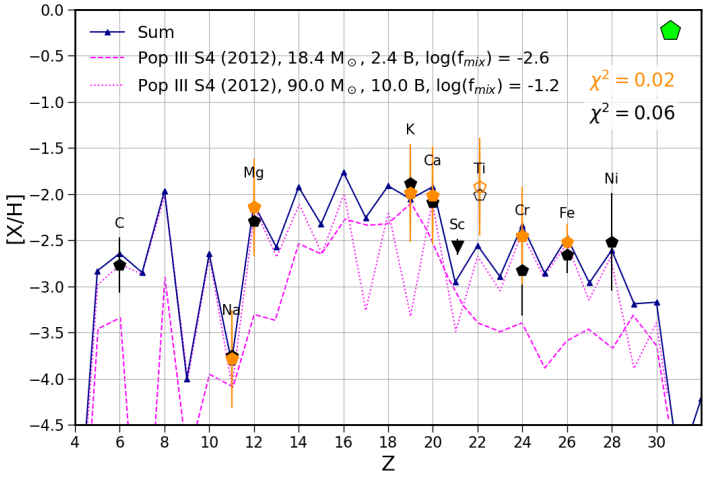

Figure 5.5: Chemical abundances in Aqu2472 are compared to Pop III models from Heger & Woosley (2010) (S4 with 2012 updates) using StarFit. The Aqu2472 1DLTE and NLTE abundances from Tables 4.1 and 4.2 are shown in black and orange, respectively, including the goodness of the fit (χ^2). Ti was not included in the fit (see text).

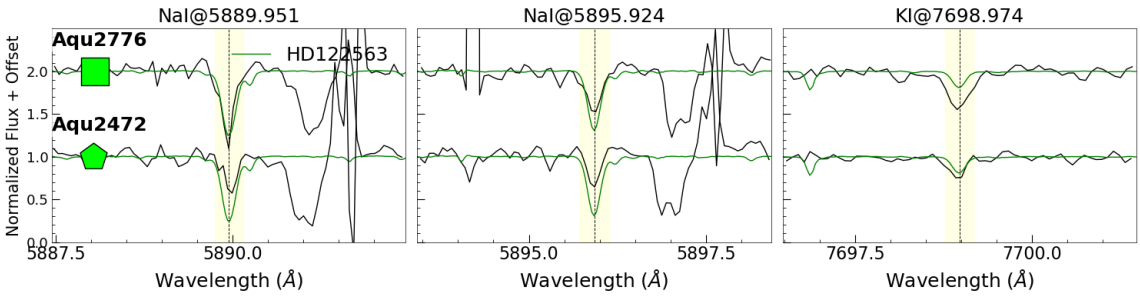

Figure 5.6: Comparison of the strong KI and weak NaD spectral lines for two stars in Aqu2 and the metal-poor standard star HD122563.

5.2.1 Element (anti-) correlations (K-Na)

Our 1DLTE abundances for the two targets in Aqu2 exhibit elevated K abundances alongside significantly depleted Na, which is a very unusual abundance pattern. To check these results, we directly compare the spectra of the NaD lines and the KI line at 7698 Å in the Aqu2 targets to the standard star HD122563, which has similar stellar parameters; see Fig. 5.6.

Clearly the NaD lines are weaker, particularly in the higher metallicity Aqu2472 star, and the KI line is stronger, particularly in Aqu2776 which has a similar metallicity to HD122563. There are no signs of contamination (telluric, interstellar, or dust shell).

The [K/Fe] in our two Aqu2 members is more closely aligned with stars in some UFDs than with stars in the MW halo, as seen in the K panel of Fig. 4.2.

Webber et al. (2023) recently suggested that enhanced K could serve as a distinguishing feature of UFD stars. This was based on a suggestion by Prantzos et al. (2018) that massive rotating stars may enrich K in such environments; however, they also cautioned that all of their models produce K at levels that are far lower than the solar abundance or MW halo stars. Therefore, the source of the high K in UFDs has not yet been clearly identified.

Alternatively, the unusual globular cluste NGC 2419 is notable for its substantial scatter in K abundances, reaching unprecedented values of [K/Fe]$\sim$ +2 dex (Cohen & Kirby, 2012; Mucciarelli et al., 2012); see Fig. 5.7. These high-K stars are found to be correlated with depleted Mg; i.e., a Mg-K anti-correlation.

Ventura et al. (2012) proposed that hot-bottom burning in stars of masses around 6 $M_{\odot}$ – at the edge between AGB and super-AGB (SAGB) regime – could reproduce the extreme potassium abundances in NGC 2419 if the standard cross section of Argon

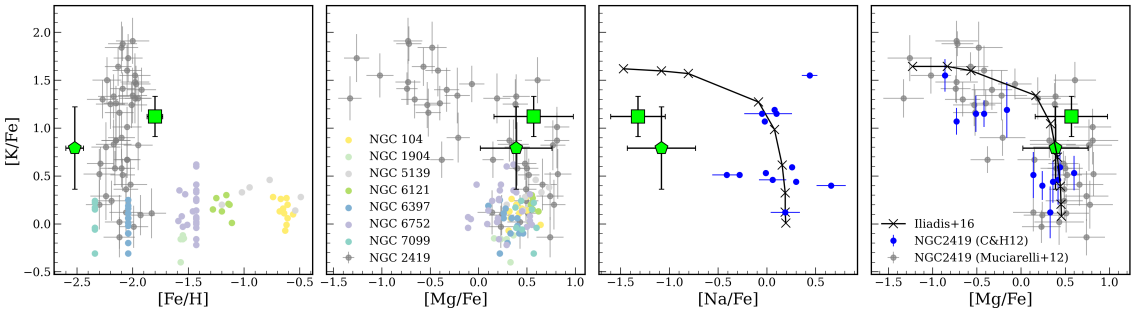

Figure 5.7: Comparison of [Na/Fe] and [Mg/Fe] vs [K/Fe] for the star cluster NGC 2419. 1DLTE abundances from Cohen & Kirby (2012) are shown in blue. Abundances from Mucciarelli et al. (2012), in grey, include a unique NLTE correction of -0.3 applied to K abundances. They did not apply a NLTE correction to Mg, which is predicted to be negligible for Mg-poor stars; however, 1DLTE Mg abundances may be overestimated by 0.2-0.3 dex for the Mg-rich stars. Other MW GC data is from Carretta et al. (2013). The black line illustrates the predictions obtained by mixing one part of processed matter with f parts of pristine matter in a one-zone nuclear reaction network by Iliadis et al. (2016) at constant temperature $T = 160$ MK, density $\rho = 900$ g cm^{-3}, and hydrogen mass fraction $X_{\rm H} = 0.7$; the crosses denote, from left to right, the abundances obtained with dilution factors of $f = 0.02$ (i.e., purely processed matter), 0.05, 0.1, 1.0, 3, 10, 30, 100, and 1000 (i.e., almost purely pristine matter).

nuclei in $^{38}\mathrm{Ar}(p,\gamma)^{39}\mathrm{K}$ reaction were increased by a factor of 100. In this model[2], the reduction of Mg and the production of K are maximized by also decreasing the mass loss rate by a factor of 4. By exploring a nuclear reaction network sensitive to variations in temperature, density, hydrogen abundance, reaction rates, and initial composition, Iliadis et al. (2016) identified that these abundance variations are limited to a narrow temperature-density range, achievable only by SAGB stars and classical novae.

In the right two panels of Fig. 5.7, we show [Na/Fe] and [Mg/Fe] vs [K/Fe] for stars in NGC 2419 from Mucciarelli et al. (2012) and Cohen & Kirby (2012), our 2 stars in Aqu2, and model results from Iliadis et al. (2016). While the data and models clearly show the K-Mg anti-correlation, an anti-correlation with Na is not clear. The star in NGC 2419 with the highest K also has the highest Na (third panel in Fig. 5.7). New observations of Na in the K-rich stars in NGC 2419 would help to constrain these models. Whether these models are applicable to Aqr2 is not currently clear, particularly as these models were developed for globular clusters and not ultra faint dwarf galaxies, e.g., the SAGB scenario for Aqu2 may be inconsistent with other observed abundance patterns in this system, which align more closely with a one-shot enrichment by Pop III star. Investigations into nucleosynthesis in other convective-reactive environments associated with massive stars – e.g., C and O shell mergers, which may also be induced by rotation Ritter et al. (2018) – could also explain high K abundances in UFDs.

Finally, K in Aqu2 is compared to stars in the globular clusters available in the APOGEE Value-Added Catalogue of Galactic globular cluster stars (Schiavon et al., 2023). As Na is not reliably measured from IR spectra of metal-poor RGB stars in APOGEE, then we examine Al (IR) as a proxy for Na; this is not ideal, however they are both odd-Z elements that participate in various stages of H-burning and show abundance variations in GC stars (Mészáros et al., 2015).

Fig. 5.8 illustrates the comparison of Na (Al) and K abundances in Aqu2 targets with those from optical studies of UFDs (Na, K) and those from IR studies of MW GCs (Al, K) from the APOGEE VAC. The comparison reveals that very high [K/Fe] abundances are present in some globular clusters. Notably, NGC 7078 (M15) which

[2]The SAGB model by Ventura et al. (2012) also predicts a modest increase in Na and a strong depletion in O, i.e., a weak Na-O anti-correlation similar to that observed in GCs.

The SAGB scenario has been further supported by recent high-precision measurements of the potassium-destroying reaction $^{39}\mathrm{K}(p,\gamma)^{40}\mathrm{Ca}$ Fox et al. (2024), which is critically sensitive to temperature-density conditions Dermigny & Iliadis (2017).

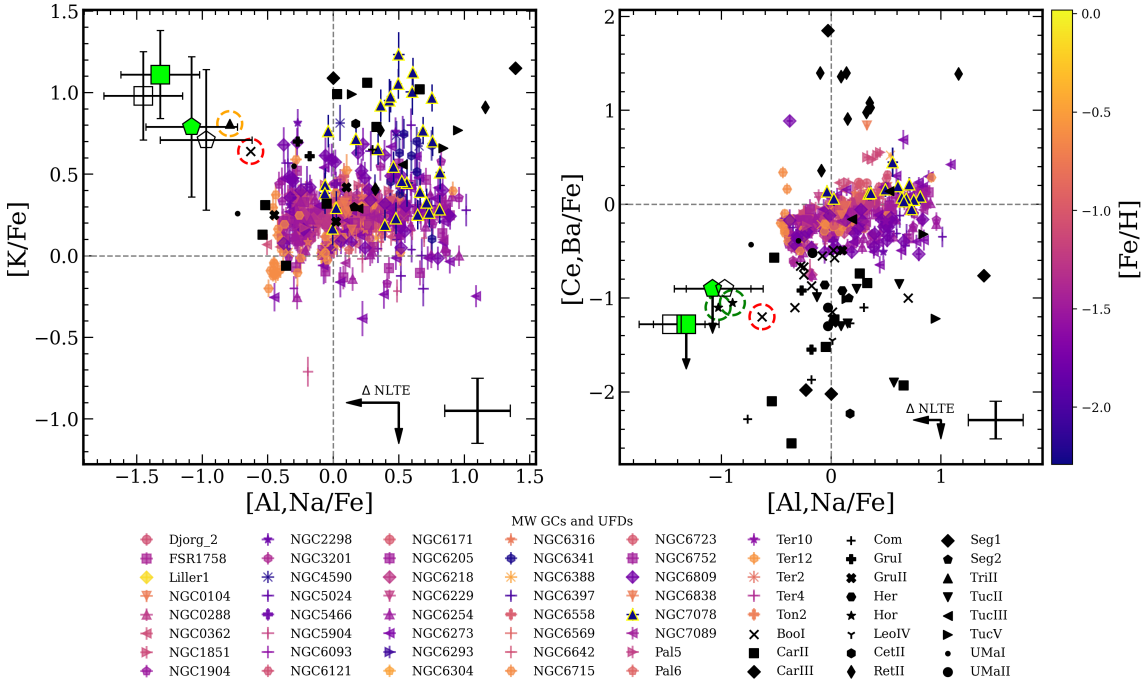

Figure 5.8: Comparison of Na (Al), Ba (Ce), and [K/Fe] in Aqu2 targets with those of stars in the Milky Way GCs and UFDs. GCs are from the APOGEE Value-Added Catalogue of Galactic globular cluster stars Schiavon et al. (2023) and are color-coded by their metallicity. Here, Al (IR) is used as a proxy for Na (opt), and Ce (IR) as a proxy for Ba (opt), based on the reliability of their abundance measurements and shared nucleosynthetic production sites. Only member stars with both velocity and proper motion probabilities greater than 0.5 are included. Outliers (iFLAG == 0) and non-giants (LOGG > 1.5) were excluded. To ensure reliable measurements, only APOGEE stars with SNR > 100 are shown, and abundance measurements were filtered using the following criteria: X_FE_ERR < 0.3 and X_FE_FLAG == 0. References for UFD abundances are as in Fig. 4.2. A representative uncertainty for UFDs is displayed in the bottom right corner, along with average NLTE corrections (K estimated from Reggiani et al. (2019), Na from Lind et al. (2011) and Ba from Mashonkina & Belyaev (2019)). NLTE abundances for our targets are shown with open markers. Highlighted with dashed, colored circles are other UFD members that exhibit similar abundance patterns (see text for details).

has a similar metallicity to Aqu2 and of course NGC 2419 (as shown in Fig. 5.7). As M15 is known to show variations in neutron-capture elements (Worley et al., 2013; Cabrera Garcia et al., 2024), we also examine [K/Fe] vs Ce (IR) or Ba (opt) in Fig. 5.8. Unfortunately, no systems have very similar abundance patterns to our two stars in Aqu2, where the low Na is poorly matched to most stars in both the UFDs (Na) and GCs (Al). The closest matching stars are: (i) one member in the Triangulum II UFD with high [K/Fe]= +0.8 and low [Na/Fe]= −0.8 (Venn et al., 2017b), (ii) one star in Bootes I with high [K/Fe]= +0.6, low [Na/Fe]= −0.6 and low [Ba/Fe]= −1.2 (Waller et al., 2023), and (iii) two stars in the Horologium I UFD with low [Na/Fe]= 0.1 and low [Ba/Fe]= −1, but lacking K measurements (Nagasawa et al., 2018). These stars are identified (circled) in Fig. 5.8.

We conclude that SAGB stars are the most likely source for the enhancements in K, anti-correlated with Mg, and potentially Na. This conclusion requires that the low n-capture abundances observed in Aqu2 from the "one shot" model include the Pop III yields, but limited yields from other (Pop II) massive stars, presumably due to SN feedback losses.

Chapter 6

Results for Sgr2

Our results for three stars in Sgr2 are compared to measurements from lower resolution spectra in the literature - specifically, Longeard et al. 2020 (L20) and Longeard et al. 2021 (L21).

6.1 [Fe/H] and v_r dispersions

The three targets in this paper have previous spectroscopic measurements by L20 (from DEIMOS) and L21 (from FLAMES), as shown in Fig. 6.1. Only two of our three targets were considered members of Sgr2 (Sg2936 and Sgr2584); however, we confirm the membership of all three stars (including Sgr2656).

For two targets, our radial velocity measurements (in Table 3.1) are in good agreement with those from L21; v_r within 0.5 $\sigma(v_r)$ for both Sgr2936 and Sgr2656. For Sgr2584, we find $v_r = -176.2 \pm 0.1$ km s^{-1}, which is in excellent agreement with our other two targets, but ~ 6 km s^{-1} lower than L20 ($v_r = -170.4 \pm 0.7$ km s^{-1}). Potentially Sgr2584 is a binary star. Similarly, our metallicity measurements (in Table 3.1) are in good agreement with the Ca II triplet metallicity estimates from L21; [Fe/H]$_{\rm NLTE}$ are within 1 σ([Fe/H]) for both Sgr2936 and Sgr2656. For Sgr2584, we find [Fe/H]$_{\rm NLTE} = -2.24 \pm 0.06$ ([Fe/H]$_{\rm LTE} = -2.36$), which is in excellent agreement with the other two targets, but ~ 0.15 dex lower than L20 ([Fe/H] $= -2.09 \pm 0.04$). Generally, our NLTE metallicities are in good agreement with those derived by L21 from CaT lines (only our LTE metallicities are ~ 0.2 dex lower). This good agreement enables us to combine the two samples (L21 + this work) without accounting for a zero-point offset between the instruments. Using our measurements for the overlap-

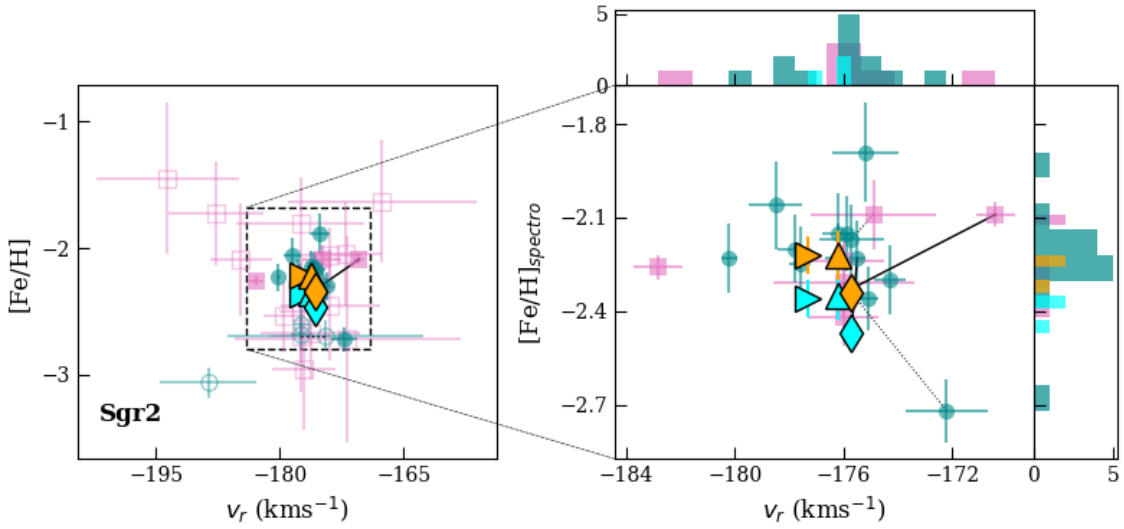

Figure 6.1: Radial velocity (v_r) and metallicity ([Fe/H]) distribution of Sgr2 members. Data from L20 and L21 are shown in pink and dark cyan, respectively. Open markers represent photometric members, and filled markers represent spectroscopic members, with one potential binary from the L20 sample excluded from the analysis. The right panel provides a zoomed-in view of the spectroscopic sample. Measurements from this work are plotted in light cyan (LTE) and orange (NLTE). Dashed lines connect the same objects between the L20 and L21 samples, while solid lines connect overlapping stars between this study and the L20, L21 datasets.

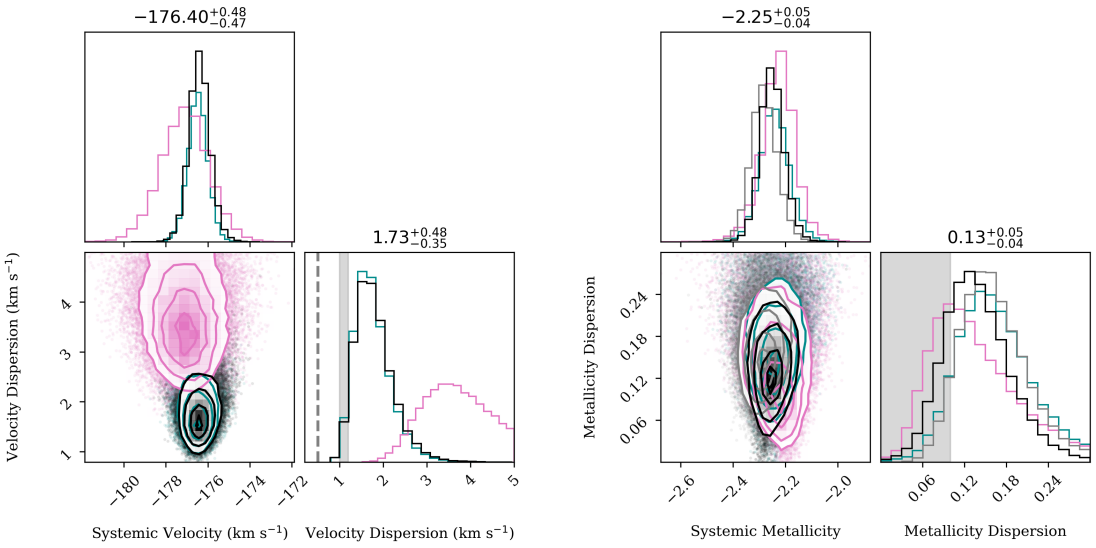

Figure 6.2: *Left*: Two-dimensional joint PDFs of systemic velocity and its dispersion for Sgr2. Pink and dark cyan show L20 and L21 samples, respectively. Black represents the combined L21 spectroscopic data with targets from this work; overlapping targets use measurements from this study. The grey band indicates the velocity dispersion expected under a purely baryonic scenario, based on the formalism of Wolf et al. (2010) (1.1 ± 0.1 km s^{-1}; Longeard et al. 2021). The grey dashed line represents the velocity dispersion derived from the N-body modeling of globular cluster velocity dispersion profile, calculated as described in Baumgardt (2017) (0.5 km s^{-1}). *Right*: Joint PDFs of systemic metallicity and its dispersion for Sgr2. Only spectroscopic members from L20 (pink) and L21 (dark cyan) were used. Grey shows combined L21 data with LTE metallicities of targets analyzed here, and black shows the same with NLTE. The grey band indicates the upper limit for metallicity dispersion in GCs (< 0.1 dex). Contours represent the 39%, 88%, and 95% volume intervals.

ping stars, we revisit the systemic metallicity and velocity dispersions of Sgr2, shown in Fig. 6.2 and as described in Section 5.1.

The velocity dispersion derived from the entire L21 spectroscopic sample and this study finds $\sigma_{v_r} = 1.73^{+0.48}_{-0.35}$ km s^{-1}. L21 estimated the velocity dispersion for a typical Milky Way Sgr2-like globular cluster is 1.1 ± 0.1 km s^{-1}, thus, our PDF suggests Sgr2's velocity dispersion is resolved and just barely higher than expected for a GC. This does not clearly rule out the GC origin for Sgr2 though, as some stars may be binaries (e.g., Sgr2584). Our examination of the metallicity dispersion shows $\sigma_{[Fe/H]} = 0.13^{+0.05}_{-0.04}$ dex (NLTE). Thus, our PDF suggests Sgr2's metallicity dispersion is resolved, but just barely above that expected for a GC.

On further analysis, the L20 and L21 datasets reveal two stars in common,

Table 6.1: Metallicity and velocity dispersions for Sgr2, including and excluding star83.

	sys [Fe/H] (dex)	$\sigma_{[Fe/H]}$ (dex)		sys v_r (km s^{-1})	σ_{v_r} (km s^{-1})
L21 + this work					
NLTE	$-2.25^{+0.04}_{-0.04}$	$0.13^{+0.05}_{-0.04}$	ph+sp:	$-176.52^{+0.39}_{-0.39}$	$1.55^{+0.38}_{-0.28}$
LTE	$-2.29^{+0.05}_{-0.05}$	$0.16^{+0.05}_{-0.04}$	*spec:*	$-176.89^{+0.63}_{-0.66}$	$1.72^{+0.48}_{-0.35}$
L21 (star83 excluded) + this work					
NLTE	$-2.23^{+0.03}_{-0.03}$	$0.06^{+0.03}_{-0.03}$	ph+sp:	$-176.41^{+0.49}_{-0.47}$	$1.45^{+0.36}_{-0.26}$
LTE	$-2.27^{+0.05}_{-0.05}$	$0.13^{+0.05}_{-0.03}$	*spec:*	$-177.15^{+0.60}_{-0.65}$	$1.59^{+0.43}_{-0.31}$

hereafter referred to as star34 and star83 (these numbers correspond to the target's order in Table 2 of L20; see Fig.6.1). The measurements for star34 are consistent within the reported uncertainties; however, star83 shows a large discrepancy in radial velocity and metallicity, where $\mathrm{RV}^{\mathrm{L20}}_{\mathrm{DEIMOS}} = -176.0 \pm 2.6$ km/s and $[\mathrm{Fe/H}]^{\mathrm{L20}}_{\mathrm{DEIMOS}} = -2.31 \pm 0.12$ (SNR = 17), compared to $\mathrm{RV}^{\mathrm{L21}}_{\mathrm{FLAMES}} = -172.2 \pm 1.5$ km/s and $[\mathrm{Fe/H}]^{\mathrm{L21}}_{\mathrm{FLAMES}} = -2.72 \pm 0.10$ (SNR = 11). To assess the influence of star83 on the systemic metallicity and velocity dispersions ($\sigma_{[Fe/H]}$, σ_{v_r}), we performed a jackknife test, presented in Table 6.1. The L21 FLAMES data for star83 has no significant influence on the velocity dispersion, however it alone can double the metallicity dispersion in Sgr2 and suggest a metallicity spread larger than seen in globular clusters, i.e., consistent with a UFD. The discrepancy between L20 and L21, combined with the outsized influence of this star, suggests that star83 (PS1 $g_0 = 20.21$) should be reobserved.

6.2 Chemistry in Sgr2

Due to the small sample size, asserting any abundance spreads among the elements in Fig. 4.2 in Sgr2 is challenging. The only chemical abundances that catch our attention are those for the neutron-capture elements, where Sr II and Ba II are usually somewhat lower for stars in dwarf galaxies than the Galactic comparison stars.

To emphasize this result, we show the Sr II, Ba II, and Eu II line syntheses for our Sgr2 stars in Fig. 6.3, relative to GHOST spectra of two standard stars, HD222925 and HD122563. While Eu II is clearly identified and synthesized in Sgr2584, we are more cautious in the analysis of the other Sgr2 stars, i.e., suggesting only upper limits for Eu II. Nevertheless, the Eu II upper limit for Sgr2936 is a valuable constraint as it is *lower* than the measurement for Sgr2584.

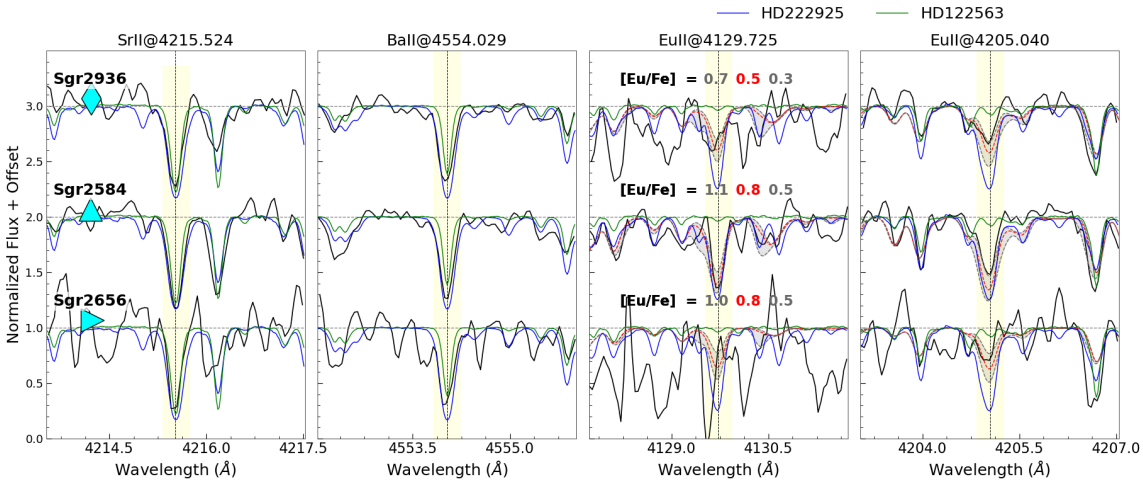

Figure 6.3: Comparison of n-capture element lines of SrII, BaII, and EuII between Sgr2 stars (black), the r-II standard star HD 222925 (blue), and the non-r-process-enhanced star HD 122563 (green). For the Eu lines, we also include synthetic spectra with varying [Eu/Fe] abundances, as indicated in the plots. The enhanced n-capture elemental abundances in Sgr2 stars are apparent, particularly the pronounced Eu II lines in Sgr 2584. For Sgr 2936 and Sgr 2656, only upper limits could be determined, both derived from the Eu line @4205 Å.

We also examine the absolute abundances of Sgr2584 and Sgr2936[1] compared to solar values and our two standard stars, HD222925 and HD122563. In Fig. 6.4, the chemistry for the two standard stars in determined in two ways: (1) from the literature for HD222925 Roederer et al. (2018) and HD122563 Honda et al. (2006); Collet et al. (2018), and (2) derived using the same spectral lines as for the Sgr2 stars (details discussed further in Venn et al. (2025)). The solar system's s- and r-process abundance patterns from Simmerer et al. (2004) are scaled to match the Ba and Eu abundances in Sgr2584. The chemical abundances for both Sgr2 targets are similar, and generally fall between those of the two standard stars.

6.2.1 Discovery of an r-I star in Sgr2

The abundance pattern of Sr, Ba, and Eu suggests that Sgr2584 is an r-I star ($0.3<$[Eu/Fe]<1 and [Eu/Ba]>0.4; c.f., Hansen et al. (2017)). In Fig. 6.4 we also present the solar system s- and r-process curves from Sneden et al. (2008), scaled to the Ba and Eu abundances of Sgr2584, respectively. Thus, a scaled solar system r-process pattern shows good agreement with the abundances in Sgr2584, based on our measurements of six n-capture elements.

6.3 R-process Enrichments in Stellar Populations

R-process enrichment in GCs: The globular clusters M15 and M92 show r-process enrichments. In M92, Kirby et al. (2023) observed a spread in Eu between Na-enhanced and low-Na stars, with the significant scatter in [Eu/Fe] confined to the low-Na first generation (1G) stars. They proposed a scenario where a source of the main r-process polluted M92 during the early stages of star formation. The 1G stars formed quickly, in less time than it took for gas to mix fully (within a crossing time), resulting in inhomogeneous r-process enrichment. The 2G formed later (~ 0.8 Gyr) after the gas had homogenized, resulting in little to no variation in r-process elements among the second generation (2G) stars. In M15, Cabrera Garcia et al. (2024) report similar findings to M92. Sgr2 exhibits abundance patterns that generally align with those of M92, as shown in Fig. 6.5.

[1]Sgr2656 is not plotted due to having fewer abundance measurements, all of which are consistent with the other two targets.

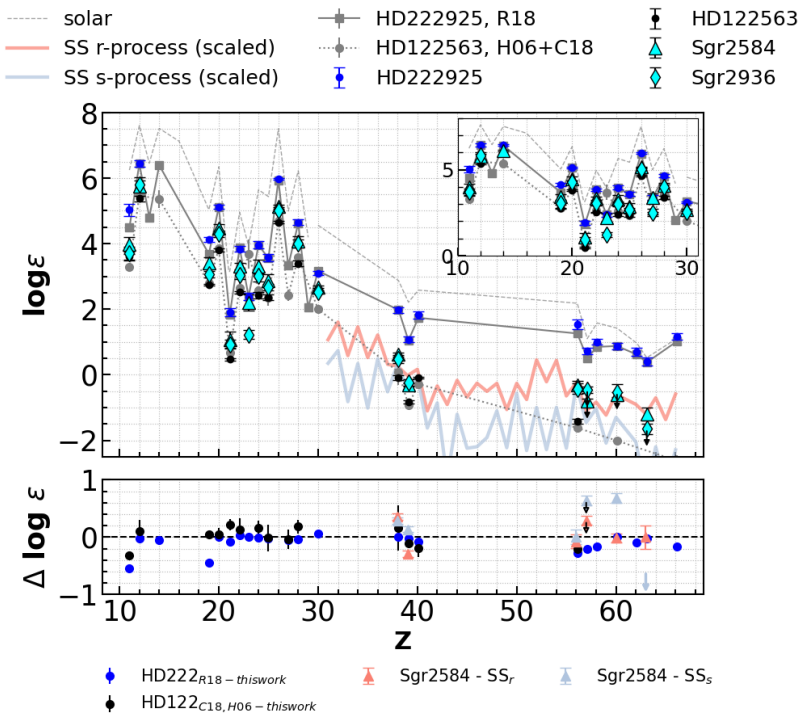

Figure 6.4: Comparison of abundances for two Sgr2 targets with HD222925, a standard r-process star, and HD122563, which has similar stellar parameters to the targets. The solar abundances are indicated by the grey dashed line. Abundances for the standard stars, derived using the same spectral lines as for the targets, are shown as black circles for HD122563 and blue circles for HD222925. Grey markers represent literature values for HD222925 from Roederer et al. (2018) and for HD122563 from Collet et al. (2018) and Honda et al. (2006). The solar system's s- and r-process abundance patterns from Simmerer et al. (2004), scaled to match the Ba and Eu abundances in Sgr2584, are shown in blue and red, respectively. The lower panel displays the residuals.

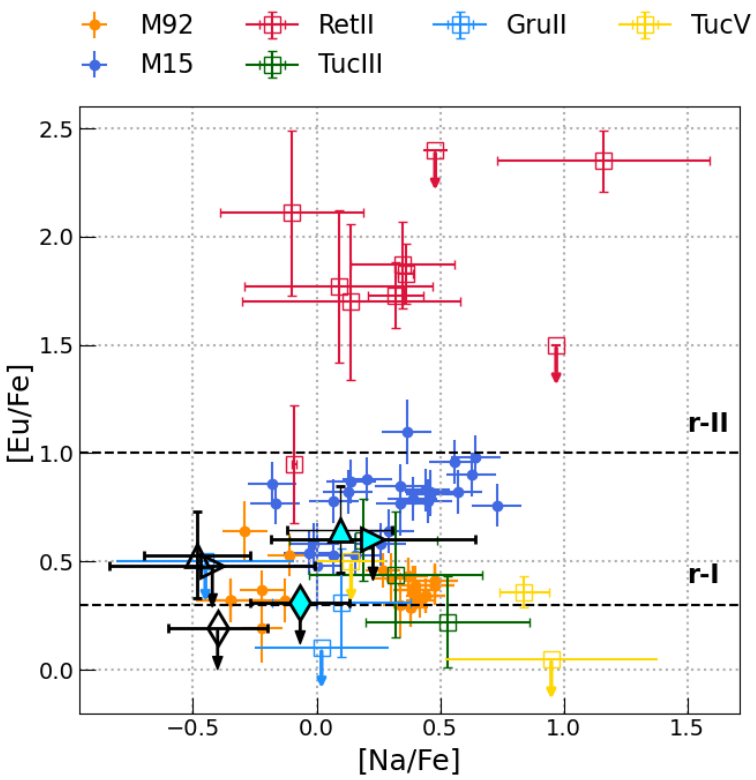

Figure 6.5: [Eu/Fe] as a function of [Na/Fe] for Sgr2 targets (cyan markers, downward arrows for upper limits), compared with two r-process-enriched globular clusters M15 (blue circles) and M92 (orange circles), both showing Eu abundance spreads; as well as four r-process-enriched UFDs Reticulum II (red open squares), Tucana III (green open squares), Gru II (light-blue open squares) and Tuc V (yellow open squares). NLTE abundances for our targets are shown as open markers. Na abundances for M15 stars are taken from Sneden et al. (1997), Sneden et al. (2000), Carretta et al. (2009), and Sobeck et al. (2011); Eu abundances are from Cabrera Garcia et al. (2024); data for M92 are sourced from Kirby et al. (2023); for Ret II, from Ji et al. (2016), Hayes et al. (2023), for Tuc III, from Hansen et al. (2017), Marshall et al. (2019) though only three of five stars with Na measurements are shown, for Gru II, from Hansen et al. (2020), and for Tuc V, from Hansen et al. (2024)

.

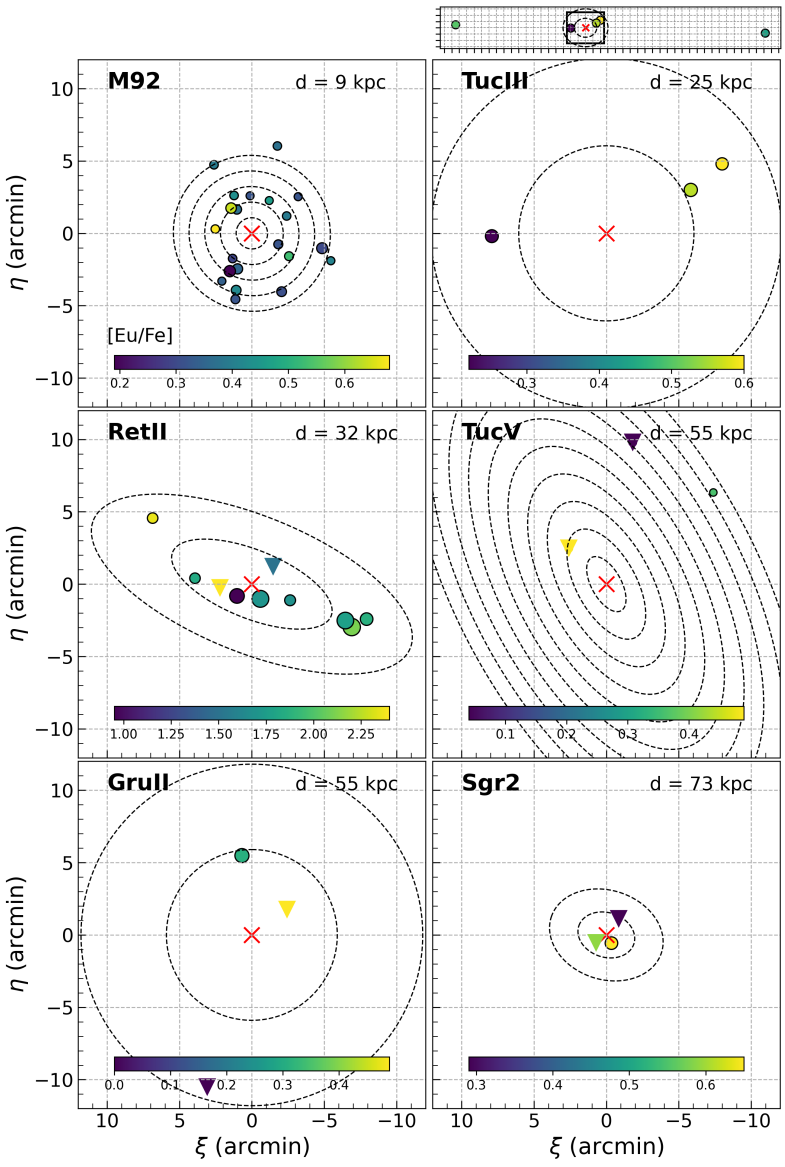

Figure 6.6: Positions of stars with [Eu/Fe] abundance measurement in M92, Tucana III, Reticulum II, Tuc V, Gru II and Sgr2 (shown in order of increasing distance). Marker sizes are proportional to the uncertainties, where smaller markers represent lower total errors and colours are correlated with Eu. Upper limits are indicated by downward triangles. Contours start at 1 R_h, with steps of 1 R_h. Due to the difficulty in constraining the system's ellipticities, for Tuc III and Gru II, circles of radii $n \times R_h$ are shown. Two very distant members of Tuc III are noted, near $\sim$ 12 and 15 R_h. Both axes are equally scaled to allow for size comparisons between systems.

R-process enrichments in UFDs: R-process enrichments in UFDs are exceptionally rare. Several UFD galaxies have been found to host r-process rich stars, including Tuc III, Gru II, and Tuc V which host r-I stars Hansen et al. (2017, 2020); Hansen et al. (2024); Marshall et al. (2019), and Ret II which shows that 70% of its observed members are highly Eu-enhanced r-II stars Ji et al. (2016); Hayes et al. (2023). Fig 6.5 shows that the Eu and Na abundances of the UFDs with only r-I stars do not stand out compared to the r-process-enriched globular clusters.

To test the r-process enrichment scenario further, we show the projected positions of stellar members in M92, Tuc III, Gru II, Tuc V, Ret II, and Sgr2, within their respective systems, in Fig. 6.6, along with their corresponding [Eu/Fe] abundances. Jeon et al. (2021) has suggested that the most critical factor in the formation of Eu-enhanced stars is how quickly new stars form around the event/NSM site, predicting that the highest Eu enhancements are achieved within ∼300 pc of the event/NSM site. Notably, the most Eu-rich star in Sgr2 *is* located near the system's center. However, this is not seen for any of the other systems. In the case of Tuc III, only core members are shown (excluding two stars from the tidal tails) as it is a disrupted galaxy. Its disruption may have altered the original positions of the three members shown, complicating efforts to trace the site of the initial Eu enrichment. In Gru II, its Eu-enriched star lies within the system's half-light radius, whereas in Tuc V, a similarly r-process rich member is located at the system's outermost edge (~ 9 R_h) and the closer members only have upper limits. In Ret II, the most Eu-rich member is found beyond one half-light radius from the system's center, while the star with the lowest [Eu/Fe] value is more central. Thus, overall, no clear trend with increasing distance is observed in these comparison systems. Jeon et al. (2021) also suggested that if Ret II were a satellite of the LMC, as indicated by its derived orbital history, this may have impacted the effects of reionization on its star formation history, and thereby the likelihood of forming metal-poor r-II stars throughout. Full cosmological simulations with detailed chemical evolution will be necessary to explore connections between r-process enhancements and locations in dwarf galaxies Manwadkar & Kravtsov (2022, 2024).

As a reference globular cluster for comparison, M92 exhibits the highest [Eu/Fe] abundances in members located roughly two half-light radii to the northeast; see Fig. 6.6. However, no clear gradient is observed with respect to radial distance or along the east-west and north-south directions.

In general, our analysis of these systems shows that r-process enrichments alone,

at least via the presence of r-I stars, is insufficient to constrain a system's origin, i.e., as an UFD or globular cluster, whether examining the scatter in the [Eu/Fe] abundances within a system or the spatial distribution of r-process rich stars within the system.

In summary, we find that Sgr2 is a very intriguing case. It is comparable to Tuc III, as an ambiguous system that remains difficult to classify, even with detailed chemical analyses of its brightest members.

6.4 Comparison of Sgr2 with Tuc III

Tuc III is a particularly interesting system as it has been classified as a UFD based on its low average metallicity ([Fe/H] ~ -2.49; Li et al. (2018b)), a velocity and metallicity dispersion, and the absence of light-element anti-correlations amongst five of its brightest members Hansen et al. (2017); Marshall et al. (2019). However, Marshall et al. (2019) note that adopting the photometric temperature for the metallicity outlier star from Hansen et al. (2017) would eliminate the statistically significant metallicity spread among its members. The observed metallicity gradient from CaT lines among core and tidal tail members (shown in Fig. 6.7) has likewise been presented as evidence for the system's origin as a UFD (Li et al., 2018b). We reanalyze the evidence for a metallicity dispersion and metallicity gradients in Fig. 6.8 and do not find clear evidence for Tuc III to be classified as an UFD.

And, unfortunately, the velocity distribution for Tuc III is not representative of the system due to its disrupted state (only an upper limit of 1.5 $\mathrm{km\,s^{-1}}$ at the 95.5 % confidence level for core members was derived by Simon et al. 2017). Taking into account that low metallicity is also insufficient evidence for the presence of dark matter (i.e., an UFD classification), as globular clusters are typically found with [Fe/H] $= -2.5$, and even lower ([Fe/H] $= -2.9$ have been found for M31 clusters Simpson (2018); Larsen et al. (2020), and the stellar stream C-19 appears to be a disrupted star cluster with [Fe/H] $= -3.4$, see Martin et al. (2022); Yuan et al. (2022); Venn et al. (2025)), then Tuc III remains a challenging system to classify.

Both Sgr2 and Tuc III have at least one star that exhibits a europium enrichment, but at levels comparable to stars in the GCs, M15 and M92, and well below the r-II stars found in the UFD, Ret II. Other n-capture elements (Sr and Ba) are at levels consistent with the MW halo, similar to those in GCs, and therefore somewhat higher than typically found in stars in UFDs. This is noteworthy as Ji et al. (2019) has

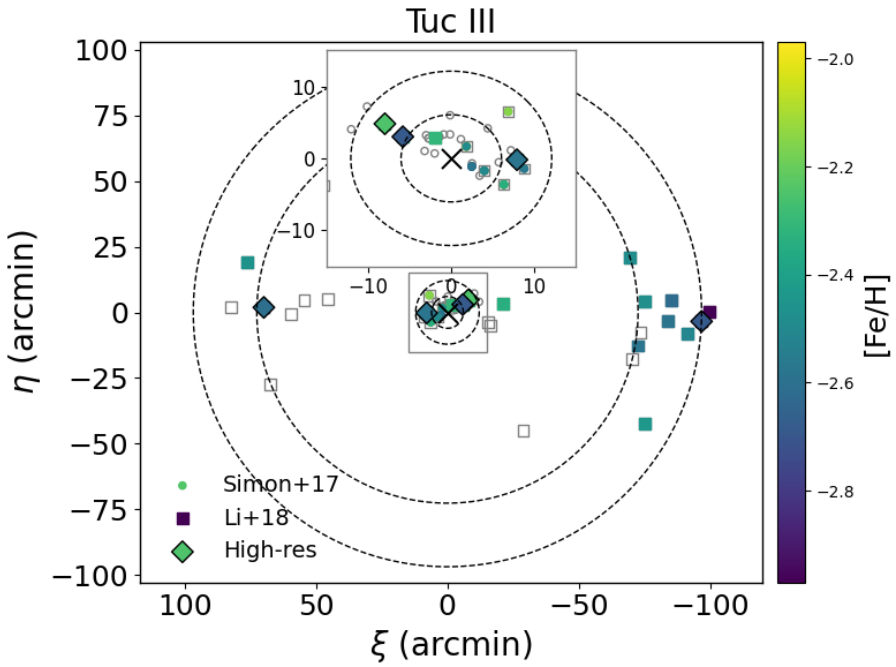

Figure 6.7: Spatial distribution of Tuc III members observed by Simon et al. (2017) (circles, concentrated in the core), Li et al. (2018) (squares), and high-resolution studies by Hansen et al. (2017); Marshall et al. (2019) (diamonds) is shown. Members with available metallicities (determined from either CaT or iron lines) are color-coded by metallicity, while open gray markers represent observations without measured metallicities. Dashed circles indicate radii of 1, 2, 12, and 16 R_h.

suggested that low neutron-capture element abundances are a distinguishing feature of the faintest dwarfs. Earlier, in our Fig. 5.4, we showed that the mean neutron-capture element abundances for Sgr2 and Tuc III are higher than those of other UFDs. Taken together, we find that the evidence is not yet clear on the classification of either Sgr2 nor Tuc III.

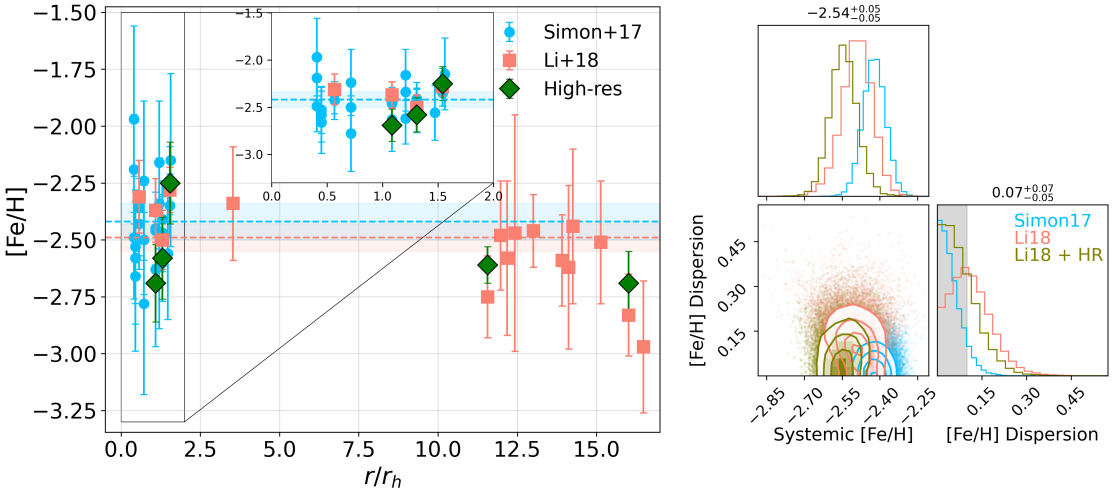

Figure 6.8: *Left:* Radial distribution of metallicities for TucIII members. Marker shapes are consistent with those in Fig. 6.7. Notably, the measurements by Li et al. (2018) suggest a slight metallicity gradient between the core and tidal tail members. However, this trend is primarily driven by the three most metal-poor members, two of which were followed up with high-resolution spectroscopy by Marshall et al. (2019), weakening the strength of the reported gradient. *Right:* Probability density function (PDF) of systemic metallicity and metallicity dispersion for Tuc III, based on samples from Simon et al. (2017) (core members, light blue), Li et al. (2018) (primarily tidal tail members, salmon), and a combined sample from Li et al. (2018) and high-resolution studies by Hansen et al. (2017) and Marshall et al. (2019), with high-resolution metallicities used for stars present in both datasets (olive). The analysis shows that when high-resolution metallicities are applied to the most metal-poor members in the tails, the dispersion decreases to a level comparable to that of star clusters (gray band), aligning more closely with the dispersion observed in the core. Note also he most metal-rich member from high-resolution studies shows a decrease in metallicity by ~ 0.2 dex when T_{phot} is applied (see discussion in Marshall et al. (2019))

Chapter 7

Additional diagnostics for ambiguous systems

The present work demonstrates two possible scenarios that may arise during the review or reassessment of UFDs and UFD candidates with high-resolution spectroscopy. On the one hand, there is Aqu2, where a clear metallicity spread and distinct chemical signatures, even among just the two brightest member stars, strongly support its classification as a UFD. Combined with its extended size and the radial velocity dispersion estimated in previous studies, this provides robust evidence for the presence of a dark matter halo in this system. On the other hand, high-resolution spectroscopic follow-up of Sgr2 has not resolved its classification, instead highlighting its "on the border" position in terms of kinematics and metallicity, as well as its detailed chemical abundances.

The most common approach to identify a low surface brightness system within a dark matter halo is to examine the velocity dispersion profile and compare it to estimates for a purely baryonic scenario. However, as noted in Fig. 6.2, the method used to calculate the expected velocity dispersion for the self-gravitating case significantly affects the results. The expected velocity dispersion for Sgr2 using the Wolf et al. (2010) formalism is shown in Fig. 6.2 as the grey-shaded band at ~ 1 km s^{-1}, which is too large to clearly resolve the velocity dispersion. In contrast, adopting the star-cluster-specific approach of Baumgardt (2017), which accounts for energy equipartition and mass segregation effects commonly observed in globular clusters (e.g., Baumgardt & Makino 2003), reduces the expected velocity dispersion to ~ 0.5 km s^{-1}(gray dashed line in Fig. 6.2).This lower value means that we do resolve our

velocity dispersion, and hints at a classification for Sgr2 as an UFD.

In addition to theoretical uncertainties, the observed velocity values can also be influenced by data quality and sample selection (e.g., compare the pink profile from L20 and the green profile from L21 in Fig. 6.2), as well as binary contamination. GC observations show that the binary fraction increases toward a cluster center (e.g., Sollima et al., 2007; Ji et al., 2015), and simulations reveal that as binaries segregate, "hard"[1] binaries become even harder. Their semimajor axes shrink according to the Heggie 1975 - Hills 1975 law, making them more difficult to identify and potentially causing up to a 70% overestimation of the velocity dispersion in the cluster's core (Aros et al., 2021a). As a quantitative example, Wang et al. (2024) estimated the observed binary fraction for a Palomar 5-like globular cluster (which we note is close to Sgr2 on the M_V vs. r_h diagram; see Fig. 1.1), with a heliocentric distance of $\sim$ 20 kpc. They showed that most bright binaries with periods below 10^4 days can be detected within $\sim$6 months by measuring line-of-sight velocities of $|\Delta v_r| > 0.3$ km s^{-1}. The undetected binaries ($|\Delta v_r| < 0.3$ km s^{-1}) could still inflate the computed velocity dispersion by a factor of 1.5-2 compared to estimates based solely on single stars. For Sgr2, which is $>$ 3 times farther away, the stars have measured radial velocity uncertainties $\sim$1 km s^{-1} (L21), constrained by observations of only $\sim$1 month (38 days). This implies its $\sigma(v_r)$ is not resolved. This agrees with Baumgardt et al. (2022), who estimated a lower velocity dispersion for Sgr2[2] of $\sim$ 0.6 km s^{-1}, i.e., 3x lower than L21 (see Fig. 6.1), and attributed the higher observed $\sigma(v_r)$ entirely to binary contamination.

To take these studies further, Baumgardt et al. (2022) have conducted a homogeneous and extensive study of mass segregation in GCs and UFD candidates using N-body simulations. As a measure of mass segregation, they used the ratio of the radii where the cumulative fraction of bright and faint stars reaches 0.5. A lower $\frac{R_{h,\mathrm{bright}}}{R_{h,\mathrm{faint}}}$ ratio (deviating further from unity) indicates stronger segregation and is expected in clusters with relaxation times much shorter than their age. To get the two subsets, members below the main sequence turn-off and above a certain M_{Low} mass threshold were divided into two equally sized groups based on brightness. For Sgr2, their mass segregation parameter $r = \frac{R_{h,\mathrm{bright}}}{R_{h,\mathrm{faint}}} = 0.96 \pm 0.02$, which is in agreement with

[1] "hard" means that their binding energy is much higher than the average kinetic energy of stars in a cluster

[2] The velocity dispersion profile for Sgr2 derived with N-body models of Baumgardt (2017) can be found at https://people.smp.uq.edu.au/HolgerBaumgardt/globular/fits/kin/sgrii_vel.pdf

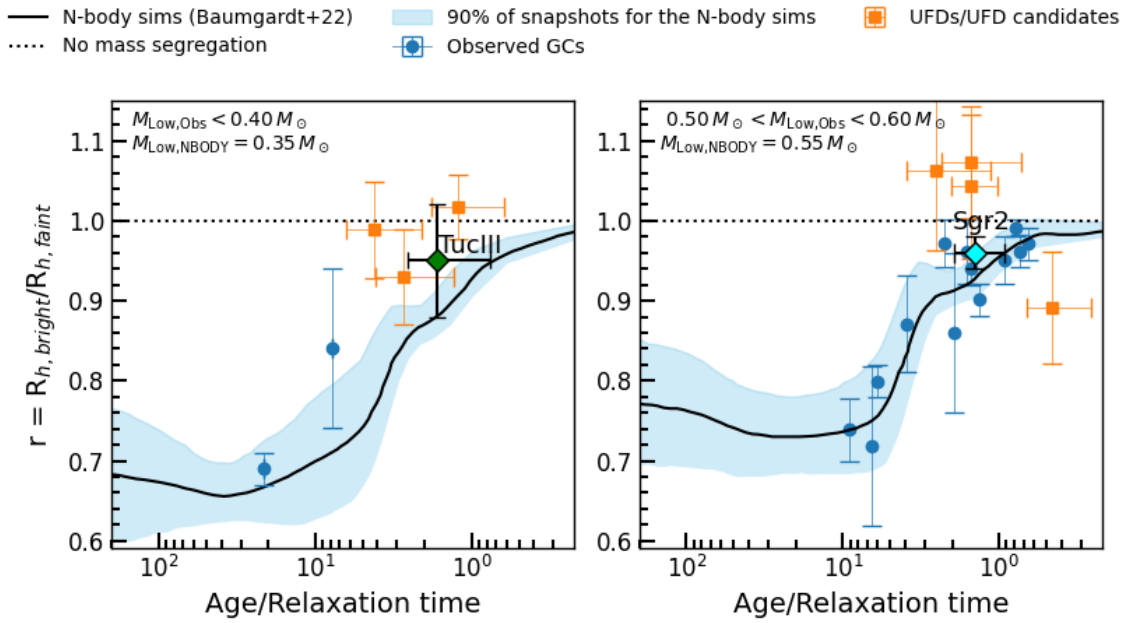

Figure 7.1: Mass segregation ratios, defined as the ratio of the radius containing half the bright stars ($R_{h,bright}$) to the radius containing half the faint stars ($R_{h,faint}$), plotted as a function of the dynamical age ($T_{\rm Age}/T_{\rm RH}$) for MW globular clusters. Results are based on the analysis by Baumgardt et al. (2022). Samples are categorized by the lowest stellar mass analyzed in each cluster, with corresponding N-body model results adjusted for varying minimum masses, as indicated in the panels. The black solid line and pale blue shaded region represent results from N-body simulations. Observed GCs are shown in blue, while UFDs analyzed in the study, either confirming or establishing their classification, are shown in orange. Tuc III and Sgr2 are highlighted as black-edged diamonds.

the expected value for a star cluster of Sgr2's relaxation time of 8.37 Gyr, calculated following Spitzer (1987)[3].

We present the mass segregation parameters versus the ratio of age to relaxation time (dynamical age, $T_{\rm Age}/T_{\rm RH}$) for globular clusters in Fig. 7.1, alongside the N-body predictions from Baumgardt et al. (2022). Two panels are shown to differentiate between the lowest mass analyzed in each cluster, and to include corresponding N-body model results for other systems adjusted for the minimum mass.

The computed mass segregation parameter for Sgr2 from Baumgardt et al. (2022) aligns well with the trend observed in GCs. While the value is close to 1 (indicating no mass segregation), the small bootstrapped uncertainties place it firmly within the region typically occupied by star clusters at this $T_{\rm Age}/T_{\rm RH}$. As an additional test for mass segregation, the authors performed a KS test on the cumulative distributions of bright and faint stars, finding a high significance for segregation in Sgr2 ($P_{\rm Mseg} = 97.5\%$). This contrasts with the results for Tuc III, where both the mass segregation ratio (0.95 ± 0.07) and the KS test result (42.8%) remain inconclusive.

We support that the mass segregation parameter can provide an additional and valuable test for low surface brightness systems when trying to determine their origins (GC vs UFD), total mass, and thereby dark matter contents. The chemical patterns – particularly in heavy elements – and mass segregation of Sgr2 align with those of similar Milky Way GCs, supporting its classification as a star cluster. Such diagnostics are especially important when alternative approaches, like studying system stability within the Milky Way's tidal field, are inapplicable or computationally expensive (e.g., Sgr2's distant pericenter, as noted in Section 1.5, or the impact of the LMC on Tuc III).

[3]We note that Wang et al. (2024) find that the presence of black holes can significantly shorten the two-component relaxation time.

Chapter 8

What's Next: Navigating the 'Valley of Ambiguity'

8.1 The faintest systems

The systems explored in this thesis occupy the so-called "Valley of Ambiguity" in the M_V–r_h plane, defined by extremely low luminosities ($M_V \gtrsim -5$), small sizes, and uncertain nature given their structural and dynamical properties.

The ambiguity between star clusters and dwarf galaxies varies across this space. Extended systems are typically classified as UFDs but may be dissolving clusters, while compact systems are often labeled as clusters but could instead be remnants of early-accreted dwarfs ("microgalaxies"), or systems initially formed in ultra-low-mass halos.

As the number of known faint satellites increases and N-body simulations continue to explore both dark-matter-free and dark-matter-dominated scenarios, it is becoming increasingly clear that multiple evolutionary and dynamical pathways can lead to similar observational properties. Consequently, representatives of both classes within this regime could, in principle, occupy almost any region of the M_V–r_h space.

This complexity underscores the need to improve and refine the criteria we use to distinguish between star clusters and dwarf galaxies. It also highlights the importance of recognizing observational biases, considering alternative formation scenarios, and employing complementary diagnostics.

In this chapter, I take a closer look at the "Valley of Ambiguity" in this context, aiming to explore the full spectrum and gradient of ambiguity across this regime and

discuss how different lines of evidence can help us navigate its diverse landscape.

8.2 Regions of Common Properties

In Fig. 8.1, I present a closer look at the "Valley of Ambiguity", which I have divided into five distinct regions for clarity. The systems grouped by region are listed in Table 8.1. These regions will be discussed in detail below, but here I provide a brief overview as follows:

In **Region A**, I show how extended sizes and ellipticities measured through photometry are sufficient to infer the dark matter-dominated nature of these systems — making them a natural extension of classical dwarf galaxies. I also briefly discuss their resilience to tidal disruption and how other classification methods serve primarily as supplemental evidence supporting their origin.

In **Region B**, I demonstrate how small number statistics, instrumental effects, and unknown binary fractions can bias estimates of dark matter content in systems currently classified as UFDs. Motivated by our findings for Tuc III, discussed in this thesis, I also show how metallicity outliers can inflate measurements of metallicity dispersion, underscoring the need to revisit certain systems with better constraints on their dark matter content. This need is further supported by N-body modeling, which shows that extended clusters can exhibit dynamical and structural properties similar to those of dwarf galaxies.

In **Region C**, where many systems remain ambiguously classified and analysis is further complicated by faint magnitudes, I show the increasing importance of alternative classification methods, e.g., mass segregation, chemical abundances, and density analyses. In some cases, these methods may even yield conflicting results. I also present an independent analysis of the resilience of these systems to tidal forces in the MW field and propose a classification scheme for some systems based on a compilation of the available data.

In **Region D**, I consider the possibility that these systems are globular clusters of non-Galactic origin undergoing mass loss, leading to their low observed luminosities. Alternatively, some may be (ex-situ formed) open clusters with intrinsically lower densities. This region may also extend into neighboring Regions C and E, suggesting similar dynamical evolution – an idea that I illustrate by studying non-Galactic associations of the ambiguous systems, as well as their clustering in the luminosity-metallicity plane.

Table 8.1: Faint MW satellites grouped by Region in the M_V vs r_h plane, see Fig 8.1.

Name	Short	Reg	Name	Short	Reg	Name	Short	Reg
Aquarius II	Aqu2	**A**	Bootes V 2	Boo5	**B**	Balbinot 1	–	**C**
Boötes IV	Boo4	**A**	Carina III	Car3	**B**	Cetus II	Cet2	**C**
Canes Venatici 2	CanVen2	**A**	Horologium I	Hor1	**B**	DELVE 1	–	**C**
Carina II	Car2	**A**	Horologium II	Hor2	**B**	DELVE 2	–	**C**
Cetus III	Cet3	**A**	Hydra II	Hyd2	**B**	DELVE 3	–	**C**
Coma Berenices	ComBer	**A**	Hydrus I	Hyd1	**B**	DELVE 4	–	**C**
Eridanus IV	Eri4	**A**	Indus 1	Ind1	**B**	DES 1	–	**C**
Grus I	Gru1	**A**	Leo I	Leo1	**B**	DES 4	–	**C**
Indus II	Ind2	**A**	Palomar 14	Pal14	**B**	DES J0225+0304	–	**C**
Leo IV	Leo4	**A**	Pegasus III	Peg3	**B**	Draco II	Dra2	**C**
Pegasus III	Peg3	**A**	Pegasus IV	Peg4	**B**	Eridanus III	Eri3	**C**
Tucana II	Tuc2	**A**	Phoenix II	Pho2	**B**	Gaia 3	–	**C**
Tucana IV	Tuc4	**A**	Pisces II	Pis2	**B**	HSC 1	–	**C**
Tucana V	Tuc5	**A**	Reticulum II	Ret2	**B**	Kim 2	Kim2	**C**
Ursa Major I	UMa1	**A**	Sagittarius II	Sag2	**B**	Leavens 3	–	**C**
UrsaMajor II	UMa2	**A**	Segue 1	Seg1	**B**	Munoz 1	–	**C**
			Segue 2	Seg2	**B**	Pictor I	Pic1	**C**
			Triangulum II	Tri2	**B**	PS 1	PS1	**C**
			Tucana III	Tuc3	**B**	SMASH 1	–	**C**
			Virgo I	Vir1	**B**	Virgo II	Vir2	**C**
						YMCA-1	–	**C**
AM 4	AM4	**D**	BLISS 1	–	**E**			
Koposov 1	Ko1	**D**	DES 5	–	**E**			
Koposov 2	Ko2	**D**	DES J0111-134	–	**E**			
Palomar 1	Pal1	**D**	Kim 1	Kim1	**E**			
Torrealba 1	To1	**D**	Kim 3	Kim3	**E**			
Whiting 1	–	**D**	Segue 3	Seg3	**E**			
			DELVE 5	–	**E**			
			UrsaMinor III/UNIONS 1	UMiIII/U1	**E**			

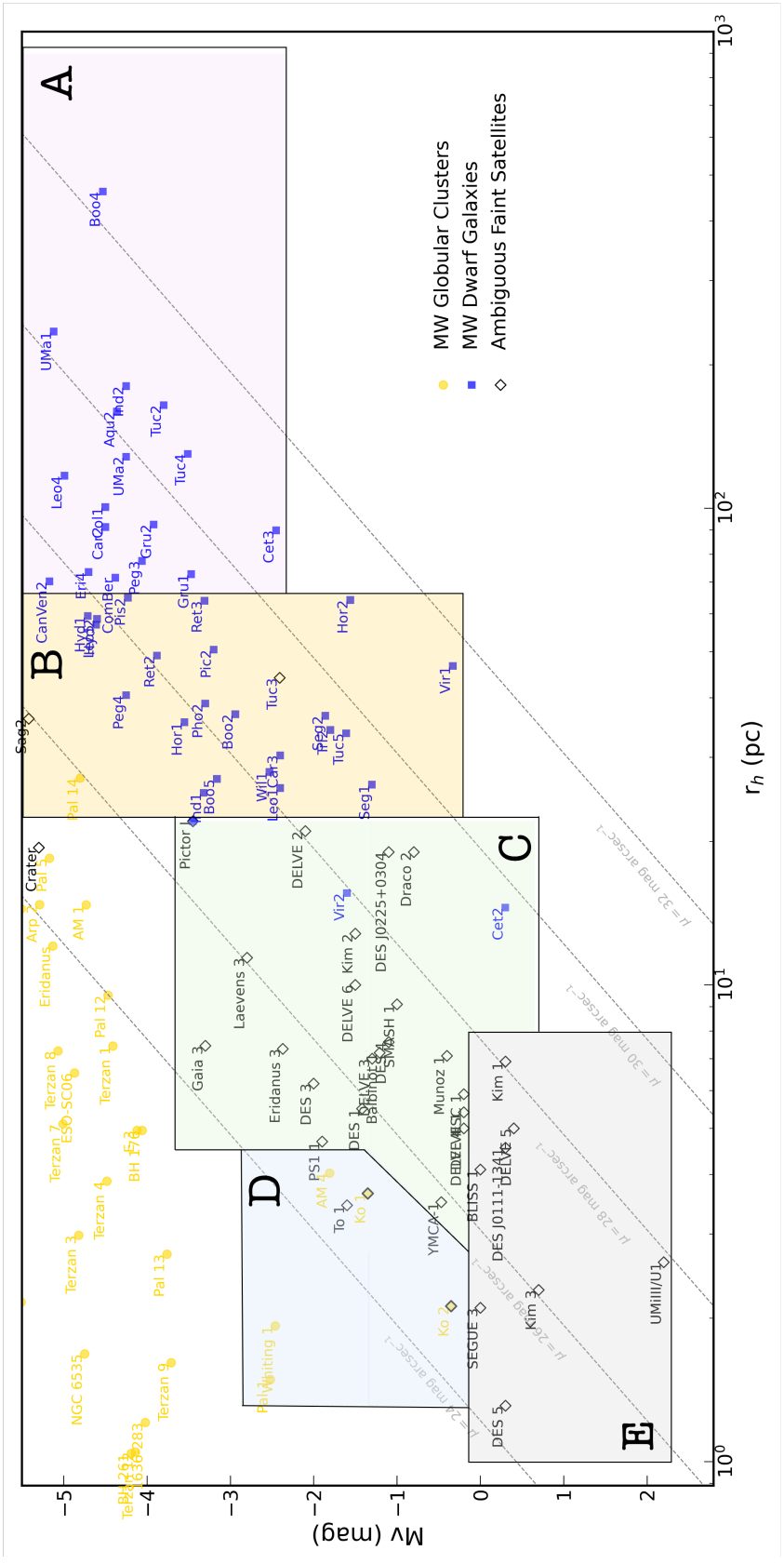

Figure 8.1: Same as Fig. 1.1, but zoomed in on the *Valley of ambiguity* region. Grey dashed lines represent constant surface brightness levels. Distinct regions with common properties (A–E) are highlighted in different colors, see text for details.

Finally, in **Region E**, I examine the impact of short relaxation/evaporation timescales, coupled with tidal effects, on the smallest and faintest known systems. I explore how the slope of the mass function (MF), which depends on dynamical evolution but is largely independent of environment, may serve as a distinguishing feature between star clusters and dwarf galaxies. I also emphasize the importance of comprehensive N-body modeling for understanding the survivability of these systems on their orbits, highlighting the extreme case of Ursa Major III/UNIONS 1.

8.3 Region A

This region appears to be a natural extension of the classical dwarf spheroidal (dSph) population. Systems within it are typically classified as UFDs due to their extended sizes and relatively high ellipticities. These galaxies have been discussed in detail by Simon (2019a), with additional members identified more recently, particularly through deep surveys near the Magellanic Clouds (REF).

Figure 8.2 shows ellipticity (e) as a function of luminosity (M_V), highlighting systems in this region. As evident, most exhibit well-constrained ellipticities with $e \gtrsim 0.4$. Their dark matter-dominated nature is further supported by measured velocity dispersions in 8 out of 17 systems (Car2, Tuc4, CanVen2, ComBer, Aqu2, UMa1, Tuc2, Eri4), also indicated in the figure. Despite their low luminosities and masses, these systems exhibit high velocity dispersions, resulting in some of the highest M/L ratio measurements known. This supports the notion that M/L ratios increase toward fainter systems – although this trend may not persist into the next regions.

While many of these systems are structurally elongated, most show no signs of ongoing tidal disruption, based on the dynamical density analysis by Pace et al. (2020). Their apparent stability is likely due to their high M/L ratios. Potential exceptions include Gru2 and Tuc4, which lie close to the average Milky Way density at their pericenters.

High-resolution chemical abundance studies have been conducted for 7 systems in this region – Leo4, Tuc2, Car2, Gru2, UMa1, UMa2 (see references in Fig. 4.2), and Aqu2 (this thesis) – and reveal abundance patterns distinctive from those of the Milky Way halo and consistent with signatures typically associated with UFDs (as discussed in Sec. 1.4.3).

By combining evidence for dark matter from structural, kinematical, dynamical, and chemical studies, these systems serve as an excellent comparison baseline for

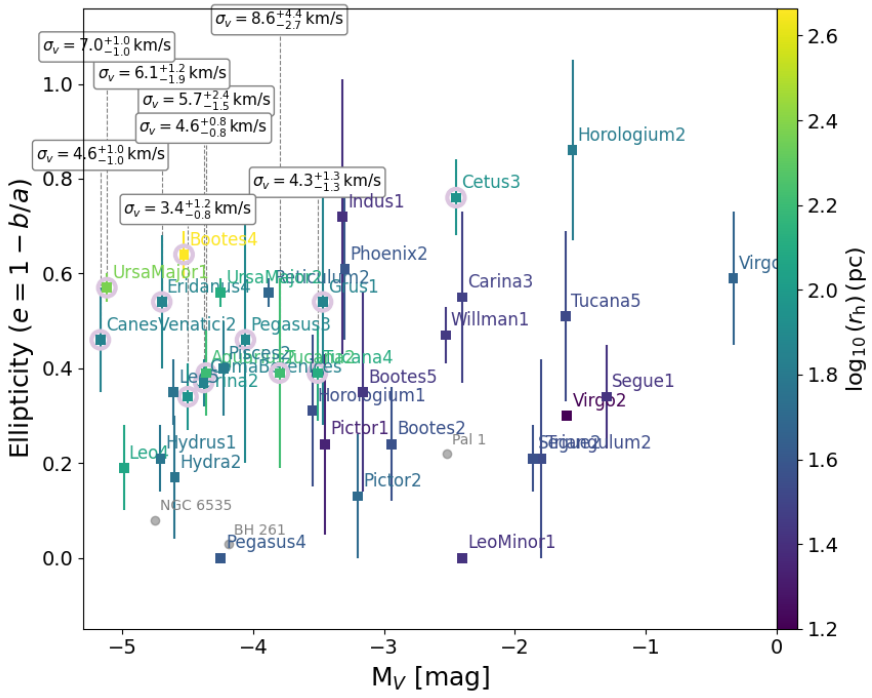

Figure 8.2: Ellipticity, e, as a function of V-band absolute magnitude, M_V, for known UFDs in Regions A and B. Data points are color-coded by $\log_{10}$ of half-light radius. Systems from Region A are circled in light purple, with velocity dispersions shown where available. Ellipticities are taken from McConnachie & Venn (2020); velocity dispersions are from Simon & Geha (2007); Walker et al. (2016); Li et al. (2018a); Simon et al. (2020); Heiger et al. (2024).

dark-matter-dominated faint satellites

8.4 Region B

This region marks the onset of ambiguity, where the two classes begin to blend. This is more evident in the density–size plane (see left panel of Fig. 8.4). As the Fig. 8.1 shows, all the systems in this region are classified as UFDs. However, as demonstrated in this work for the case of Tuc III, the classification in this regime can sometimes be less reliable. Examples of other systems that stand out as outliers from the broader population of UFDs in this Region include: HorI – the first UFD known to host multiple stellar populations (Jerjen et al., 2018a), a feature more commonly associated with globular clusters; Hyd1 – a notable outlier from the galaxy mass-metallicity relation (Hargis et al., 2016, see discussion in Sec 8.7.1); and Sgr2 – one of the two targets in this thesis, which may be the most extended globular cluster known, lacking signs of tidal disruption and lying closest to the UFD locus in the size–luminosity plane.

Region B also may suffer from confident dark matter content estimations due to several measurement limitations. For example, as discussed in Sec. 1.4.1, the estimation of dark matter abundance in a system comes primarily from the velocity dispersion, yet, this is complicated by the small number statistics, large measurement uncertainties, instrumental limitations and binary inflation that can dominate the dark matter content estimate. As mentioned in Sec. 1.3, measuring the dark matter density is important for identifying potential sites of dark matter particle annihilation signals. Therefore, it is crucial not only to detect the *presence* of a dark matter halo in a system, but also to place tighter constraints on its abundance.

8.4.1 Dispersion Analyses Caveats

To illustrate the interplay between the number statistics of confirmed members and the uncertainties in individual measurements in this region, I present the metallicity–radial velocity distribution of member stars for several systems in the right panel of Fig. 8.4. As shown in Fig. 5 of Errani et al. (2024b), UFDs and GCs exhibit some degree of overlap in density within this r_h range; therefore, I also include nearby GCs for comparison. All confirmed binary stars have been excluded from this plot, as they will be discussed separately in a later section.

Before turning to more complex cases, it is worth highlighting several systems within this region provide compelling evidence for the presence of dark matter halos. Notable examples include Reticulum II (Ret2) and Hydrus I (Hyi1), both of which display well-resolved dispersions in velocity and metallicity, with uncertainties small enough to confidently resolve these spreads. Another strong candidate for a dark-matter-dominated system is Segue 1 (Seg1), which exhibits a clear metallicity dispersion despite a relatively small number of spectroscopic members[1]. See, however, the discussion on alternative scenario for this system in Sec. 8.4.2.

In contrast, Triangulum II (Tri2) and Segue 2 (Seg2) illustrate the challenges of interpreting dark matter halo signatures in systems with few confirmed members. In both cases, a single metallicity outlier at [Fe/H] ~ -1.5 dex substantially affects the inferred metallicity spread, while their velocity dispersions remain unresolved. These two systems share similar structural parameters and occupy nearly the same location in density–radius space, lying closest to the globular cluster locus (see Fig. 8.4). Seg2 is also an outlier from the mass–metallicity relation of galaxies, with $\langle [Fe/H] \rangle = -2.2$ – significantly higher than other UFDs of similar luminosity.

Tri2 is particularly notable for the presence of a confirmed binary star (star 46; Venn et al., 2017b), which has a well-constrained orbital solution (Buttry et al., 2022). Excluding this star from the analysis renders the system's velocity dispersion unresolved. The evidence for a metallicity spread hinges on the membership status of ~ 2 relatively metal-rich stars.[2] Consequently, the classification of Tri2 remains uncertain. Its detailed abundance patterns may provide additional insight (Ji et al., 2019), as discussed in the following subsection. Finally, given that both systems have been the subject of extensive study and that I happened to have observations of individual stars in each using *Gemini*/GRACES (see Fig. 8.3), I adopt Tri2 and Seg2 as case studies to illustrate key caveats in identifying dark matter halos through dispersion-based analyses. Each is examined in detail in the sections that follow.

Segue 2 (Seg2)

In Fig. 8.5, I show three samples of Seg2 members identified by Belokurov et al. (2009) with the Hectochelle spectrograph (only velocities measured; metallicities are taken

[1]Notably, the member star with the largest velocity uncertainty ($\sim$10 km s^{-1}) originates from a separate analysis (Norris et al., 2010) compared to the rest of the sample (Simon et al., 2011)

[2]The second metallicity outlier is the binary star 46 (excluded from Fig. 8.4); however, its derived metallicity depends sensitively on the adopted stellar parameters – see the differences among Venn et al. (2017a), Kirby et al. (2017), and Ji et al. (2019).

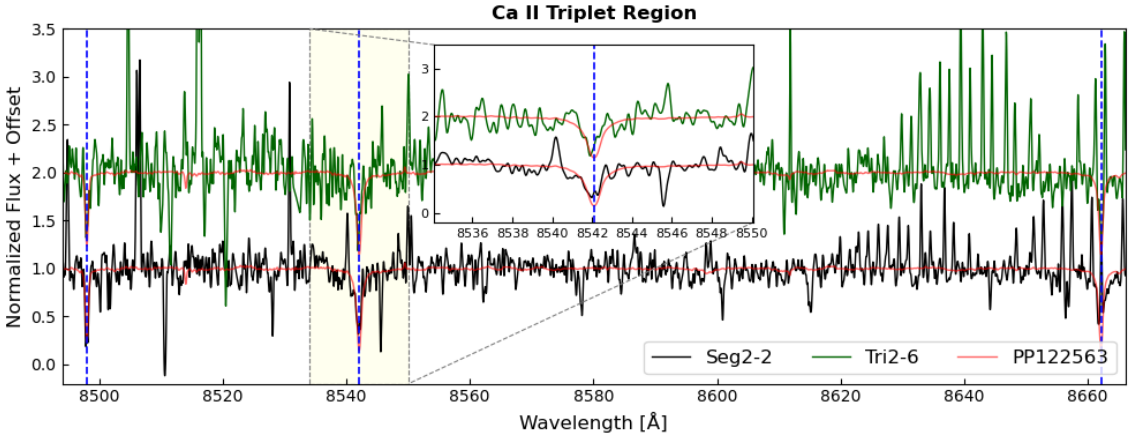

Figure 8.3: Gemini/GRACES spectra of the Seg2-2 and Tri2-6 member stars, with the reference star PP122563 (PARAMETERS) overplotted, focused on the Ca II triplet region. The inset shows a zoom-in on the Ca II line at 8542Å, whose equivalent width (EW_{8542}) was used in both cases to derive [Fe/H] via the Starkenburg et al. (2010) calibration, assuming a fixed line ratio of EW_{8542}/EW_{8662}=1.2.

from Kirby et al. (2013a) for stars in common), by Kirby et al. (2013a) with DEIMOS, and by us, based on CMD position, proper motion, metallicity, and radial velocity from the Hectochelle spectroscopic sample of Walker et al. (2023) (showing mean metallicity and velocity values averaged across epochs). The only star cross-matched across all samples in this plot is Seg2-2, the star measured in this study. As shown, the highest-metallicity outlier appears in the sample of Kirby et al. (2013a), while the sample from Belokurov et al. (2009) exhibits a larger radial velocity spread, albeit based on significantly smaller number statistics (5 RGB stars). The potential members selected from Walker et al. (2023) show a narrower dispersion in both velocity and metallicity; however, the metallicity may be systematically lower, as indicated by the comparison of the cross-matched star. Such a comparison is valuable for understanding the possible effects of instrumentation and member selection methodology, as was already discussed in the comparison of the L20 and L21 samples for Sgr2 in Sec. 7. In Fig.8.6, we further cross-match four stars common between the samples. Our measurements for Seg2-2 with GRACES ($v_r = -40.43 \pm 0.80$ km s^{-1}, [Fe/H] $= -2.54 \pm 0.07$) are in excellent agreement with those of Belokurov et al. (2009) and Kirby et al. (2013a), with a tighter constraint on velocity. The individual-epoch measurements from Walker et al. (2023) also show no signs of binarity, although they provide much larger uncertainties on the metallicity measurements. Overall, the uncertainties and possible zero-point differences between the instruments do not reveal clear signs of binarity for any of the compared stars, except for Seg2-033 (shown in yellow), which exhibits a velocity difference of $v_r(\mathrm{K13}) - v_r(\mathrm{B09}) = -7.7 \pm 2.3 \mathrm{km\,s^{-1}}$, suggesting it could be a possible binary. Interestingly, this star is also responsible for the larger velocity spread observed in Belokurov et al. (2009)'s sample compared to that of Kirby et al. (2013a).

Triangulum II (Tri2)

In Fig.8.7, I present individual-epoch measurements of confirmed Tri2 member stars in the metallicity–radial velocity plane, as reported across various studies. One confirmed binary clearly stands out, while the binarity status of the remaining members remains unresolved within current uncertainties and temporal coverage.

Our measurement for star6 ($v_r = -384.73 \pm 0.77$ km s^{-1}, [Fe/H] $= -2.83 \pm 0.18$) is consistent with the multi-epoch velocity analysis of Buttry et al. (2022), but yields a higher metallicity than reported in their study. Notably, Buttry et al. (2022) also

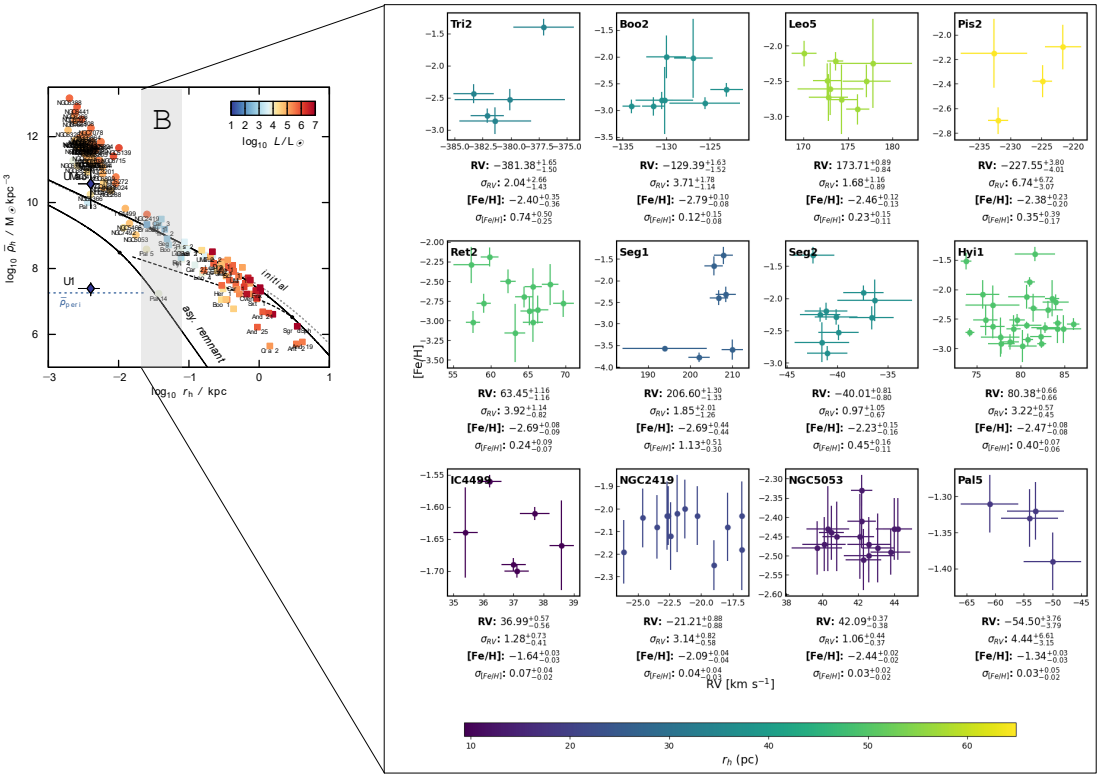

Figure 8.4: *Left panel:* Figure 5 from Errani et al. 2024b, showing the mean density enclosed within the 3D half-light radius for Local Group dwarf galaxies (squares) and globular clusters (circles). The grey band highlights "region B" from Fig. 8.1, where the two classes overlap. *Right panel:* Members of some systems from this highlighted region are shown in the metallicity ([Fe/H])–radial velocity (RV) plane, excluding all detected binaries. We also compute rough estimates of the velocity and metallicity dispersions, in the same way as for the systems analyzed in this work, based on the members plotted. Data points are shown for Tri2 (Venn et al., 2017a; Kirby et al., 2017), Boo2 (Koch, 2009; Ji et al., 2016; Bruce et al., 2023), Leo5 (Collins et al., 2017; Jenkins et al., 2021; Mutlu-Pakdil et al., 2019), Pis2 (Kirby et al., 2015), Ret2 (Simon et al., 2015), Seg1 (Simon et al., 2011; Frebel et al., 2014; Norris et al., 2010), Seg2 (Kirby et al., 2013a), IC4499 (Dalessandro et al., 2018), NGC2419 (Cohen & Kirby, 2012), NGC5053 (Boberg et al., 2015), and Pal5 (Smith, 1985; Smith et al., 2002).

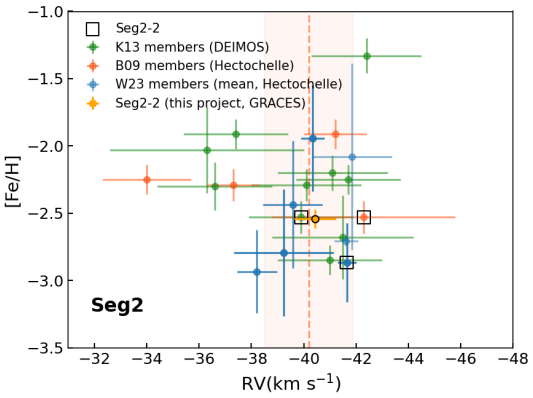

Figure 8.5: Members of the Seg2 ultra-faint dwarf galaxy shown in the metallicity ([Fe/H])–radial velocity (RV) plane. Members, excluding HB stars, identified in different studies are marked: orangered points indicate the velocity measurements from Belokurov et al. (2009) with metallicity measurements from Kirby et al. (2013a); a dashed line and shaded region show the velocity measurement for an RGB member (Seg2-064) that was not observed by Kirby et al. (2013a) and therefore lacks a metallicity measurement; green points are from Kirby et al. (2013a), and blue points are from Walker et al. (2023), with selection based on CMD position, proper motion, metallicity, and radial velocity from their spectroscopic sample. We also include the velocity and metallicity measurements of the Seg2-2 member star, derived from CaT lines using the GRACES spectrograph in this study, adding an additional instrument to the comparison. This star, highlighted with a black box, is the only one cross-matched across all datasets.

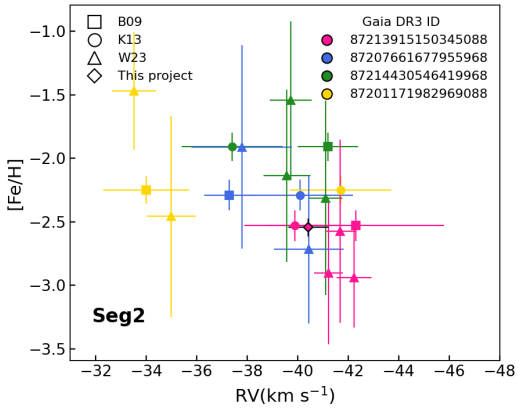

Figure 8.6: Seg2 members in the metallicity–radial velocity plane, cross-matched across different studies. Data points are color-coded by the stars' Gaia DR3 IDs (see legend) and shaped according to the study in which they were analyzed: squares represent data from Belokurov et al. (2009), circles from Kirby et al. (2013a), triangles from Walker et al. (2023) (individual epoch measurements), and the diamond shows our measurement based on the GRACES spectrum.

report a systematically lower [Fe/H] for Star40 compared to the values from Venn et al. (2017b) and Kirby et al. (2017).

A striking feature of the system is the metallicity outlier star31, confirmed as a member by Kirby et al. (2017), which also lies at a large spatial offset, as shown in the left panel of Fig. 8.7. I additionally include star0, selected from the spectroscopic sample of Walker et al. (2023) based on its CMD position, proper motion, radial velocity, and metallicity. While its membership remains uncertain due to its significant spatial separation ($> 4, r_{\rm ell}$), its metallicity, similar to that of star31, makes it a potentially important data point. If confirmed as a member, it would further support the presence of a significant metallicity spread in the system.

Another potential indicator of metallicity dispersion is star46, the confirmed binary. However, as shown in the figure, its derived metallicity is sensitive to the adopted stellar parameters. While still within the uncertainties reported by Venn et al. (2017b), Ji et al. (2019) used slightly different parameters, leading to a higher metallicity estimate. In contrast, the metallicity derived for star40 in the same high-resolution analysis was lower, and this difference was used as supporting evidence for metallicity dispersion – an arguments in favor of Tri2 being classified as an UFD.

I note that a similar situation, where the significance of inferred metallicity dispersion depends sensitively on the adopted stellar parameters in high-resolution analyses, may also apply to the most metal-rich member star in Tuc3 (Marshall et al., 2019), as previously discussed in Section 6.4.

Tri2 is therefore another example of a system with unresolved velocity dispersion, outlier-dependent metallicity dispersion, and unknown binary fraction.

Other systems in Region B

Some other examples of systems from this Region, with either confirmed binaries or hints of the presence of such, include:

Leo5: The velocity dispersion of Leo5 was measured as $0.30^{+0.14}_{-0.09}$ km s^{-1}using 8 member stars (Jenkins et al., 2021). Two additional stars were identified as binaries. Notably, these binaries stood out only when multiple studies were compared, as velocity variations were not evident when considering VLT measurements alone, taken seven months apart (see their Fig. 12).

Boo2: Boo 2 has 12 reported members (Bruce et al., 2023), two of which were confirmed as binaries by comparing measurements from Koch 2009 (April 2007) and

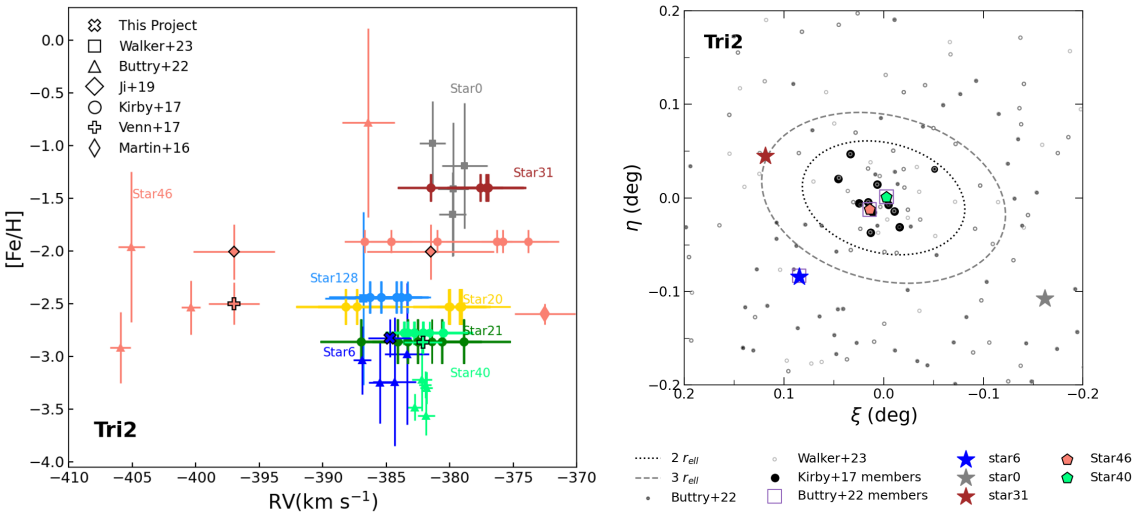

Figure 8.7: *Left*: Individual epoch observations of Tri2 members in the metallicity–radial velocity plane. Data points from Martin et al. (2016a); Venn et al. (2017b); Kirby et al. (2017); Ji et al. (2019); Buttry et al. (2022) are color-coded by individual stars, labeled according to Martin et al. (2016a), and shaped according to the study in which they were analyzed. Measurements from high-resolution analyses are shown with black edges. I also include our own measurement for star6, obtained with Gemini/GRACES. The grey point (star0) marks a possible member identified by us based on its CMD position, proper motion, and radial velocity from the Walker et al. (2023) sample. *Right*: On-sky positions of Tri2 members in projected coordinates. Dotted and dashed lines indicate 2 and 3 elliptical radii, respectively. Two stars with high-resolution abundance measurements—one of which is the binary star46—are highlighted with pentagon symbols. Three distant (possible) members—star31, star6, and star0—are marked with star symbols. All highlighted members are shown in the same colors as in the left panel. Other members from Kirby et al. (2017) are shown as black circles. Notably, the metallicity outlier star31, as well as the possible member star0, are among the most distant members of the system, while the metallicity of star46—another possible outlier—varies between high-resolution studies (Venn et al., 2017a; Ji et al., 2019) due to differences in the adopted stellar parameters.

Bruce et al. 2023 (June-July 2021). Excluding these newly identified binaries reduced the velocity dispersion to one-third of the previously reported value.

Peg4: The velocity dispersion for Peg4 was measured as $3.3^{+1.7}_{-1.1}\mathrm{km\,s^{-1}}$ based on seven spectroscopic members (Cerny et al., 2023c). Two additional stars were excluded as HB stars, while three others were omitted because their velocities deviated by more than $10\mathrm{km\,s^{-1}}$ from the system's mean velocity – suggesting they could be either non-members or binaries. A binarity analysis was not performed in that study, as the observations were conducted over only two consecutive nights.

This region, therefore, hosts systems that may lack reliable dark matter abundance estimates.

At the same time, it is important to note that additional classification efforts for several systems (Boo2, Tuc3 Tuc5, Ret2, Tri2, Seg2, Seg1, Car3, Hor1; see references in Fig. 4.2, Sgr2 (this thesis)) have included detailed chemical abundance studies. These have often revealed patterns – and in some cases, extremely low metallicities ([Fe/H] < -2.5) – that are typically associated with UFDs (with the exception of Sgr2 and Tuc3 as discussed in Sec. 6.4).

While chemical abundance analyses can effectively complement kinematic data in classifying stellar systems, they sometimes remain the primary or only available diagnostic. This is especially true for *Tucana V (Tuc 5)*, a marginally detected system with poorly constrained structural parameters (Conn et al., 2018). Nevertheless, high-resolution spectroscopy of three RGB stars by Hansen et al. (2024) revealed C-enhancement in one star and low Sr and Ba abundances in all three –chemical signatures consistent with known UFDs. In later sections, I discuss why such chemical evidence, though suggestive, may be insufficient on its own to confirm a dark matter-dominated origin.

Another valuable diagnostic is the resilience-to-tides analysis conducted by Pace et al. (2022), which was based on dynamical density estimates derived from velocity dispersion measurements (see their Fig.5). This method revealed clear signs of tidal disruption only for Tuc3 – which has an extremely small pericenter (∼1–3 kpc)—and possibly for Seg2, whose density lies near that of the Milky Way[3]. The study further noted that if velocity dispersions are overestimated, other satellites with small pericenters ($r_{\mathrm{peri}} < 30$ kpc), such as Seg1, Tri2, and Wil1, may also be undergoing disruption.

Several systems from this region were not included in the Pace et al. (2022) sample.

[3]Seg2 was also recently shown to have collided with the Cetus-Palca Stream (Foote et al., 2025).

Among them, Leo5 shows kinematic signatures consistent with impending dissolution (Collins et al., 2017), and Boo5 has a close pericenter ($r_{\rm peri} = 15$–20 kpc) that could lead to tidal elongation or stripping (Cerny et al., 2023a). Although Phoenix II (Pho2) was not flagged as disrupted by the density analysis in Pace et al. (2020), it exhibits clear tidal arms extending from its core (Jerjen et al., 2018b).

Such dynamical assessments are crucial, as velocity dispersion measurements become increasingly unreliable in systems already affected by tidal stripping.

Lastly, I note that the most extended known GC – *Pal 14* ($r_h = 46 \pm 3$pc) – enters this region. The detection of mass segregation (Frank et al., 2014) and the extension of its stellar distribution beyond more than $2\times$ its Jacobi radius (Sollima et al., 2011) have been used as evidence that the cluster was significantly more compact in the past, and may have been accreted from a now-detached or disrupted dwarf galaxy with a strong tidal field (Zonoozi et al., 2024). This provides an example of how star clusters can mimic dark-matter-dominated UFDs in their structural parameters, effectively "entering" the regions typically populated by the latter.

In the following subsection, I also highlight alternative pathways by which GCs may enter this region of parameter space, as suggested by N-body simulations.

8.4.2 Extended GCs mimicing DGs

Contenta et al. (2017) explored the contribution of dissolving star clusters to the population of ultra-faint stellar systems in the outer halo of the Milky Way using N-body simulations. They concluded that ultra-faint star clusters may contribute to both "populations" of faint ambiguous systems: those with half-light radii $r_h \gtrsim 20\,$pc (Region B) and the more compact ones with $r_h \sim 5\,$pc (Region E), albeit through different internal dynamical mechanisms. In particular, they showed that the retention of stellar-mass BHs in initially low-density clusters is essential for forming extended star clusters. This has been further supported for a sparse star cluster Palomar 5 (Gieles et al., 2021)[4]. Furthermore, dynamical properties of these clusters closely resemble those of DGs: high-inferred mass-to-light ratios due to binaries, binary properties mildly affected by dynamical evolution, no observable mass segregation[5]

[4] I note that Wang et al. (2024) also proposed an alternative scenario involving a black-hole-free low-density cluster – a hypothesis that may be tested by examining the fraction of soft binaries in Pal5.

[5] This is consistent with the lack of significant mass segregation detected for systems in Region B in the analysis by Baumgardt et al. (2022).

and flattened stellar mass function. These similarities, along with the overlapping densities depicted in Fig. 8.4, further motivate a more detailed evaluation of the dark matter content in such systems.

As further evidence of such "mimicking", Domínguez et al. (2016) have shown that for Seg1 — a system in this region exhibiting an extremely high mass-to-light ratio— the observed kinematics can be entirely reproduced by a dissolving, dark-matter-free progenitor. In this scenario, the elevated velocity dispersion arises almost exclusively from unbound stars. More recently, Lujan et al. (2025) demonstrated that most of the "dark" mass in Seg1 could plausibly originate from a central $\sim 10^5\ M_\odot$ black hole rather than a traditional dark matter halo. This serves as a compelling example of how kinematic analyses alone may be insufficient to distinguish between dark-matter-dominated and dark-matter-free systems. While in systems like Seg1 it is still feasible to perform complementary chemical analysis using a reasonable number of spectroscopic members[6], this becomes increasingly difficult at fainter magnitudes. As a result, the distinction between dark-matter-free and dark-matter-dominated scenarios becomes progressively more ambiguous.

8.5 Region C

As we move toward fainter magnitudes, it becomes increasingly difficult to collect sufficiently large spectroscopic samples. Most systems in this region lack confident measurements of velocity and metallicity dispersions, motivating the use of alternative classification tools, which sometimes yield conflicting results. These include chemistry, mass segregation, and tidal stability, each discussed below.

8.5.1 Chemistry

The CMDs of such faint systems often still contain a few ($\sim$ 1–3) bright RGB stars, enabling the derivation of high-resolution abundances. A good example is the faintest system in this region – Cetus II (Cet2). As shown in the figure, this system is currently classified as a UFD, based purely on the chemical analysis of a single RGB star, particularly its low n-capture element abundances ([Sr/Fe], [Ba/Fe] ~ -2[7]; Webber

[6]In particular, Seg1 exhibits distinctive UFD chemical signatures, including low [Sr/Ba] ratios, a large metallicity spread (from [Fe/H] = –3.8 to –1.4), and enhanced α-element abundances ([α/Fe] $\approx$ 0.5), based on spectroscopic analysis of seven member stars (Frebel et al., 2014).

[7]Note, however, that the [Sr/Ba] ratio would be close to the solar value.

et al. 2023). I note a comparable case for Tuc5 in Region B.

At the same time, a similar situation recently observed for two other ambiguous faint satellites from Region C – DELVE 1 and Eri3 studied by Simon et al. (2024) – did not lead to the same conclusions. Single stars observed in both systems exhibited significant C-enhancement ([C/Fe]$\sim +2$), low Sr and Ba abundances ([Sr/Fe]$= -1.62, -1.89$; [Ba/Fe]$= -1.37, -0.79$), and very low metallicities ([Fe/H]$= -2.8, -3.1$) — all consistent with a UFD scenario. However, the extreme compactness of these satellites precluded definitive classification, and the authors proposed an alternative scenario of carbon-rich primordial star clusters.

This lack of consensus and uniformity in interpreting the origin-defining power of these chemical patterns is further complicated by the inherent difficulty in understanding them (see discussions on possible sources of low n-capture abundances in Tarumi et al. 2021, as well as their interpretation as 'one-shot' enrichment by Frebel & Bromm 2012). It may be that these chemical signatures require refinement, especially when applied to faint, compact systems where the diagnostic power of chemical abundances is limited. In particular, additional observational and theoretical tests are essential to improve classification reliability in such challenging cases.

8.5.2 Mass Segregation

Interestingly, size is not the only cluster-like property of these systems. For example, Baumgardt et al. (2022) measured significant mass segregation in Eri3 ($\frac{R_{\rm bright}}{R_{\rm faint}} = 0.84 \pm 0.09$, with $P_{\rm Mseg} = 91.7\%$; see Section 7 for details), consistent with that observed in similar Milky Way GCs. Additionally, Conn et al. (2018) showed that the system must have always been that small, without experiencing significant mass loss, by fitting Eri3's LF with a Salpeter IMF.

Thus, Eri3 is a good example of an ambiguous case that leads to opposite conclusions when different classifiers are applied. If Eri3 is indeed a primordial star cluster, it raises important questions about the reliability of chemical diagnostics used to classify faint ambiguous systems. In particular, if primordial star clusters with metallicities below [Fe/H]$= -2.5$ dex have survived to the present day, what chemical abundance patterns would they be expected to exhibit? And how would these differ from those observed in currently known UFDs?

As seen in this context, the lack of confident and sufficiently large spectroscopic samples often necessitates the use of alternative photometric diagnostics — in par-

ticular, signs of mass segregation. However, identifying mass segregation signatures in UFD candidates is particularly challenging due to small sample sizes (see, e.g., Kim et al., 2016, for a discussion on mass segregation in Kim 3) and uncertainties in structural parameters, which can be further amplified by mass loss from tidal disruptions.

In addition to the intrinsic complexities of ultra-faint MW satellites, methods for quantifying mass segregation may suffer from biases and assumptions – such as the choice of mass bins, bin sizes, density profile models, lack of comparison with an unsegregated case, the identification of the system's center (see the introduction of Allison et al. 2009 and references therein, and Parker & Goodwin 2015 for comparative mass segregation), or the selection of stellar populations (see, e.g., Frank et al., 2014, for a discussion on mass segregation in Pal 14 estimated from blue stragglers versus the main sequence population). The depth of the photometric data further complicates interpretation; for example, the conflicting conclusions between Baumgardt et al. (2022) and Conn et al. (2018) regarding Eri3, and between Baumgardt et al. (2022) and Longeard et al. (2018) for Dra2, have been attributed to differences in photometric depth. An important further caveat is the role of black holes, which suppress stellar mass segregation (Weatherford et al., 2018; Aros et al., 2021b; Wu & Zhao, 2021; Dickson et al., 2024, also discussed earlier in Sec. 8.4.2).

Overall, the key implication of searching for this dynamical signature is as follows: if significant mass segregation is detected – consistent with expectations for dark-matter-free star clusters at a given relaxation time – it can serve as strong evidence in favor of the system being a star cluster.[8]. Conversely, the absence of detectable mass segregation alone is not sufficient to infer the presence of a dark matter halo.

Additional star cluster candidates in this Region that have been proposed to show mass segregation include Leavens 3, Kim2, Dra2.

Leavens 3 shows unresolved velocity and metallicity dispersions and, with [Fe/H] $= -1.8 \pm 0.1$ dex, stands out as a clear outlier from the dwarf galaxy mass–metallicity relation (Longeard et al., 2019). Its half-light radius was revised upward by $\sim$4 pc in Longeard et al. (2019) relative to the discovery paper (Laevens et al., 2015), reflecting a mass-segregated structure: deeper photometry revealed fainter, less massive stars at larger radii, yielding a more accurate size estimate. The observed mass segregation,

[8]Comparison with known globular clusters is crucial, as apparent mass segregation may arise from sample contamination (e.g., due to foreground stars or substructures, as discussed for Gru1 by Baumgardt et al. 2022)

structural properties, and relatively high metallicity all support a dark-matter-free star cluster origin.

For Kim2, independent studies by Kim et al. (2015a) and Baumgardt et al. (2022) reported evidence of dynamical mass segregation in the Kim2 system. Furthermore, Kim et al. (2015a) concluded that Kim2 has likely experienced mass loss due to the Milky Way's tidal field, based on its low luminosity and the presence of extra-tidal stars. It has been suggested that Kim2 may be analogous to Pal14 (see Region B).

For Dra2, only upper limits on the velocity dispersion have been obtained by Martin et al. (2016b) and Longeard et al. (2018). Similar to Kim2, Dra2 shows indications of tidal disruption, inferred from its derived pericenter (~ 21.3 kpc) and the detection of extra-tidal features (Longeard et al., 2018). A mass segregation analysis by Baumgardt et al. (2022) further revealed a significant signal, with $\frac{R_{\rm bright}}{R_{\rm faint}} = 0.78 \pm 0.07$ and a segregation probability of $P_{\rm Mseg} = 88.4\%$.

In summary, Eri3, Leavens 3, Kim2, and Dra2 – each located in Region C – may indeed be star clusters based on the *presence* of significant mass segregation signatures.

Mass segregation in low dark matter halos

The relaxation time of a stellar system is proportional to its crossing time, which is given by R/v, where R is the system's characteristic radius and $v = \sqrt{GM/R}$ is the typical stellar velocity. For a purely baryonic system, this leads to the scaling

$$t_{rh} \propto N \frac{r_h^{3/2}}{M_h^{1/2}},$$

where M_h is the total stellar mass, r_h is the half-light radius, and N is the number of stars (see Eqs. 1.35–1.38 in Binney & Tremaine).

However, when the total mass within r_h comprises both a (grainy) stellar component and a (smooth) dark matter component, the scaling can be rewritten as

$$t_{rh} \propto \frac{(M_h r_h)^{3/2}}{N \langle m \rangle^2},$$

where $M_h = M_{\rm dyn}(r < r_h)$ is the dynamical mass enclosed within the half-light radius and $\langle m \rangle$ is the mean stellar mass[9] (see Eq. 5 of Errani et al. (2025)).

[9]The original scaling is recovered by substituting $N\langle m \rangle = M_h$.

In other words, for a system with a fixed number of stars and mean stellar mass, and at fixed half-light radius, the presence of dark matter increases the relaxation time by a factor of $\Upsilon^{3/2}$, where $\Upsilon = M_{\rm dyn}/L$ is the dynamical mass-to-light ratio.

This implies that in compact systems –those with small r_h and therefore inherently short relaxation times – the addition of modest dark matter halo (i.e., a small increase in $M_{\rm dyn}$) can still lead to a dynamically relaxed, mass-segregated state.

This has been tested in the recent work by Errani et al. (2025) who demonstrated that the stellar component of galaxies can exhibit mass segregation in systems with low dark matter content (those with mass-to-light ratios $\Upsilon < 50$). In such systems, smaller sizes (i.e., shorter relaxation times) are associated with a higher degree of mass segregation at lower Υ values. Analyzing Eri3, they found tentative evidence for mass segregation at a level of $\frac{r_{\rm high}}{r_{\rm low}} \approx 0.93$[10] at $\Upsilon = 10$. For reference, Baumgardt et al. (2022) detected mass segregation at $\frac{r_{\rm high}}{r_{\rm low}} = 0.84 \pm 0.09$ with a KS test significance of $P_{MS} = 91.7\%$[11] These results suggest that the observed segregation in Eri3 could still be consistent with the presence of a dark matter halo – albeit a very low-mass one with $\Upsilon < 10$.

It is important to note that in such faint systems with a small number of member stars, radial measurements of mass segregation can be significantly affected by statistical fluctuations and stochasticity (see, e.g., Fig. 3 of Errani et al. 2025). Therefore, alternative approaches such as the minimum spanning tree (MST) method (Allison et al., 2009) may offer more robust and insightful constraints on the presence and extent of mass segregation in these systems.[12].

Finally, a competing dynamical process – gravothermal expansion driven by heating from the dark subhalo population, as described by Peñarrubia et al. 2025 – may further inhibit the development of mass segregation in such dark matter dominated systems by increasing the r_h, and consequently, the system's crossing time.

[10]Converted to match the scale used by Baumgardt et al. (2022) for comparison.

[11]It is worth noting that Errani et al. (2025) did not assess the statistical significance of the measured mass segregation.

[12]In this method, mass segregation is quantified by comparing the total edge length of the MST connecting the N most massive stars to the distribution of MST lengths connecting many sets of N randomly selected stars. This method is independent of assumptions about the system's center, as it focuses on detecting spatial clustering among the most massive stars, and thus also mitigates uncertainties related to determining the faint system's centers from observations.

8.5.3 Tidal Disruption

Tidal disruption plays a critical role in understanding the ambiguous nature of the faintest Milky Way satellites. First, a tidally stripped system may exhibit inflated velocity dispersions that mimic the dynamical signature of dark matter. Second, the identification of tidal stripping signatures can help explain the unusually extended sizes observed in some systems lacking dark matter. Third, such analyses provide valuable insight into the dark matter content itself: if a system shows evidence of tidal disruption yet would be expected to resist it if dark matter were present (i.e., had a higher mass-to-light ratio), this suggests the system is likely dark-matter-free. Conversely, if a system shows no signs of disruption despite being on an orbit that would not allow survival without dark matter, it is more plausibly a dark-matter-dominated dwarf galaxy (as discussed in Sec. 1.4.2).

This latter scenario offers a stringent test for the presence of dark matter, particularly in systems where other classification tools are inapplicable or unreliable.

Here, I assess tidal resilience in two ways. In Fig. 8.8, I illustrate limiting radii corresponding to galactocentric distances of 20, 30, 40, 50, and 80 kpc. Following Baumgardt et al. (2022), I define the limiting radius as $R_{\rm Lim} = 0.25 R_{\rm Tide}$, representing the maximum radius a system can reach before undergoing tidal disruption. The tidal radius for a cluster on a circular orbit within a spherically symmetric isothermal external potential (King 1962; Baumgardt & Makino 2003) is given by:

$$R_{\rm Tide} = \left(\frac{M_h}{2V_C^2}\right)^{1/3} R_{GC}^{2/3} \tag{8.1}$$

I adopt a mass-to-light ratio of ~ 2, appropriate for old stellar populations. For circular velocities V_C at each galactocentric distance R_{GC}, I use values of 210, 190, 187, 183, and 170 km s^{-1} for respective distances (Cautun et al., 2020; Deason et al., 2020; Zhou et al., 2023). Ambiguous systems are color-coded based on their proximity to 80 kpc – the largest distance for which I compute $R_{\rm Lim}$, and which also conveniently lies near the dividing line between ambiguous systems and UFDs. For visual clarity, each limiting line is color-coded to match the systems located at the corresponding galactocentric distance. This allows the reader to easily determine whether a system lies to the left of its matching line – suggesting it is likely unaffected by tides – or to the right, indicating it may be tidally disrupted unless supported by a dark matter halo.

In Fig. 8.9, I calculate the mean half-light densities for ambiguous systems from

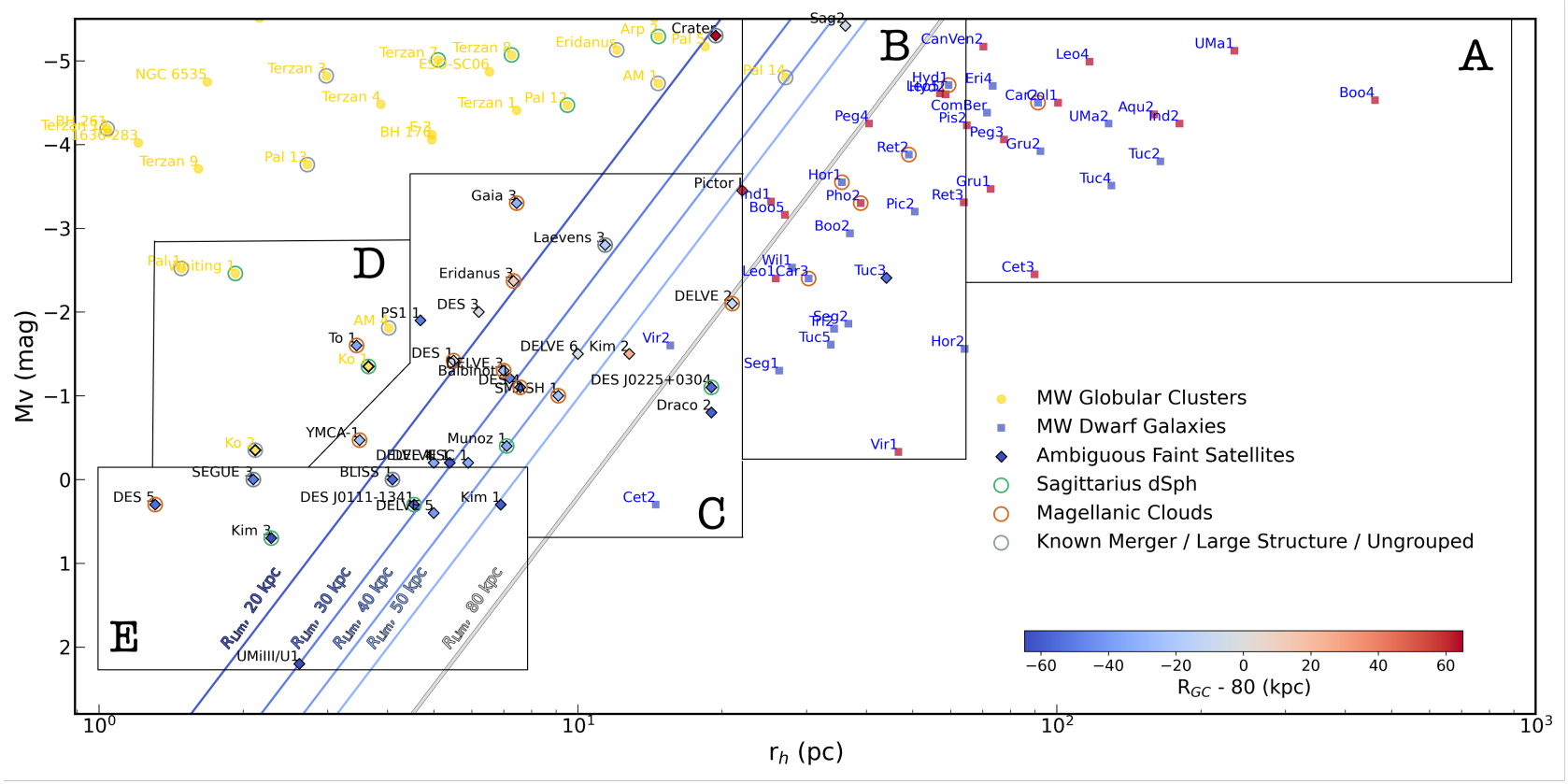

Figure 8.8: Same as Fig. 8.1; solid lines show the limiting radii for dark-matter-free stellar systems at various Galactocentric distances, with color indicating proximity to $R_{\rm GC} = 80$ kpc (see text for details). Ambiguous systems are color-coded similarly, according to their location relative to this $R_{\rm GC} = 80$ kpc, with redder colors indicating systems farther away and bluer colors indicating those closer. UFDs are color-coded to reflect their typically greater Galactocentric distances. Markers are encircled to indicate specific associations: green for Sagittarius dSph, brown for LMC/SMC satellites, and grey for clusters either tied to major merger events or deemed ungrouped – those lacking connections to known mergers or the MW disc/bulge, potentially indicating other ex-situ origins (as described in the analysis by Callingham et al. (2022).

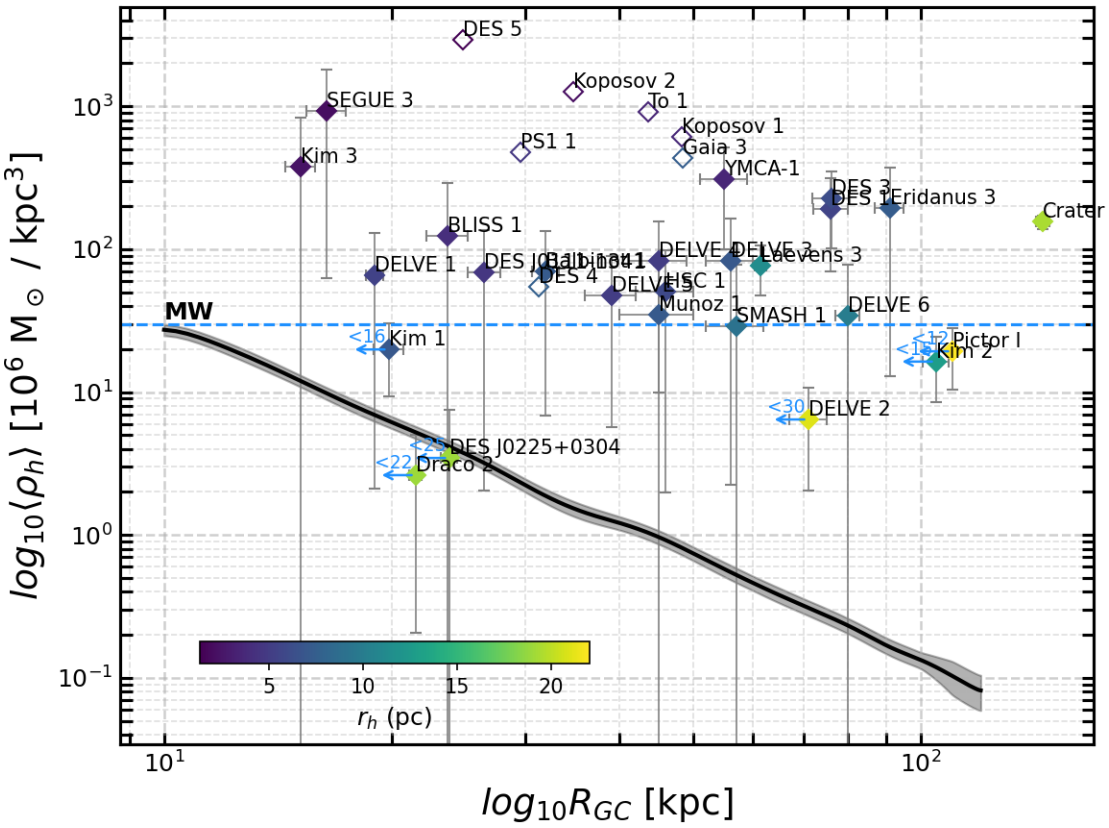

Figure 8.9: Mean half-light densities ($\langle\rho_h\rangle$) of ambiguous satellites in Regions C–E (as defined in Fig. 8.1), calculated under the assumption of no dark matter. Marker colors indicate half-light radius (r_h); open symbols denote systems lacking reported uncertainties on M_V and/or r_h, and hence on ρ_h. The thick black line and surrounding grey shaded region represent the Milky Way density profile as a function of galactocentric distance ($R_{\rm GC}$), derived from galaxy rotation curve models (Cautun et al., 2020; Deason et al., 2020; Zhou et al., 2023). Systems lying below the light-blue dashed line, given their $\langle\rho_h\rangle$ uncertainties, may be susceptible to tidal disruption by the Milky Way's gravitational field if their pericenters fall below a critical $R_{\rm GC}$ value. This threshold – where the satellite crosses below the Milky Way density curve – is marked with light-blue arrows for each object. Note that some systems (Draco2 and DESJ0225+0304) currently lie below the Milky Way density threshold, implying that they should exhibit signs of tidal disruption unless they are embedded within dark matter halos (see text for further discussion).

Regions C–E and compare them to the Milky Way's average density profile across a range of galactocentric distances, as given by Equations 1.2 and 1.3. While such comparisons are typically made using the Milky Way density at each system's *pericenter*, most of these systems lack well-constrained orbital solutions. Therefore, I first compute the Milky Way density profile as a function of galactocentric distance, and then assess which systems could be susceptible to tidal disruption under the dark-matter-free assumption. Systems that either already lie below the Milky Way density curve or could plausibly fall below it within their uncertainties, given certain orbital configurations, are marked with light-blue arrows indicating threshold pericenter values.

These two approaches – comparing half-light to tidal radii and analyzing mean densities – are combined to provide improved insight into each system's likely origin, supported by existing observational data. Below, I discuss specific cases from Region C:

Draco 2: As previously noted, Draco 2 shows tentative observational signs of tidal disruption (Longeard et al., 2018), and mass segregation confirms its classification as a star cluster (Baumgardt et al., 2022). Our analysis supports both conclusions: Fig.**??** shows that the system lies to the right of the line corresponding to its distance ($\sim$20 kpc), implying it may be disrupted, while in Fig.8.9 it falls below the Milky Way density profile, reinforcing this interpretation.

DES J0225+0304: This system also lies below the Milky Way density curve in Fig.8.9, and in Fig.8.8 appears to exceed its limiting radius. Thus, I support the tentative conclusion by Luque et al. (2017) that DES J0225+0304 may be an ultrafaint star cluster, possibly stripped from the Sagittarius dSph.

I also note that both Draco 2 and DES J0225+0304 exhibit relatively large r_h values compared to most other faint ambiguous systems.

Kim 1: Kim 1 has relatively low uncertainties on its density and is located at a relatively small galactocentric distance, making it potentially prone to tidal disruption if its pericenter is $\lesssim$16 kpc. This is consistent with its significantly large half-light radius compared to its limiting radius, and supports its classification as a dissolving star cluster, as proposed by Kim & Jerjen (2015) based on its high ellipticity and irregular outer isophotes.

DELVE 2: DELVE 2 lies just above its limiting radius in size and may fall below the Milky Way density profile for pericenters $\lesssim$30 kpc. However, no obvious tidal features are currently observed, and its possible association with the Magellanic Clouds

complicates the interpretation (discussed below).

Kim 2: Kim 2 shows observational evidence of tidal disruption and mass segregation, suggesting it is a disrupted star cluster. My density analysis does not rule out this interpretation, as Kim 2 could be susceptible to tidal disruption for pericenters $\lesssim$15 kpc.

Finally, I note that for several systems, density analysis is not informative due to large uncertainties that could place them below the Milky Way density estimate at their current positions. These include DELVE 1, BLISS 1, *DELVE 4*, *SMASH 1*, and DELVE 6. Improved constraints on luminosities and orbital parameters will be crucial for future analyses. A complementary tidal radius analysis for *DELVE 6* rules out a disrupted state, while for SMASH 1, this test may be inapplicable, as the system shows signs of tidal disruption caused by the LMC (Martin et al., 2016c, ,also discussed below).

Conversely, there are systems whose well-constrained parameters confidently rule out the tidal disruption scenario, as their high densities place them well above the Milky Way's average density profile. Such systems include DES1 (in agreement with the luminosity function fit analysis by Conn et al. 2018), DES3, YMCA-1, and Leavens 3 (consistent with conclusions by Longeard et al. 2019) – all in good agreement with the tidal radius analysis done here.

Future progress will rely on improved orbital solutions from proper motion measurements and deeper photometric searches for tidal features, which will provide crucial insight into the dynamical states of these faint systems.

Tidal influence from LMC-SMC

The tidal resistance analysis presented here does not incorporate the gravitational influence of the Magellanic Clouds. In Fig.8.8, systems with possible associations to the LMC or SMC are marked with brown circles. These include DES5, To1, Gaia3, and DES4 (Torrealba et al., 2019); YMCA-1 (Piatti & Lucchini, 2022); Eri3 and DES1 (Conn et al., 2018); DELVE3 (Cerny et al., 2023a); SMASH1 (Martin et al., 2016c); and DELVE2 (Cerny et al., 2021). The observed r_h of these satellites may be influenced by tidal interactions with the LMC–SMC system, which are not accounted for in the Milky Way-only tidal analysis presented above.

8.6 Region D

A review of the objects in this region suggests they may be associated with disrupted star clusters, possibly of extragalactic origins.

8.6.1 Extragalactic Origin?

Two systems from this region – Koposov1 (Ko1) and Koposov2 (Ko2) – are of particular interest, having been studied in multiple works. Originally discovered by Koposov et al. (2007), both were classified as globular clusters based on their compact morphology and low luminosities, suggestive of significant tidal stripping. They were subsequently included in the updated catalog of Milky Way globular clusters by Harris (2010), with slightly revised structural parameters that nonetheless place them within the same region (Region D) of our classification scheme[13]. Deeper photometric observations by Paust et al. (2014) yielded tidal radii of 15 pc and 10.7 pc for Ko1 and Ko2, respectively – $\sim 3\times$ their current half-light radii estimated. By fitting present-day mass functions consistent with a Salpeter slope, the authors argued that these systems show no clear evidence of tidal stripping. Instead, they proposed that Ko1 and Ko2 are intermediate-age open clusters[14] likely originating from the Sagittarius dwarf galaxy (Sgr dSph), based on their ages, metallicities, and spatial alignment with Sgr's stellar population and star formation history.

Interestingly, the other two clusters in this region – AM4 and Whiting 1 – have also been considered potential members of the Sagittarius dSph system (Carraro et al., 2007; Carraro, 2009), while Pal1 has been proposed to be associated with the Canis Major Overdensity (Forbes & Bridges, 2010; Sakari et al., 2011). This raises the tentative possibility that Region D may be preferentially populated by star clusters of non-Galactic origin. However, such associations are highly method-dependent. For instance, while Forbes (2020) linked AM4 to the Sagittarius system, Malhan et al. (2022) did not recover this connection, and a chemo-dynamical analysis by Callingham et al. (2022) instead associated AM 4 with the Sequoia merger event. In contrast, both Ko1 and Whiting 1 have consistently been associated with the Sgr dSph across multiple studies (e.g., Callingham et al., 2022; Malhan et al., 2022). Ko2, however, remains unassociated with any known accretion event or Galactic component and is

[13] In Fig. 8.1, 8.8, I adopt the structural parameters from Harris (2010) for these systems.

[14] Mass segregation analysis by Baumgardt et al. (2022) also revealed clear signatures of mass segregation in these systems, further supporting their dark matter–free nature.

classified as 'ungrouped' in Callingham et al. (2022).

The ambiguous system To1 in this region has also been recently proposed as an extragalactic star cluster. It has been tentatively linked to the Magellanic Clouds based on its sky position and physical characteristics (Torrealba et al., 2019).

To illustrate these associations, Fig. 8.8 highlights the systems connected to the major Milky Way satellites – the LMC-SMC (Magellanic Clouds) and Sgr dSph groups – using two distinct colors. Systems linked to other large structures or known merger events, as well as those lacking clear association with either the MW disc/buldge or any known accretion event (based on the classification by Callingham et al. 2022), are shown in a single color, as they collectively represent candidates of likely *ex-situ* origin[15]

As evident from the figure, regardless of the specific classification or method used, Region D appears to host clusters that are distinct from the Milky Way's *in-situ* population. These clusters may either be remnants of systems that were significantly stripped during the merger of their host galaxy with the Milky Way, or genuinely compact objects that formed in distinct environments and survived the merger thanks to their high density, experiencing only mild tidal disruption. Both scenarios are consistent with evidence of extra-tidal stars observed in Whiting1, AM4, and Pal1 (Carraro et al., 2007; Carraro, 2009; Niederste-Ostholt et al., 2010).

This raises the question of whether the boundaries of this region should be revised – either extended downward to include the faintest known Milky Way satellites (as discussed below) or rightward, where it overlaps with compact, ambiguous systems associated with dwarf satellites. These include YMCA-1 (possibly a stripped SMC cluster; Piatti & Lucchini 2022), Eri3 and DES1 (likely unstripped but tidally extended by LMC–SMC interactions; Conn et al. 2018), and Muñoz 1 (linked to the Sagittarius dSph (Callingham et al., 2022)).

8.6.2 Overlap with Open Clusters

This region also overlaps with the locus of open clusters (OCs) in the size–luminosity plane. OCs are typically younger, more metal-rich, and confined to the Galactic disc if formed *in situ*. Structurally, they are less dense than GCs, and thus occupy a slightly lower position in the r_h–M_V parameter space.

[15]Their extragalactic origin is further supported by the independent classification scheme of Belokurov & Kravtsov (2023), which also distinguishes between *in-situ* and *ex-situ* clusters.

As noted earlier, at least two clusters in this region (Ko1 and Ko2) have been reclassified as OCs rather than GCs. This reassessment is supported by their Salpeter-like present-day mass functions, which indicate minimal mass loss despite their relatively low densities, as well as by their younger ages (5–7 Gyr) and higher metallicities ([Fe/H] ≈ -0.6), determined by Paust et al. (2014) using isochrone fitting based on photometry several magnitudes deeper than that used by Koposov et al. (2007). Whiting1 is another candidate: it is among the youngest and most metal-rich clusters in the Galactic halo (6.5 Gyr, [Fe/H] = ˘0.65; Carraro et al. 2007). Given its association with the Sagittarius dwarf spheroidal galaxy (Sgr dSph), Whiting1 may also be an open cluster that was stripped from its host during accretion by the Milky Way.

Torrealba et al. (2019) suggested that several newly discovered, ambiguous systems in this region may also be open clusters. PS1 is one such candidate, and Mau et al. (2020) did not rule out this possibility for BLISS1. Similarly, Seg3 – once thought to be an old globular cluster (Fadely et al., 2011) – was re-estimated to have an age of ~ 3 Gyr by Ortolani et al. (2013), based on isochrone fitting that included subgiant branch stars, rendering its classification uncertain.

Better constraints on ages, metallicities, and potential extragalactic associations will be essential to resolve the nature of these objects. However, the distinction between open and globular clusters may be less critical if many of these systems formed in similar environments.

8.6.3 Formation in "Wet Mergers"

In addition to the scenario where clusters formed *ex-situ* and were later accreted by the Milky Way, some may have formed *during* infall events in gas-rich environments – so-called "wet mergers" (Ashman & Zepf, 1992). Such events could lead to a bimodal age distribution among accreted clusters, as suggested by Valenzuela et al. (2024), with younger clusters forming during gas-rich infall and thus exhibiting higher metallicities.

This could explain the presence of young, metal-rich clusters with extragalactic associations. To illustrate this, Fig.8.10 shows Milky Way OCs, GCs, and clusters associated with the Magellanic Clouds[16]. The youngest Milky Way outer halo clusters are highlighted in red. In addition to Region D systems (Ko1, Ko2, Whiting1, Pal1)

[16]The catalog by Bica et al. 2020 includes clusters located in the gas-rich Magellanic Bridge – a promising region to search for clusters potentially formed during a wet merger.

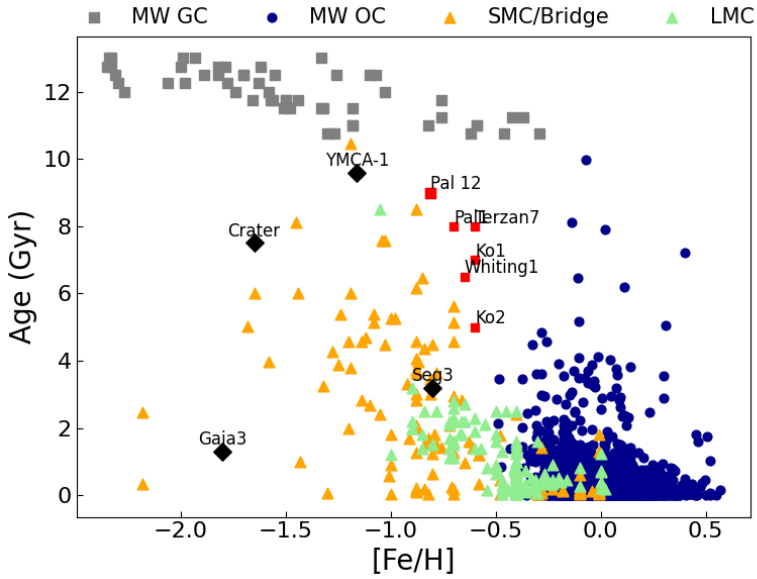

Figure 8.10: Open clusters (OCs) are from Dias et al. 2021, globular clusters (GCs) from VandenBerg et al. 2013, LMC clusters are from Palma et al. 2016, and SMC/Bridge clusters from Bica et al. 2020. The youngest Milky Way GCs are highlighted in red. In addition to Region D systems (Ko 1, Ko 2, Whiting 1, and Pal 1), all of which show evidence for an ex-situ origin (see text), Terzan 7 and Pal 12 also stand out as young outliers—both associated with the Sagittarius dSph (Malhan et al., 2022; Callingham et al., 2022). The youngest ambiguous satellites are also included; all exhibit signs of extragalactic origin (see text).

– all of which show evidence for an ex-situ origin (see Sec 8.6.1) – Terzan7 and Pal12 also stand out as young outliers, both associated with the Sagittarius dSph (Malhan et al., 2022; Callingham et al., 2022). The youngest ambiguous satellites are also included, all of which exhibit signs of extragalactic origin: Gaia3 is linked to the LMC (Torrealba et al., 2019), YMCA-1 to the SMC (Piatti & Lucchini, 2022), and both Crater and Seg3, while not clearly associated with known merger events, show evidence of ex-situ formation (Callingham et al., 2022; Belokurov & Kravtsov, 2023). See Sec. 8.7 (below) for more discussion on Seg3.

These outliers – many of which deviate not only in age–metallicity but also in M_V–r_h space (clusters from Region D and ambiguous satellites from Regions C and D) – align well with the properties of known extragalactic clusters. Whether formed as GCs or OCs within their host galaxies or during the mergers themselves, their distinct properties suggest a common extragalactic origin.

8.7 Region E

This region poses the greatest challenge in tracing system origins. These objects are among the faintest and most compact known, with few or no RGB stars on their isochrones, severely limiting the available observational data. Despite this, most discovery papers classify them as ultra-faint star clusters, mainly based on size. This has prompted discussion on how such low-luminosity systems form and survive – ranging from merger events where clusters endure the disruption of their host galaxies, to mass-loss processes and their timescales, and the survivability of compact clusters on current orbits.

In the sections below, I address these points and highlight the importance of also considering the "smallest galaxies" scenario. One potential discriminator in this regime is the analysis of factors shaping the MF slope. Another is to explore both dark matter-free and dark matter-dominated scenarios through N-body simulations, as demonstrated in the case of Ursa Major III / UNIONS 1, discussed in the final subsection.

8.7.1 Remnants of Merger Events or Heavily Stripped Dwarfs?

As discussed for Region D, some of the faint halo clusters have been proposed to be remnants of past merger events. These systems were likely accreted onto the Milky Way along with their host systems, which were subsequently disrupted by Galactic tidal forces (e.g., Forbes & Bridges, 2010; Leaman et al., 2013; Massari et al., 2017).

A similar origin may also be plausible for some systems in Region E. In particular, several clusters in this region exhibit tentative extragalactic associations. DES5, Kim3, BLISS1, and DESJ0111−1341 have been linked to either the Magellanic Clouds or the Sagittarius dwarf spheroidal galaxy. A chemo-dynamical analysis by Callingham et al. (2022) further confirmed the association of BLISS1 with the Helmi streams. Seg3 has also been suggested to be associated with the Hercules–Aquila Cloud (Belokurov et al., 2010; Ortolani et al., 2013), and it spatially overlaps with the overdensity reported by de Jong et al. (2010) (see also Fadely et al., 2011), as well as got *ex-situ* classification in .

Structural and stellar population properties of some systems support this scenario. For example, Kim 3 may have originated in the outskirts of a more massive globular cluster and is now undergoing tidal disruption in the Milky Way's potential. This is

suggested by its lack of binaries – contrary to the expected anticorrelation between cluster mass and binary fraction – its undefined center, and an overdensity ∼10 pc from the cluster (Kim et al., 2016). *Segue 3* has been proposed as the youngest star cluster in the Milky Way (∼3Gyr; Ortolani et al., 2013), possibly formed from enriched gas in a dwarf galaxy and later accreted. Its potential origin as an ex-situ open cluster is further discussed in Sec. 8.6.2. These systems may therefore represent a continuation of the Region D population – clusters of non-Galactic origin that have likely lost significant mass through dynamical interactions.

Alternatively, some of these systems may be "microgalaxies" –heavily stripped remnants of early-accreted satellite galaxies (Errani & Peñarrubia, 2020; Errani et al., 2024a). Tidal evolution tracks in the size–luminosity plane, as shown by Errani et al. (2024a), demonstrate that the trajectories of these tidal descendants are highly sensitive to the progenitor's distribution of stellar binding energies. The track closest to the ambiguous systems in Region E corresponds to progenitors with higher initial luminosities and/or surface brightnesses than typical dSphs with log $2D$ stellar density profiles.

To further explore these two scenarios, I examine the positions of the ambiguous systems in the metallicity-luminosity plane. This is motivated by: (a) the luminosity-metallicity relation of Local Group dwarf galaxies, which is used to estimate the luminosity of a stream's progenitor (Kirby et al., 2013b); and (b) the observation that many ambiguous systems in this region exhibit relatively high metallicities compared to expectations for dwarf galaxies at these luminosities, making their clustering in this space potentially insightful.

Clustering in Luminosity-Metallicity Plane

It is well established that the scatter in the luminosity–metallicity relation for dwarf galaxies increases toward the faint end (Simon, 2019a). Nevertheless, Fig. 8.11 reveals a distinct clustering (highlighted by the grey-filled polygon) at [Fe/H] $\gtrsim -1.8$, lying above the expected scatter for UFDs at comparable luminosities. While this may partly reflect an intrinsic increase in scatter among dwarfs at low M_V, additional diagnostics suggest that most (if not all) of these outliers are more consistent with star clusters.

The following systems support this interpretation: *Ko1, Ko2, Whiting 1, Pal 1, AM 4* – likely ex-situ clusters accreted from the Sagittarius dSph or similar pro-

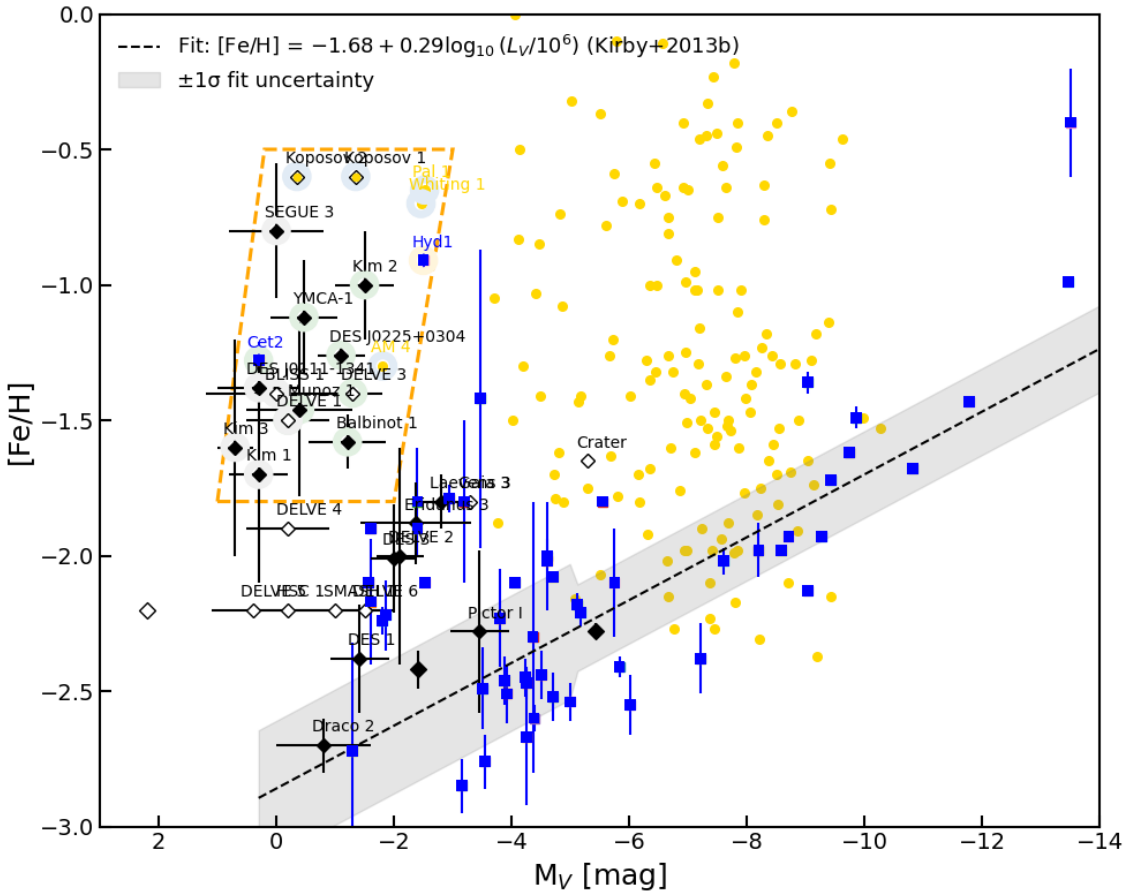

Figure 8.11: Luminosity–metallicity plane showing nearby galaxies (blue squares), Milky Way globular clusters (gold circles), and ambiguous systems (black diamonds; open markers indicate systems without reported [Fe/H] uncertainties). References are the same as in Fig. 1.1. The luminosity–metallicity relation for classical dwarfs is shown as a red dashed line. The scatter in the relation clearly increases below $M_V \lesssim -5$. A group of significant outliers with higher metallicities is highlighted by the dashed polygon, each circled in a color corresponding to the region they lie in (see text for details). Note that for Cet2, I adopt the photometric metallicity estimate from Conn et al. (2018), which is higher than the spectroscopic measurement of [Fe/H] = −2.3 for a single RGB member reported by Webber et al. (2023).

genitors (Region D); *SEGUE 3* – a probable cluster formed within a dwarf galaxy, showing low [Fe/H] dispersion, extra-tidal stars, and signs of mass segregation (Fadely et al., 2011; Ortolani et al., 2013); *Kim 3* – the remnant of a more massive star cluster, chemo-dynamically associated with the Sagittarius dSph and showing evidence of tidal stripping (Callingham et al., 2022; Kim et al., 2016); *Kim 2* – shows mass segregation and tidal disruption features (see Sec. 8.5); *Kim 1* – a dissolving cluster, based on structural parameters and tidal disruption analysis presented Sec 8.5.3; *DES J0225+0304* – tentatively associated with the Sagittarius dSph, and exhibiting signs of tidal dissolution consistent with my density analysis under the assumption of a dark matter-free system; *Balbinot 1* – a mass-segregated star cluster (Baumgardt et al., 2022); *YMCA-1* – cluster srtipped from SMC by LMC (Piatti & Lucchini, 2022)

Among systems lacking definitive signs of cluster/dwarf origin but showing strong extragalactic associations are: *Munoz 1* (chemo-dynamically linked to the Sagittarius dSph; Callingham et al. 2022), *BLISS 1* (associated with the Helmi streams; Callingham et al. 2022), and *DES J0111−1341* (tentatively linked to the Sagittarius dSph; Luque et al. 2017).

Finally, two systems classified as UFDs fall within this metallicity–luminosity grouping: *Hydra I (Hyd 1*, Region B) and *Cetus II* (*(Cet 2)*, Region C). Hyd 1 has been interpreted as a heavily disrupted dwarf galaxy that has lost over 99% of its stellar mass (Hargis et al., 2016). Its progenitor is estimated to have had a stellar mass of $M_* \sim 10^9\ M_\odot$, comparable to that of the present-day Fornax dSph, making Hyd 1 a strong candidate for a "microgalaxy", in the sense proposed by Errani et al. (2024a). The star cluster scenario was originally disfavored due to the absence of known clusters with similar age and metallicity (∼5–6 Gyr; [Fe/H] = −0.9). However, Hyd1 would fit well within the extragalactic population of clusters shown in Fig.8.10. Hargis et al. (2016) also noted that, under the cluster scenario, Hyd 1 would likely have formed within a dwarf galaxy that was later accreted by the Milky Way – consistent with the origin scenarios proposed for many systems in this metallicity–luminosity grouping. Later, Patel et al. (2020) also demonstrated that Hyd 1 has been dynamically bound to the Magellanic Clouds for at least its two most recent orbital periods.

Cet 2 was classified as a UFD primarily based on chemical abundances from its brightest member (see Sec. 8.5.1). However, Conn et al. (2018) derived a relatively high photometric metallicity ([Fe/H] = −1.28), while spectroscopic analysis by Webber et al. (2023) found a much lower metallicity ([Fe/H] = −2.3) for the only RGB

star identified. If this value is representative of the system, it would place Cet 2 lower in the metallicity–luminosity plane, outside the 'cluster' and more in line with typical UFDs.

Measurement Caveats

It is important to note that most of the systems considered here have metallicities (and ages) inferred from isochrone fitting, which is highly uncertain given the very small number of member stars and often absence of RGB members. Deeper photometry and/or the inclusion of new members may reveal significantly different metallicities, as demonstrated for Ko1, Ko2, and SEGUE 3. Spectroscopy of the brightest members can also lead to revised estimates, as discussed above for Cet2. Additionally, under the star cluster scenario, these systems are expected to be mass segregated due to their short relaxation times (discussed below). As a result, shallow photometry may miss low-mass stars in the outskirts, leading to underestimated values of r_h and M_V (e.g., see discussion for Leavens 3 in Sec 8.5.2). Thus, while clustering in the luminosity–metallicity plane can offer valuable insights, such patterns must be interpreted with caution.

Nevertheless, multi-criteria analysis has proven effective in shedding light on the origins of these systems – not only in determining whether a system is a dark matter-free star cluster, but also in distinguishing between clusters formed *in situ*, and those possibly accreted from dwarf galaxies or formed in tidal streams. At the same time, size alone is not a reliable discriminator between clusters and dwarfs in this regime, as heavily stripped dwarf galaxies can overlap with clusters in the size–luminosity plane, much like extended clusters and larger dwarfs (see Sec. 8.4.2).

I therefore tentatively propose that some of the systems in Region E may represent a continuation of Region D, potentially forming a population of accreted star clusters. Better constraints on the systems' parameters, along with complementary analyses, may help clarify their nature.

8.7.2 Evaporation Timescales

It has been suggested that, given their current stellar masses and sizes, the evaporation timescales (i.e., the time over which stars in a star cluster escape the system due to two-body relaxation) of these clusters are shorter than their observed ages, implying that evaporation may play a significant role in their evolution (Koposov et al., 2007;

Fadely et al., 2011) and subsequently on their apparent physical properties.

In order to explore the long-term dynamical evolution of these systems, I estimate their survival timescale in their current evolutionary state, by computing the evaporation timescale following Koposov et al. (2007). Specifically, I compute $t_{ev} = 12t_{rh}$, where t_{rh} is the half-mass relaxation time given by Equation 7.2 of Meylan & Heggie 1997:

$$t_{\rm rh} = 0.138 \, \frac{M^{1/2} \, r_h^{3/2}}{\langle m \rangle \, G^{1/2} \, \ln \Lambda} \tag{8.2}$$

where M is the total mass of the cluster (I use M/L ratio ~ 2 throughout the thesis), r_h is the half-mass radius (I assume it equals half-light radius), $\langle m \rangle$ is the mean stellar mass of stars in the cluster (I use $\langle m \rangle \sim 0.35 M_{\odot}$, following Baumgardt et al. 2022), G is the gravitational constant, and $\Lambda \simeq 0.4N$, where N is the total number of stars in the cluster ($N = \frac{M}{\langle m \rangle}$).

The final results for each faint ambiguous system are presented in Table 8.2. As a consistency check, I compare my evaporation time estimates with literature values for systems where $t_{\rm ev}$ has previously been computed. For Ko 1 and Ko 2, my $t_{\rm ev}$ estimates are $\sim$0.2 Gyr lower than those of Koposov et al. (2007), likely due to differences in the adopted r_h and M_V, which I take from the Harris (2010) catalog. For DELVE 1, only my upper estimate of 2.8 Gyr is consistent with the 3 Gyr reported by Mau et al. (2020). The discrepancy likely stems from differences in the adopted mean stellar mass $\langle m \rangle$ and total number of stars N. Finally, for SEGUE 3, Fadely et al. (2011) report $t_{\rm rh} \approx 0.14^{+0.15}_{-0.05}$ Gyr, about 0.1 Gyr higher than my estimate. This offset can be attributed to the choice of Coulomb logarithm; Fadely et al. (2011) use $\ln(0.02N)$, whereas I adopt $\ln(0.4N)$. When I use their convention, I reproduce their result.

Overall, my generalized calculations are in good agreement with literature values obtained through more system-specific methods, and any discrepancies do not significantly impact the comparison with current age estimates. These calculations clearly indicate that none of the systems in Region E could have preserved their present-day structural and dynamical configurations throughout their entire lifetimes if they are low M/L star clusters. Their short relaxation times further imply a high degree of mass segregation. Combined, these factors would have led to the preferential loss of low-mass stars, resulting in steeper present-day mass functions – consistent with the observed anticorrelation between mass function (MF) slope and relaxation time in Milky Way globular clusters (Hilker et al., 2020). This topic will be explored in more

Table 8.2: Relaxation time, evaporation time, and mean density within r_h for each known ambiguous system. The evaporation time is estimated as $t_{\rm ev} = 12\,t_{\rm rh}$.

Name	Age [Gyr]	$t_{\rm rh}$ [Gyr]	$t_{\rm ev}$ [Gyr]	$\log\langle\rho_h\rangle$ [10^6 $M_\odot$ / kpc^3]
Koposov 2	5.0[a]	0.04	0.48	3.10
Koposov 1	7.0[a]	0.12	1.45	2.79
SEGUE 3	$12.0^{+1.5}_{-0.4}$[b] / $3.2^{+0.5}_{-0.5}$[c]	0.04 ± 0.02	0.43 ± 0.20	2.97 ± 0.40
Munoz 1	12.5[d]	0.25 ± 0.15	3.00 ± 1.82	1.54 ± 0.53
Balbinot 1	$10.07^{+0.05}_{-0.03}$[e]	0.32 ± 0.15	3.86 ± 1.74	1.85 ± 0.39
Kim 1	12.0[f]	0.20 ± 0.05	2.39 ± 0.63	1.30 ± 0.23
Kim 2	$11.5^{+2.0}_{-3.5}$[g]	0.83 ± 0.20	9.99 ± 2.41	1.21 ± 0.21
Draco 2	12.0[h]	1.22 ± 0.56	14.68 ± 6.76	0.42 ± 0.40
Crater	7.5[i]	5.63 ± 0.31	67.61 ± 3.75	2.19 ± 0.05
SMASH 1	13.0[j]	0.43 ± 0.37	5.16 ± 4.38	1.46 ± 0.74
Kim 3	$9.5^{+3.0}_{-1.7}$[k]	0.03 ± 0.02	0.42 ± 0.25	2.58 ± 0.53
DES J0111-1341	$11.0^{+0.5}_{-0.5}$[l]	0.11 ± 0.05	1.28 ± 0.62	1.84 ± 0.42
DES J0225+0304	$11.0^{+0.5}_{-0.5}$[l]	1.34 ± 0.78	16.02 ± 9.33	0.54 ± 0.51
Eridanus 3	12.5[m]	0.48 ± 0.22	5.71 ± 2.66	2.29 ± 0.41
DES 1	11.2[m]	0.23 ± 0.07	2.75 ± 0.87	2.28 ± 0.28
DES 3	12.6[n]	0.33 ± 0.09	3.95 ± 1.09	2.36 ± 0.24
Pictor I	11.8[o]	3.55 ± 0.82	42.59 ± 9.85	1.29 ± 0.20
To 1	–	0.12	1.44	2.96
Laevens 3	$13.0^{+1.0}_{-1.0}$[p]	1.06 ± 0.20	12.73 ± 2.43	1.88 ± 0.17
DES 4	–	0.34	4.04	1.74
PS1 1	–	0.21	2.51	2.68
HSC 1	–	0.18 ± 0.09	2.15 ± 1.03	1.70 ± 0.42
DES 5	–	0.02	0.20	3.46
BLISS 1	12.0[q]	0.10 ± 0.07	1.18 ± 0.78	2.10 ± 0.58
Gaia 3	1.3[r]	0.66 ± 0.00	7.95 ± 0.00	2.64
DELVE 1	$12.5^{+1.0}_{-0.7}$[s]	0.16 ± 0.08	1.88 ± 0.91	1.82 ± 0.42
DELVE 2	> 13.3[t]	2.11 ± 0.72	25.33 ± 8.61	0.81 ± 0.30
YMCA-1	9.6[w]	0.09 ± 0.03	1.06 ± 0.36	2.49 ± 0.29
DELVE 5	10.0[x]	0.12 ± 0.05	1.44 ± 0.63	1.68 ± 0.38
DELVE 3	> 11.7[x]	0.32 ± 0.15	3.80 ± 1.85	1.92 ± 0.42
DELVE 4	13.5[x]	0.14 ± 0.06	1.68 ± 0.74	1.92 ± 0.38
DELVE 6	> 9.0[y]	0.58 ± 0.37	6.90 ± 4.43	1.54 ± 0.56

[a] Paust et al. (2014), [b] Fadely et al. (2011), [c] Ortolani et al. (2013), [d] Muñoz et al. (2012), [e] Balbinot et al. (2013), [f] Kim & Jerjen (2015), [g] Kim et al. (2015b), [h] Laevens et al. (2015), [i] Weisz et al. (2016), [j] Martin et al. (2016c), [k] Kim et al. (2016), [l] Luque et al. (2017), [m] Conn et al. (2018), [n] Luque et al. (2018), [o] Jerjen et al. (2018b), [p] Longeard et al. (2019), [q] Mau et al. (2019), [r] Torrealba et al. (2019), [s] Mau et al. (2020), [t] Cerny et al. (2021), [w] Piatti & Lucchini (2022), [x] Cerny et al. (2023a), [y] Cerny et al. (2023b),

detail in the next section, where I also consider another driver of mass loss – tidal effects.

8.7.3 Dynamical and Environmental Impacts on MF Slope

The evaporation timescale analysis presented here considers only internal dynamical processes, as defined by Equation 8.2. However, it is important to recognize that most systems in Region E are located at relatively small Galactocentric distances ($R_{GC} \sim 15\tilde{}30$ kpc), with four – Kim 3, Segue 3, DELVE 1, and Kim 1 – residing within 20 kpc. This proximity to the Galactic center likely enhances the role of external tidal forces. As illustrated in Fig. 8.12, these systems with the shortest present-day relaxation timescales are also those closest to the Galactic center. This spatial correlation suggests that tidal interactions may further accelerate mass loss in these systems.

Lamers et al. (2010) identified three distinct phases of mass loss in star clusters: (A) an early phase dominated by stellar evolution, (B) a phase where mass loss is primarily driven by dynamical effects ("dissolution"), and (C) a late phase following core collapse. The first phase is the strongest and dominates at early times, but the later phases become increasingly important for long-term structural evolution.

Building on this, Madrid et al. (2017) demonstrated that when both stellar evolution and the effects of the Galactic tidal field are included in globular cluster models, the dimensionless mass evaporation rate[17] is significantly higher than previously estimated, and shows a strong dependence on galactocentric distance. Their results are particularly pronounced in regions experiencing a strong tidal field, i.e., at $R_{\rm GC} \sim 4$ kpc. These findings are also in line with recent results from Chen et al. (2025), who, by matching mock tidal streams to observations, concluded that theoretical two-body evaporation alone underestimates total mass loss in a tidal field by a factor of $\lesssim 2$. (While their analysis adopted a ratio of $t_{\rm ev}/t_{\rm rh} = 20$, in this thesis I assume $t_{\rm ev}/t_{\rm rh} = 12$, which translates to $\lesssim 3.5$ under the adopted definition.)

Bringing together the effects of the tidal field, relaxation timescales, and mass segregation, an anticorrelation between MF slope and R_{GC} is expected for GCs. This trend has also been proposed by Contenta et al. (2017) as a distinguishing characteristic between GCs and DGs. Specifically, they suggested examining MF slope

[17]Note that in their work, the mass evaporation rate encompasses not only stellar evaporation due to two-body interactions, but also includes all relevant mass-loss processes such as tidal stripping, stellar evolution, relaxation-driven escape etc.

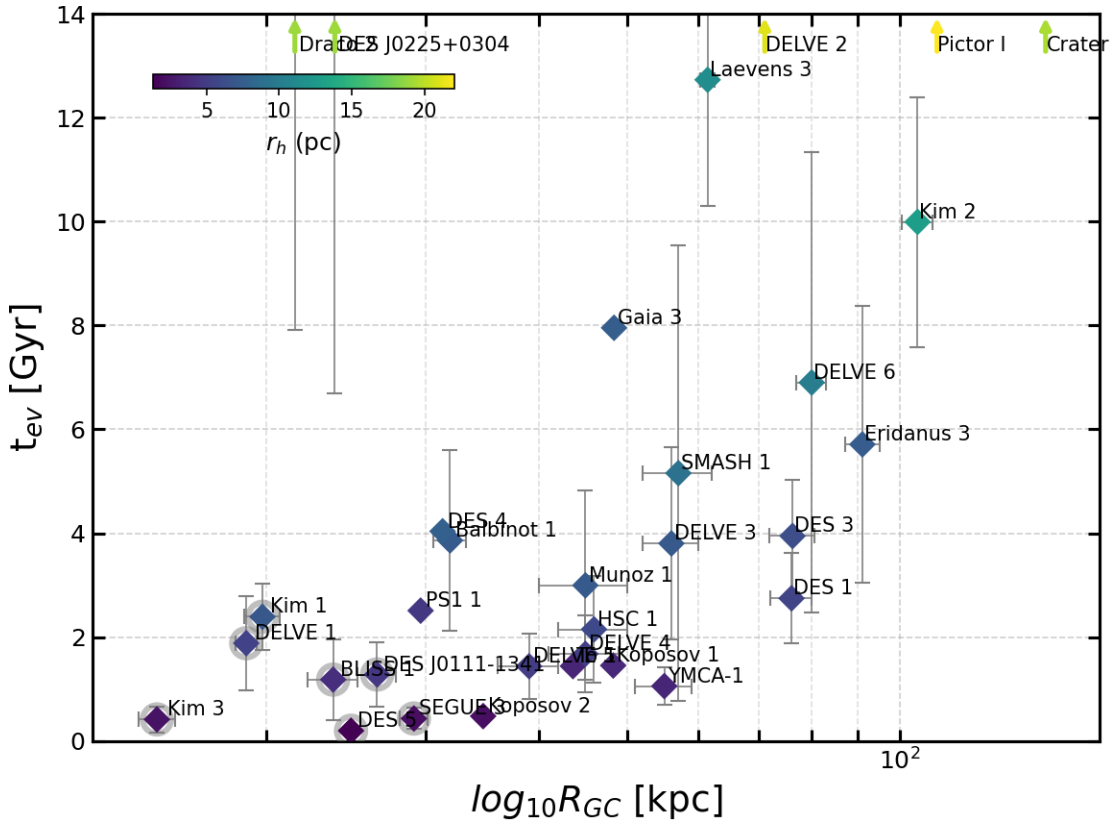

Figure 8.12: Evaporation timescales (see Table 8.2) as a function of galactocentric distance for known faint ambigous systems. Marker colors indicate half-light radius, r_h. Systems in Region E (see Fig. 8.1), circled in grey, are among the most compact, lie closest to the Galactic center, and exhibit the shortest evaporation times based on their present structural parameters.

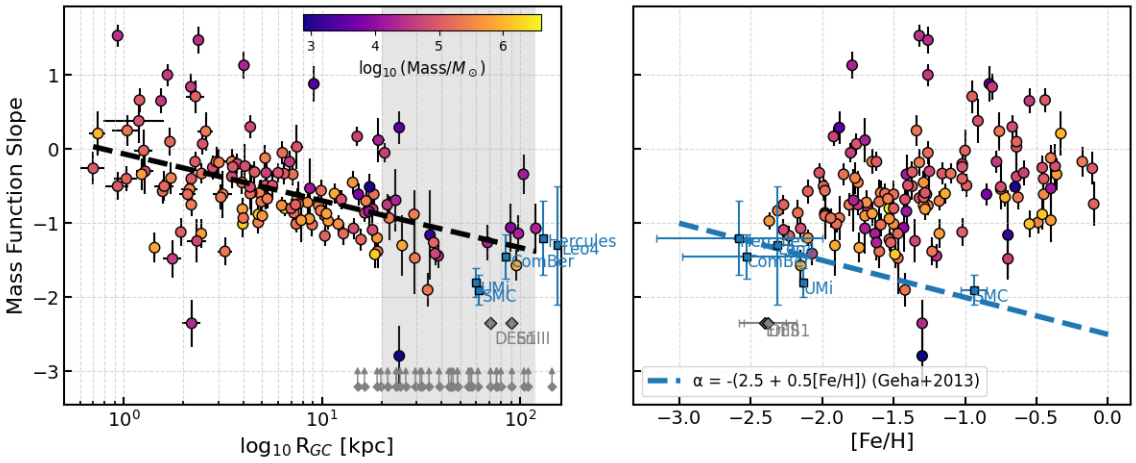

Figure 8.13: Mass function slope (α) of Milky Way GCs as a function of Galactocentric distance R_{GC} (left) and metallicity [Fe/H] (right), using data from the Hilker et al. (2020) and Harris (2010) catalogs. The black dashed line in the left panel shows a linear fit. Data points are color-coded by cluster mass, showing that low-mass clusters are absent at $R_{\rm GC} < 10$ kpc, though no clear overall trend between M and $R_{\rm GC}$ is evident. The Galactocentric distance range of faint ambiguous systems (marked as grey diamonds with upward arrows) is highlighted to emphasize that the anticorrelation trend in this region ($R_{\rm GC} \gtrsim 20$ kpc) becomes less clear, likely due to small-number statistics or reduced tidal influence shaping the relation. For comparison, DGs with measured MF slopes are also shown (Geha et al., 2013; Gennaro et al., 2018); their slopes are similar to those of GCs at comparable distances but are expected to be largely independent of $R_{\rm GC}$ and instead driven by internal environmental factors. This is illustrated in the right panel, which includes a linear fit to the MF slope–metallicity relation for DGs as derived by Geha et al. (2013), while no significant trend is observed for GCs. DES1 and Eri3 – both reported to be well fit by a Salpeter MF (Conn et al., 2018) – are also included in both panels.

simultaneously as a function of both R_{GC} and metallicity. While DGs may exhibit similarly steep MF slopes, these are found to depend on intrinsic properties such as total mass and metallicity (e.g., Geha et al., 2013), and are expected to remain largely independent of Galactocentric distance.

In Fig. 8.13, I present the MF slope (α) as a function of $R_{\rm GC}$ and [Fe/H]. An anticorrelation between the MF slope and Galactocentric distance is indeed observed for MW GCs. Notably, the scatter in this relation increases toward smaller Galactocentric distances ($R_{\rm GC} \lesssim 3$ kpc), and – more relevant for the distance regime of the currently observed faint ambiguous systems (highlighted in grey) – the correlation becomes less well-constrained beyond $R_{\rm GC} > 20$ kpc. This breakdown may stem purely

from small-number statistics at large distances, or it may reflect a genuine physical effect – specifically, the reduced tidal influence at larger R_{GC}. The latter is particularly supported by the analysis of Madrid et al. (2017), who showed that the mass evaporation rate of GCs increases rapidly at $R_{\rm GC} < 10$ kpc. This also aligns with my observations in Fig. 8.13, which shows an absence of low-mass star clusters below this distance threshold. Notably, there is an outlier at $R_{GC} = 2.2$ with $\alpha = -2.35$. This cluster also exhibits the highest $M/L_V = 8.5$, possibly explaining its steep MF at such close proximity to the Galactic center.

Conversely, DGs exhibit a trend between MF slope and metallicity, possibly driven by environmentally dependent IMF variations (Geha et al., 2013) and shown in the right panel of Fig. 8.13. In contrast, GCs show no dependence of the MF slope on either mass or metallicity. While deeper photometric constraints on MF slopes in both faint ambiguous systems and DGs are still needed, this distinction may provide a promising diagnostic for probing the nature of ambiguous systems – particularly those located at small Galactocentric distances.

8.7.4 System Survivability and N-body Modelling

One more valuable tool for distinguishing dark matter–free star clusters from dark matter–dominated galaxies is N-body modeling, i.e., a test of whether a system could evolve into its observed properties under specific assumptions. While computationally expensive, this method may offer a promising way to break the deadlock regarding the true nature of such systems.

A compelling example is Ursa MajorIII/UNIONS 1 (UMa3/U1), the faintest and smallest system in this region, discovered by Smith et al. (2024) and located at ~ 10 kpc from the Galactic center. N-body modeling by Errani et al. (2024b) showed that if UMa3/U1 were a star cluster, its low density would cause it to disintegrate rapidly – within 0.4 to 0.8 Gyr – due to tidal interactions with the Milky Way's gravitational potential. This conclusion is also supported by the system's higher-than-expected velocity dispersion for a dark matter–free cluster. However, Devlin et al. (2025) demonstrated that when stellar evolution is included, compact stellar remnants sinking to the cluster's center through mass segregation can extend its lifetime to 1.9–2.7 Gyr. Moreover, the presence of primordial binaries can account for the elevated velocity dispersion, providing an alternative explanation for the observed kinematics.

Devlin et al. (2025)'s result also emphasizes the role of white dwarfs (WD) in deepening the gravitational potential wells of compact systems. While initially dense clusters are not expected to retain BHs (unlike their more extended counterparts, see Sec. 8.4.2) —as most/all are rapidly ejected via two-body interactions (Contenta et al., 2017; Gieles et al., 2021; Weatherford et al., 2023) (the exception is dark star clusters, will be discussed below) — they can still accumulate WDs in their cores. This enhances the central density and contributes to the overall dynamical stability of the system. The inclusion of dark remnants such as WDs implies that the true central densities of some systems may be significantly higher than the values listed in Table 8.2. For example, in the case of UMa III/U1, Devlin et al. (2025) estimate an order-of-magnitude increase in density when WDs are included. This would directly affect relaxation/evaporation timescales, as these depend on the total cluster mass M and assumed mass profile (see Equation 8.2).

This highlights how N-body modeling can offer crucial insights into the evolution of low-mass systems – insights that observations alone cannot offer. While such detailed modeling has so far been applied only to UMa III/U1, these results may extend to other compact clusters/dwarfs. Ultimately, such scenarios must be tested observationally, and tidal debris offers a promising means of doing so.

Exploring wider streams in collisional N-body disruption models

A robust N-body prediction that can be tested observationally is the presence and kinematic structure of tidal debris around ambiguous systems. Contenta et al. (2017) suggested that, in the case of dissolving star clusters, these should be kinematically cold (a few 100 m s^{-1}). If, however, these systems have always been dense, they are not expected to form observable tidal tails (Gieles et al., 2021). Errani et al. (2024b), assuming an extremely low intrinsic velocity dispersion for the progenitor, predicted that UMiIII/U1's debris would form a thin stream along its orbit. However, as mentioned earlier, these predictions rely on collisionless N-body models, which may be unreliable for compact systems, as discussed by Devlin et al. (2025)

Improved collisional N-body simulations that incorporate stellar interactions and evolution (Spurzem & Kamlah, 2023) are essential for accurately modeling tidal debris. Equally important is observational insight into stream formation rates and mechanisms. Chen et al. (2025) reproduced observed stream morphologies and found that stream formation efficiency correlates with cluster mass and orbital frequency, but not

with r_h. These results help constrain stream densities across a range of progenitor properties and orbital histories. Finally, detailed studies of stellar escape processes –beyond two-body relaxation and tidal stripping – are needed, as high-velocity escapers can reshape cluster properties without contributing to streams (e.g., Weatherford et al., 2023).

Improved modeling, followed by targeted observational searches for extended tidal debris around promising candidates using deep Rubin/LSST data (i.e., astrometry and photometry below the *Gaia* limit as described further by Bonaca & Price-Whelan 2025) could provide valuable diagnostics for distinguishing between star cluster and microgalaxy scenarios in the future.

8.8 $M_V - r_h$ tracks

To demonstrate more clearly DGs and GCs can become mixed on the size–luminosity plane, I present several scenarios in Fig. 8.14. In this context, an *environmental origin* refers to the role of external tidal forces in shaping a system's properties, while an *intrinsic origin* implies that internal dynamical processes are the primary drivers of evolution. The corresponding evolutionary pathways in the M_V–r_h plane are also indicated in the figure.

Pathway 1 is a dark matter dominated scenario ("microgalaxy") includes two distinct progenitors: a UFD that undergoes monotonic size expansion followed by a sharp turn (see Fig. 7 in Errani & Peñarrubia 2020), and a classical dSph galaxy (see Fig. 7 in Errani et al. 2024a).

Pathway 2 represents systems discussed in Secs. 8.6.1 and 8.7.1, such as clusters accreted with their host galaxies or those formed during infall. In this scenario, the arrow in the lower panel of Fig. 8.14 may shift diagonally to the right, illustrating an increase in r_h due to expansion in a relatively weak tidal field – insufficient to cause significant stripping.

The *intrinsic origin* category includes two sub-scenarios applicable to both DM-free and DM-dominated systems. The first sub-scenario involves systems that formed compact: either as galaxies hosted by the smallest DM halos (Pathway 3) or as primordial clusters (Pathway 5). While the classical ΛCDM model predicts a critical halo mass of $\sim 10^8\,M_\odot$ at redshift $z = 10$ (or $\sim 10^{9.7}\,M_\odot$ at $z = 0$) below which star formation is suppressed due to the 'hydrogen-cooling' limit (see, e.g., Santos-Santos et al. 2022; Pereira-Wilson et al. 2022), a recent surge in semi-analytical and

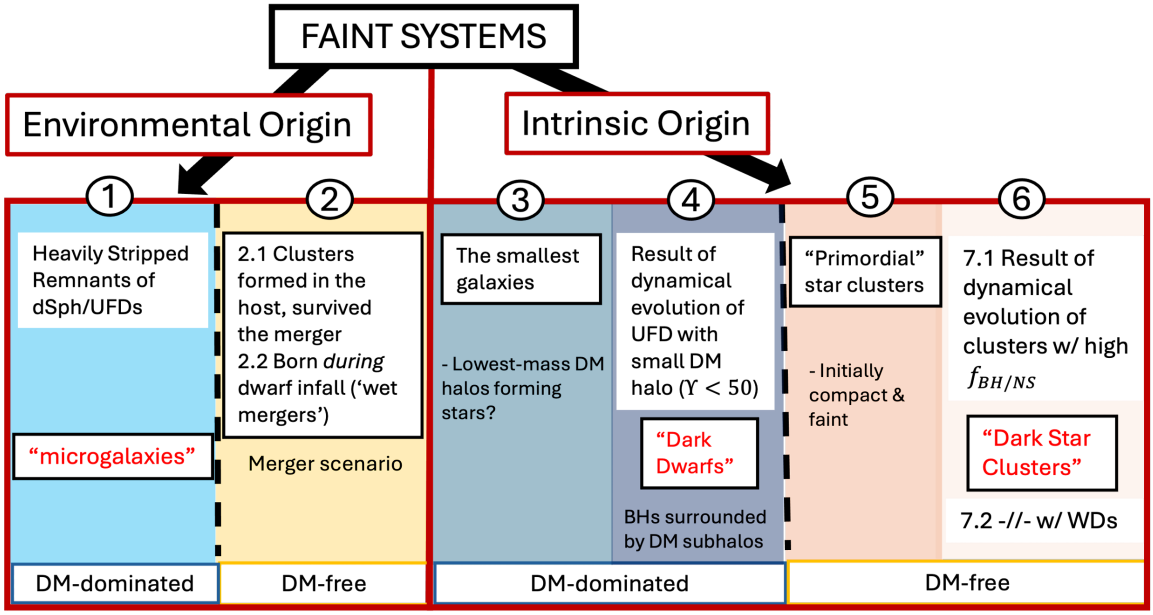

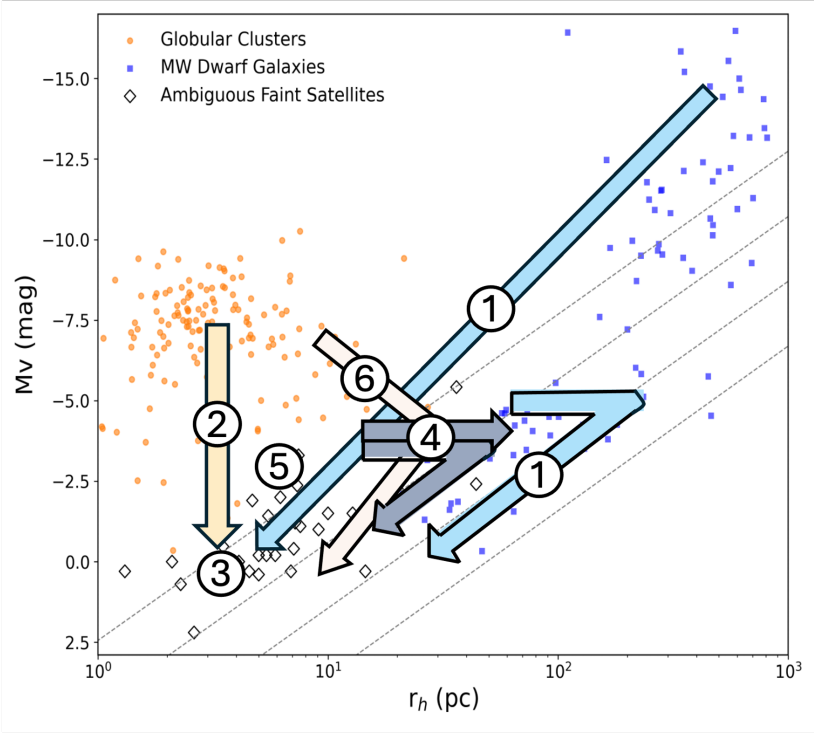

Figure 8.14: A schematic demonstration of how star clusters and dwarf galaxies can change on the M_V–r_h plane for various scenarios described above.

regulatory models tailored to UFDs is now examining in greater detail the shape, flattening, and scatter of the stellar mass–halo mass relation in this regime (Kravtsov & Manwadkar, 2022; Chen et al., 2022; O'Leary et al., 2023; Ahvazi et al., 2024). Some of these models even predict galaxy formation at the faintest end of the "Valley of Ambiguity" (Manwadkar & Kravtsov, 2022). Although these formation channels are not yet extensively explored, they can offer valuable insight into DM properties (e.g., cooling thresholds in DM halos; Nadler 2025) and may leave distinct chemical signatures, particularly in the case of primordial clusters (see Sec. 8.5.1).

The second intrinsic pathway involves internal dynamical evolution that produces an extremely faint, yet still gravitationally bound system. As discussed in Sec. 8.5.2, systems embedded in low-mass dark matter halos can undergo mass segregation. Errani et al. (2025) demonstrated that this process can lead to the central accumulation of massive binaries, ultimately facilitating the formation of massive BHs. When combined with the tidal stripping of low-mass stars, such evolution may result in compact remnants dominated by BHs and embedded in low-mass dark matter halos—*"dark dwarfs"* (Pathway 4).

Fig. 8.14 illustrates two corresponding evolutionary tracks: the first corresponds to evolution in a weak tidal field, where the stellar population expands adiabatically without significant mass loss.[18]. The second track represents evolution under stronger tidal influence, resembling the UFD-origin "microgalaxy" scenario, with more substantial stripping and compactification.

Interestingly, a similar dynamical pathway can lead to the formation of *dark star clusters* (DSCs)[19]. It has been shown that a significant population of BHs and neutron stars (NSs) can be retained in old clusters (e.g., Maccarone et al., 2007; Moody & Sigurdsson, 2008; Strader et al., 2012; Chomiuk et al., 2013; Wu et al., 2025). Through runaway mass segregation, these remnants concentrate in the cluster core, forming a dense "dark core" (Banerjee & Kroupa, 2011), while lower-mass stars gain energy via dynamical encounters and escape. This yields a system whose gravitational potential

[18]In the *absence* of tidal forces, internal dynamics lead massive stars to migrate inward (reducing r_h), while lower-mass stars migrate outward (increasing r_h). Depending on which component dominates the observed light, this can produce divergent apparent trajectories in the M_V–r_h plane – this case, therefore, is not shown.

[19]While traditional definitions of DSCs focus on systems with central concentrations of BHs and NSs, in table presented in Fig. 8.14 I extend this pathway to include clusters with centrally accumulated WDs, as discussed in Sec. 8.7.4. Although WDs may have a less pronounced, more long-scaled impact on internal dynamics, both cases involve the mass segregation-driven buildup of dark stellar remnants in dark-matter-free clusters.

is dominated by massive dark remnants – i.e., a DSC. As discussed in Sec. 8.4.2, such clusters with high BH retention may undergo expansion, reaching sizes and structures resembling dwarf galaxies. This corresponds to the 'first part' of the DSC arrow pathway (Pathway 6) in Fig. 8.14, before the curve turning point. This early expansion is relatively rapid, while the subsequent evolution and its timescale depend on multiple factors: the competition between stellar tidal stripping and the self-depletion of the dark core, the presence or absence of primordial mass segregation and primordial binaries, the strength of natal kicks, and other cluster-internal properties. Recent studies suggest that variations in these parameters can significantly accelerate DSC formation, even in the weak tidal environments of the Milky Way's outer halo (Ghasemi et al., 2024; Wu et al., 2024). These systems show high velocity dispersions, suppressed mass segregation, and mass-to-light ratios up to $\Upsilon \approx 10$, akin to the "dark dwarfs" described above (Wu et al., 2024).

Both dark-matter-dominated and remnant-dominated (DM-free) systems thus harbour substantial hidden mass and exhibit similar observable properties, making it challenging to distinguish between baryonic and non-baryonic dark components[20].

8.9 Summary

I have demonstrated that several of the faintest satellite systems exhibit similarities in their physical properties, which allow them to be grouped into distinct regions on the M_V vs. r_h plane. Each of these regions of satellites comes with its own observational and measurement-related limitations that must be carefully considered when assessing their nature.

For regions with extended systems, such as Region B and possibly Region C, it is important to account for the impact of black holes on the structural and dynamical evolution of clusters, especially when coupled with the influence of binary stars (Contenta et al., 2017; Wang, 2020; Wang et al., 2024; Dickson et al., 2024). These factors can cause globular clusters (GCs) to occupy the same region of the size-luminosity plane as UFDs and produce a close resemblance between the two in various dynamical properties – such as elevated velocity dispersions and the absence of detectable mass

[20]Potential diagnostics include the stellar mass function and galactocentric distance: in dark dwarfs, low-mass stars are more likely to survive at large galactocentric distances due to weaker tidal forces, whereas in DSCs, internal dynamical interactions with massive remnants may efficiently eject low-mass stars – even in relatively weak tidal environments. Further insight from N-body modeling is needed to disentangle these scenarios.

segregation (e.g., Peuten et al., 2016).

For more compact systems, such as those in Region D and Region E, dark-matter-free scenarios should be explored with caution. I have shown that several systems are likely (ex-situ) star clusters which have undergone various evolutionary and tidal effects. Special attention must be given to accumulation of dark stellar remnants in their cores (e.g., Wu et al., 2024; Devlin et al., 2025). Their photometrically derived properties are also highly sensitive to stellar population selection criteria and photometric depth and precision (Ortolani et al., 2013; Paust et al., 2014). Several dark-matter-free scenarios remain to be tested, including: formation from merger events between dwarf galaxies and the Milky Way, origin in tidal tails of disrupted systems, and survival as 'dark cluster' remnants from Region B. Simultaneously, dark-matter-dominated formation scenarios must also be considered, including the "initially compact galaxy" – which could push the known limit for the smallest dark matter halo able to form stars – and the "heavily stripped galaxy", which involves the study of classical dSph/UFD progenitors and their properties (Errani et al., 2024a). These possibilities are essential for refining our understanding of the properties of dark matter particles.

Several key diagnostics will be essential in advancing this field:

- Velocity dispersion measurements with improved constraints on binary fractions to clarify dark matter content in UFDs;
- Detailed chemical abundance patterns (carefully assessing how metallicity, n-capture element ratios, and C-enhancement differ between UFDs and possible primordial GCs);
- The slope of the stellar mass function as a function of Galactocentric distance – independent of system mass/metallicity – with consideration of steepening effects due to unresolved binaries and black hole populations;
- Assessment of tidal resilience (accounting for the influence of dark remnants and binaries, and requiring well-constrained orbital solutions);
- Investigating extragalactic origins through chemo-dynamical analysis;
- Presence/absence of cold stellar streams (via collisional N-body models and targeted searches);

Future high-quality spectroscopic observations will be critical for measuring binary fractions and chemical abundances, especially in the era of extremely large telescopes. Space-based direct imaging may also help identify and constrain binary populations through direct detections. Deeper photometric and astrometric data (e.g., LSST/Rubin, below the Gaia limit) will be essential for recovering mass function slopes and identifying signs of mass segregation. Ultimately, continued progress in detailed (e.g., collisional) N-body modeling will be necessary to uncover the true nature of the faintest ambiguous systems.

Chapter 9

Conclusions

The analysis of five stars observed in two low surface brightness Milky Way satellites, Sagittarius II (Sgr2) and Aquarius II (Aqu2) is presented based on spectra taken during the commissioning of the Gemini/GHOST spectrograph. The spectra were taken in both the single and double IFU standard modes, binning 2x8 for the highest possible signal on these faint objects (G$<$ 18.8). The spectra are exquisite in their resolution and high throughput over a wide wavelength range.

From GHOST spectra of two stars in Aqu2 and data in the literature, we find: (i) radial velocity and metallicity dispersions consistent with membership in a dark matter-dominated UFD galaxy; (ii) chemical abundances that indicate inefficient star formation, i.e., low abundances of [Na/Fe], [Sr/Fe], and [Ba/Fe]; (iii) [K/Fe] enrichment, most likely due to the impact of super AGB stars in a low-mass and unevolved UFD galaxy.

From GHOST spectra of three stars in Sgr2 and data in the literature, we find: (i) radial velocity and metallicity dispersions that are just barely resolved, and inconclusive on the nature of the system, especially if there are binary stars; (ii) chemical abundances that are exceptional in only one element (Eu), and in only one star, Sgr2584, where [Eu/Fe]$= +0.7 \pm 0.2$, typical of the r-I stars which are found in both globular clusters (e.g., M15, M92) and UFDs (e.g., Tuc III). From these results, Sgr2 remains a challenge to classify, highlighting the difficulty in classifying some of the lowest mass and faintest MW satellites, even with detailed chemical abundances. We suggest this is also true for Tuc III. We discuss the value of additional diagnostics in classifying the most ambiguous systems, such as mass segregation in exploring the origins and total mass (dark matter content) of star clusters and potentially UFDs (Baumgardt et al., 2022). For Sgr2, we support their conclusion that Sgr2 is most

likely a globular cluster with a radial velocity dispersion that is slightly inflated by binary stars.

The spectra used in this analysis demonstrate the high quality available with the new `Gemini/GHOST` spectrograph. It also served as a pilot program for the launch of the Gemini High-resolution Optical-UV Legacy Survey (GHOULS), where all bright ($G < 18.5$) stars within $R < 3\ R_h$ without published high resolution spectra in all ultra faint MW satellites are currently queued for ongoing studies on the nature of these systems.

My analysis of the "Valley of Ambiguity" highlights the need to apply multiple discriminators simultaneously when assessing ambiguous systems. Depending on their location in the size–luminosity (r_h–M_V) plane, such systems may follow distinct evolutionary paths and be subject to different observational biases. The significant overlap between star clusters and dwarf galaxies across various regions of this plane underscores the limitations of relying solely on structural properties or velocity and metallicity dispersions.

Additional diagnostics may include detailed chemical abundances; the slope of the mass function and its sensitivity to the Galactocentric distance and metallicity; evidence of mass segregation; tidal stability analysis through combined theoretical estimates of density and tidal radii with observed tidal features; chemo-dynamical links to known merger events; detection of cold tidal streams; and N-body modeling to reproduce current observations under varying assumptions. For many of these, binary fractions and central black hole populations play a particularly important role in shaping internal kinematics and structural evolution. Upcoming high-resolution spectroscopic and deep photometric surveys will be essential for refining these diagnostics and better constraining the nature of these faint systems.

Appendix A

Additional Information

A.1 GHOST Observations

The GHOST exposures used from commissioning for the spectra analysed in this paper are provided in Table A.1. This includes target information per IFU using both the single and dual observing modes, as well as exposure times, number of exposures coadded, and the SNR of the coadded exposures at various wavelengths. We also include the calibration files used, which is important to note as the commissioning data includes many of these files as we began testing the spectrograph. The slitview file was particularly important for proper use of the commissioning version of the GHOST data reduction pipeline.

Table A.1: GHOST exposures for Sgr2 and Aqu2 targets, including the calibration files used for the data reduction pipeline.

Target	Science	IFU	Arm	t_{exp} (s)	N_{exp}	SNR @λ (Å)	Calibration Files	Type	t_{exp} (s)
Aqu2776	aqu2_sr_2x4_br	1	Blue	1800	x3	4 @4130	arcs_sr_1x1_brs300_20220629	arc	300
	1800s300_20220629		Red	1800	x3	26 @6050	flat_sr_1x1_br6_s02_20220629	flat	6
Aqu2472		2				4 @4130	bias_2x4_20220629	2x4 bias	
						28 @6050	bias_1x1_20220629	1x1 bias	
							HD122196_HIP068460_sr1x1_br300s3	slitview	0.1
Sgr2584	Sag2_sr_2x4_b3600_	1	Blue	3600	x1	8 @4130	arc_hr_1x1_thxe2_20220628	arc	300
	r1200_s300_20220628		Red	1200	x3	59 @6050	flats_hr_1x1_20220628	flat	6
							bias_2x4_20220628	2x4 bias	
							bias_1x1_20220628	1x1 bias	
							HD122196_HIP068460_sr1x1_br300s3	slitview	1
Sgr2656	Sag2_set2_sr_br	1	Blue	3600	x3	5 @4130	arcs_sr_1x1_brs300_20220629	arc	300
	3600s150_20220630		Red	3600	x3	24 @6050	flat_1x1_sr_br6s02_set2_20220630	flat	6
Sgr2936		2				7 @4130	bias_2x4_20220630	2x4 bias	
						69 @6050	bias_1x1_20220630	1x1 bias	
							HD122196_HIP068460_sr1x1_br300s3	slitview	0.1

Bibliography

Abazajian, K. N., Adelman-McCarthy, J. K., Agüeros, M. A., et al. 2009, *ApJS*, 182, 543, DOI: 10.1088/0067-0049/182/2/543

Abbott, T. M. C., Abdalla, F. B., Allam, S., et al. 2018, *ApJS*, 239, 18, DOI: 10.3847/1538-4365/aae9f0

Adén, D., Eriksson, K., Feltzing, S., et al. 2011, *A&A*, 525, A153, DOI: 10.1051/0004-6361/201014963

Ahvazi, N., Benson, A., Sales, L. V., et al. 2024, Monthly Notices of the Royal Astronomical Society, 529, 3387, DOI: 10.1093/mnras/stae761

Allison, R. J., Goodwin, S. P., Parker, R. J., et al. 2009, Monthly Notices of the Royal Astronomical Society, 395, 1449, DOI: 10.1111/j.1365-2966.2009.14508.x

Andrae, R., Fouesneau, M., Creevey, O., et al. 2018, *A&A*, 616, A8, DOI: 10.1051/0004-6361/201732516

Aoki, W., Beers, T. C., Lee, Y. S., et al. 2013, *AJ*, 145, 13, DOI: 10.1088/0004-6256/145/1/13

Aros, F. I., Sippel, A. C., Mastrobuono-Battisti, A., et al. 2021a, Monthly Notices of the Royal Astronomical Society, 508, 4385–4398, DOI: 10.1093/mnras/stab2872

—. 2021b, Monthly Notices of the Royal Astronomical Society, 508, 4385, DOI: 10.1093/mnras/stab2872

Ashman, K. M., & Zepf, S. E. 1992, *ApJ*, 384, 50, DOI: 10.1086/170850

Asplund, M., Grevesse, N., Sauval, A. J., & Scott, P. 2009, *ARA&A*, 47, 481, DOI: 10.1146/annurev.astro.46.060407.145222

Balbinot, E., Santiago, B. X., da Costa, L., et al. 2013, *ApJ*, 767, 101, DOI: 10.1088/0004-637X/767/2/101

Banerjee, S., & Kroupa, P. 2011, The Astrophysical Journal Letters, 741, L12, DOI: 10.1088/2041-8205/741/1/L12

Bastian, N., & Lardo, C. 2018, *ARA&A*, 56, 83, DOI: 10.1146/annurev-astro-081817-051839

Baumgardt, H. 2017, Monthly Notices of the Royal Astronomical Society, 464, 2174, DOI: 10.1093/mnras/stw2488

Baumgardt, H., Faller, J., Meinhold, N., McGovern-Greco, C., & Hilker, M. 2022, *MNRAS*, 510, 3531, DOI: 10.1093/mnras/stab3629

Baumgardt, H., & Makino, J. 2003, *MNRAS*, 340, 227, DOI: 10.1046/j.1365-8711.2003.06286.x

Bechtol, K., Birrer, S., Cyr-Racine, F.-Y., et al. 2022, arXiv e-prints, arXiv:2203.07354, DOI: 10.48550/arXiv.2203.07354

Belokurov, V. 2013, New Astronomy Reviews, 57, 100, DOI: https://doi.org/10.1016/j.newar.2013.07.001

Belokurov, V., & Kravtsov, A. 2023, Monthly Notices of the Royal Astronomical Society, 528, 3198, DOI: 10.1093/mnras/stad3920

Belokurov, V., Zucker, D. B., Evans, N. W., et al. 2006, , 647, L111, DOI: 10.1086/507324

Belokurov, V., Walker, M. G., Evans, N. W., et al. 2009, *MNRAS*, 397, 1748, DOI: 10.1111/j.1365-2966.2009.15106.x

—. 2010, , 712, L103, DOI: 10.1088/2041-8205/712/1/L103

Berg, T. A. M., Ellison, S. L., Prochaska, J. X., Venn, K. A., & Dessauges-Zavadsky, M. 2015, *MNRAS*, 452, 4326, DOI: 10.1093/mnras/stv1577

Bica, E., Westera, P., Kerber, L. d. O., et al. 2020, *AJ*, 159, 82, DOI: 10.3847/1538-3881/ab6595

Boberg, O., Friel, E. D., & Vesperini, E. 2015, in American Astronomical Society Meeting Abstracts, Vol. 225, American Astronomical Society Meeting Abstracts #225, 247.20

Bonaca, A., & Price-Whelan, A. M. 2025, , 100, 101713, DOI: 10.1016/j.newar.2024.101713

Bonnell, I. A., & Davies, M. B. 1998, *MNRAS*, 295, 691, DOI: 10.1046/j.1365-8711.1998.01372.x

Bonnivard, V., Combet, C., Maurin, D., & Walker, M. G. 2015a, *MNRAS*, 446, 3002, DOI: 10.1093/mnras/stu2296

Bonnivard, V., Combet, C., Daniel, M., et al. 2015b, *MNRAS*, 453, 849, DOI: 10.1093/mnras/stv1601

Bruce, J., Li, T. S., Pace, A. B., et al. 2023, Astrophys. J., 950, 167, DOI: 10.3847/1538-4357/acc943

Buder, S., Lind, K., Ness, M. K., et al. 2021, Monthly Notices of the Royal Astronomical Society, 510, 2407, DOI: 10.1093/mnras/stab3504

Bullock, J. S., & Boylan-Kolchin, M. 2017, *ARA&A*, 55, 343, DOI: 10.1146/annurev-astro-091916-055313

Buttry, R., Pace, A. B., Koposov, S. E., et al. 2022, *MNRAS*, 514, 1706, DOI: 10.1093/mnras/stac1441

Cabrera Garcia, J., Sakari, C. M., Roederer, I. U., et al. 2024, *ApJ*, 967, 101, DOI: 10.3847/1538-4357/ad380b

Callingham, T. M., Cautun, M., Deason, A. J., et al. 2022, *MNRAS*, 513, 4107, DOI: 10.1093/mnras/stac1145

Carraro, G. 2009, The Astronomical Journal, 137, 3809, DOI: 10.1088/0004-6256/137/4/3809

Carraro, G., Zinn, R., & Moni Bidin, C. 2007, *A&A*, 466, 181, DOI: 10.1051/0004-6361:20066825

Carretta, E., Gratton, R. G., Bragaglia, A., et al. 2013, *ApJ*, 769, 40, DOI: 10.1088/0004-637X/769/1/40

Carretta, E., Bragaglia, A., Gratton, R., et al. 2009, Astronomy & Astrophysics, 505, 117

Cautun, M., Benítez-Llambay, A., Deason, A. J., et al. 2020, Monthly Notices of the Royal Astronomical Society, 494, 4291, DOI: 10.1093/mnras/staa1017

Cerny, W., Pace, A. B., Drlica-Wagner, A., et al. 2021, *ApJ*, 910, 18, DOI: 10.3847/1538-4357/abe1af

Cerny, W., Martínez-Vázquez, C. E., Drlica-Wagner, A., et al. 2023a, The Astrophysical Journal, 953, 1, DOI: 10.3847/1538-4357/acdd78

Cerny, W., Drlica-Wagner, A., Li, T. S., et al. 2023b, The Astrophysical Journal Letters, 953, L21, DOI: 10.3847/2041-8213/aced84

Cerny, W., Simon, J., Li, T., et al. 2023c, The Astrophysical Journal, 942, 111, DOI: 10.3847/1538-4357/aca1c3

Chambers, K. C., Magnier, E. A., Metcalfe, N., et al. 2016, The Pan-STARRS1 Surveys. https://arxiv.org/abs/1612.05560

Chen, L.-H., Magg, M., Hartwig, T., et al. 2022, Monthly Notices of the Royal Astronomical Society, 513, 934, DOI: 10.1093/mnras/stac933

Chen, Y., Li, H., & Gnedin, O. Y. 2025, The Astrophysical Journal Letters, 980, L18, DOI: 10.3847/2041-8213/adaf93

Chiti, A., Frebel, A., Ji, A. P., et al. 2018, *ApJ*, 857, 74, DOI: 10.3847/1538-4357/aab4fc

Chiti, A., Frebel, A., Ji, A. P., et al. 2023, The Astronomical Journal, 165, 55, DOI: 10.3847/1538-3881/aca416

Chomiuk, L., Strader, J., Maccarone, T. J., et al. 2013, The Astrophysical Journal, 777, 69, DOI: 10.1088/0004-637X/777/1/69

Cohen, J. G., Huang, W., & Kirby, E. N. 2011, *ApJ*, 740, 60, DOI: 10.1088/0004-637X/740/2/60

Cohen, J. G., & Kirby, E. N. 2012, *ApJ*, 760, 86, DOI: 10.1088/0004-637X/760/1/86

Collet, R., Nordlund, Å., Asplund, M., Hayek, W., & Trampedach, R. 2018, *MNRAS*, 475, 3369, DOI: 10.1093/mnras/sty002

Collins, M. L. M., Tollerud, E. J., Sand, D. J., et al. 2017, Monthly Notices of the Royal Astronomical Society, 467, 573, DOI: 10.1093/mnras/stx067

Conn, B. C., Jerjen, H., Kim, D., & Schirmer, M. 2018, *ApJ*, 852, 68, DOI: 10.3847/1538-4357/aa9eda

Conroy, C., Naidu, R. P., Zaritsky, D., et al. 2019, The Astrophysical Journal, 887, 237, DOI: 10.3847/1538-4357/ab5710

Contenta, F., Gieles, M., Balbinot, E., & Collins, M. L. M. 2017, *MNRAS*, 466, 1741, DOI: 10.1093/mnras/stw3178

Correa, R. A. C., Moraes, P. H. R. S., Dutra, A. d. S., et al. 2021, , 103, 103519, DOI: 10.1103/PhysRevD.103.103519

Dalal, N., & Kravtsov, A. 2022, , 106, 063517, DOI: 10.1103/PhysRevD.106.063517

Dalessandro, E., Lardo, C., Cadelano, M., et al. 2018, *A&A*, 618, A131, DOI: 10.1051/0004-6361/201833650

de Bennassuti, M., Salvadori, S., Schneider, R., Valiante, R., & Omukai, K. 2017, *MNRAS*, 465, 926, DOI: 10.1093/mnras/stw2687

de Jong, J. T. A., Yanny, B., Rix, H.-W., et al. 2010, The Astrophysical Journal, 714, 663, DOI: 10.1088/0004-637X/714/1/663

de los Reyes, M. A. C., Kirby, E. N., Ji, A. P., & Nuñez, E. H. 2022, *ApJ*, 925, 66, DOI: 10.3847/1538-4357/ac332b

Deason, A. J., & Belokurov, V. 2024, New Astronomy Reviews, 99, 101706, DOI: 10.1016/j.newar.2024.101706

Deason, A. J., Belokurov, V., & Weisz, D. R. 2015, *MNRAS*, 448, L77, DOI: 10.1093/mnrasl/slv001

Deason, A. J., Erkal, D., Belokurov, V., et al. 2020, Monthly Notices of the Royal Astronomical Society, 501, 5964–5972, DOI: 10.1093/mnras/staa3984

Del Popolo, A., & Le Delliou, M. 2021, Galaxies, 9, DOI: 10.3390/galaxies9040123

Dermigny, J. R., & Iliadis, C. 2017, The Astrophysical Journal, 848, 14, DOI: 10.3847/1538-4357/aa8ad0

Devlin, S., Baumgardt, H., & Sweet, S. M. 2025, Monthly Notices of the Royal Astronomical Society, 539, 2485, DOI: 10.1093/mnras/staf572

Dias, W. S., Monteiro, H., Moitinho, A., et al. 2021, VizieR Online Data Catalog: Updated parameters of 1743 open clusters (Dias+, 2021), VizieR On-line Data Catalog: J/MNRAS/504/356. Originally published in: 2021MNRAS.504..356D

Dickson, N., Smith, P. J., Hénault-Brunet, V., Gieles, M., & Baumgardt, H. 2024, *MNRAS*, 529, 331, DOI: 10.1093/mnras/stae470

Domínguez, R., Fellhauer, M., Blaña, M., et al. 2016, *MNRAS*, 461, 3630, DOI: 10.1093/mnras/stw1559

Drlica-Wagner, A., Carlin, J. L., Nidever, D. L., et al. 2021, *ApJS*, 256, 2, DOI: 10.3847/1538-4365/ac079d

Ebinger, K., Curtis, S., Ghosh, S., et al. 2020, *ApJ*, 888, 91, DOI: 10.3847/1538-4357/ab5dcb

Errani, R., Ibata, R., Navarro, J. F., Peñarrubia, J., & Walker, M. G. 2024a, *ApJ*, 968, 89, DOI: 10.3847/1538-4357/ad402d

Errani, R., Navarro, J. F., Smith, S. E. T., & McConnachie, A. W. 2024b, *ApJ*, 965, 20, DOI: 10.3847/1538-4357/ad2267

Errani, R., & Peñarrubia, J. 2020, Monthly Notices of the Royal Astronomical Society, 491, 4591, DOI: 10.1093/mnras/stz3349

Errani, R., Peñarrubia, J., & Walker, M. G. 2018, *MNRAS*, 481, 5073, DOI: 10.1093/mnras/sty2505

Errani, R., Peñarrubia, J., & Walker, M. G. 2025, Stellar Mass Segregation in Dark Matter Halos. https://arxiv.org/abs/2505.22717

Errani, R., Navarro, J. F., Ibata, R., et al. 2022, arXiv e-prints, arXiv:2203.02513. https://arxiv.org/abs/2203.02513

Evans, D. W., Riello, M., De Angeli, F., et al. 2018, *A&A*, 616, A4, DOI: 10.1051/0004-6361/201832756

Fadely, R., Willman, B., Geha, M., et al. 2011, The Astronomical Journal, 142, 88, DOI: 10.1088/0004-6256/142/3/88

Feltzing, S., Eriksson, K., Kleyna, J., & Wilkinson, M. I. 2009, *A&A*, 508, L1, DOI: 10.1051/0004-6361/200912833

Foote, H. R., Besla, G., Garavito-Camargo, N., et al. 2025, The Astrophysical Journal, 979, 171, DOI: 10.3847/1538-4357/ad9b89

Forbes, D. A. 2020, *MNRAS*, 493, 847, DOI: 10.1093/mnras/staa245

Forbes, D. A., & Bridges, T. 2010, Monthly Notices of the Royal Astronomical Society, 404, 1203, DOI: 10.1111/j.1365-2966.2010.16373.x

Fox, W., Longland, R., Marshall, C., & Chaves, F. P. 2024, High Resolution Study of ^{40}Ca to Constrain Potassium Nucleosynthesis in NGC 2419. https://arxiv.org/abs/2401.06754

François, P., Monaco, L., Bonifacio, P., et al. 2016, *A&A*, 588, A7, DOI: 10.1051/0004-6361/201527181

Frank, M. J., Grebel, E. K., & Küpper, A. H. W. 2014, Monthly Notices of the Royal Astronomical Society, 443, 815, DOI: 10.1093/mnras/stu1197

Frebel, A., & Bromm, V. 2012, *ApJ*, 759, 115, DOI: 10.1088/0004-637X/759/2/115

Frebel, A., Ji, A. P., Ezzeddine, R., et al. 2018, ArXiv e-prints. https://arxiv.org/abs/1810.01228

Frebel, A., Kirby, E. N., & Simon, J. D. 2010, *Nature*, 464, 72, DOI: 10.1038/nature08772

Frebel, A., & Norris, J. E. 2015, Annual Review of Astronomy and Astrophysics, 53, 631–688, DOI: 10.1146/annurev-astro-082214-122423

Frebel, A., Simon, J. D., & Kirby, E. N. 2014, *ApJ*, 786, 74, DOI: 10.1088/0004-637X/786/1/74

Freeman, K., & Bland-Hawthorn, J. 2002, *ARA&A*, 40, 487, DOI: 10.1146/annurev.astro.40.060401.093840

Gaia Collaboration, Prusti, T., de Bruijne, J. H. J., et al. 2016, *A&A*, 595, A1, DOI: 10.1051/0004-6361/201629272

Gaia Collaboration, Helmi, A., van Leeuwen, F., et al. 2018, *A&A*, 616, A12, DOI: 10.1051/0004-6361/201832698

Gallart, C., Bernard, E. J., Brook, C. B., et al. 2019, Nature Astronomy, 3, 932, DOI: 10.1038/s41550-019-0829-5

Gao, L., White, S. D. M., Jenkins, A., Stoehr, F., & Springel, V. 2004, Monthly Notices of the Royal Astronomical Society, 355, 819, DOI: 10.1111/j.1365-2966.2004.08360.x

Gatto, M., Ripepi, V., Bellazzini, M., et al. 2021, Research Notes of the American Astronomical Society, 5, 159, DOI: 10.3847/2515-5172/ac14bf

Geha, M., Brown, T. M., Tumlinson, J., et al. 2013, *ApJ*, 771, 29, DOI: 10.1088/0004-637X/771/1/29

Gennaro, M., Geha, M., Tchernyshyov, K., et al. 2018, *ApJ*, 863, 38, DOI: 10.3847/1538-4357/aaceff

Geringer-Sameth, A., Koushiappas, S. M., & Walker, M. 2015, *ApJ*, 801, 74, DOI: 10.1088/0004-637X/801/2/74

Ghasemi, S. M., Rostami-Shirazi, A., Khalaj, P., Zonoozi, A. H., & Haghi, H. 2024, Monthly Notices of the Royal Astronomical Society, 535, 1475, DOI: 10.1093/mnras/stae2212

Gieles, M., Erkal, D., Antonini, F., Balbinot, E., & Peñarrubia, J. 2021, Nature Astronomy, 5, 957, DOI: 10.1038/s41550-021-01392-2

Gilmore, G., Norris, J. E., Monaco, L., et al. 2013, *ApJ*, 763, 61, DOI: 10.1088/0004-637X/763/1/61

Gilmore, G., Wilkinson, M. I., Wyse, R. F. G., et al. 2007, The Astrophysical Journal, 663, 948, DOI: 10.1086/518025

Giribaldi, R. E., Van Eck, S., Merle, T., et al. 2023, *A&A*, 679, A110, DOI: 10.1051/0004-6361/202347208

Gratton, R. G., Carretta, E., & Bragaglia, A. 2012, , 20, 50, DOI: 10.1007/s00159-012-0050-3

Gustafsson, B., Edvardsson, B., Eriksson, K., et al. 2008, *A&A*, 486, 951, DOI: 10.1051/0004-6361:200809724

Hansen, T. T., Simon, J. D., Li, T. S., et al. 2024, Chemical Diversity on Small Scales – Abundance Analysis of the Tucana V Ultra-Faint Dwarf Galaxy. https://arxiv.org/abs/2403.13060

Hansen, T. T., Simon, J. D., Marshall, J. L., et al. 2017, *ApJ*, 838, 44, DOI: 10.3847/1538-4357/aa634a

Hansen, T. T., Marshall, J. L., Simon, J. D., et al. 2020, *ApJ*, 897, 183, DOI: 10.3847/1538-4357/ab9643

Hargis, J. R., Kimmig, B., Willman, B., et al. 2016, *ApJ*, 818, 39, DOI: 10.3847/0004-637X/818/1/39

Harris, W. E. 2010, ArXiv e-prints. https://arxiv.org/abs/1012.3224

Hasselquist, S., Hayes, C. R., Lian, J., et al. 2021, *ApJ*, 923, 172, DOI: 10.3847/1538-4357/ac25f9

Hastings, W. K. 1970, Biometrika, 57, 97, DOI: 10.1093/biomet/57.1.97

Hayes, C. R., Venn, K. A., Waller, F., et al. 2023, arXiv e-prints, arXiv:2306.04804, DOI: 10.48550/arXiv.2306.04804

Heger, A., & Woosley, S. E. 2010, *ApJ*, 724, 341, DOI: 10.1088/0004-637X/724/1/341

Heggie, D. C. 1975, Monthly Notices of the Royal Astronomical Society, 173, 729, DOI: 10.1093/mnras/173.3.729

Heiger, M. E., Li, T. S., Pace, A. B., et al. 2024, *ApJ*, 961, 234, DOI: 10.3847/1538-4357/ad0cf7

Helmi, A. 2008, , 15, 145, DOI: 10.1007/s00159-008-0009-6

Helmi, A., & Tim de Zeeuw, P. 2000, Monthly Notices of the Royal Astronomical Society, 319, 657, DOI: 10.1046/j.1365-8711.2000.03895.x

Helmi, A., White, S. D. M., de Zeeuw, P. T., & Zhao, H. 1999, *Nature*, 402, 53, DOI: 10.1038/46980

Hilker, M., Baumgardt, H., Sollima, A., & Bellini, A. 2020, in IAU Symposium, Vol. 351, Star Clusters: From the Milky Way to the Early Universe, ed. A. Bragaglia, M. Davies, A. Sills, & E. Vesperini, 451–454, DOI: 10.1017/S1743921319006823

Hills, J. G. 1975, *AJ*, 80, 809, DOI: 10.1086/111815

Honda, S., Aoki, W., Ishimaru, Y., Wanajo, S., & Ryan, S. G. 2006, The Astrophysical Journal, 643, 1180, DOI: 10.1086/503195

Hunt, L. K., Annibali, F., Cuillandre, J. C., et al. 2024, arXiv e-prints, arXiv:2405.13499, DOI: 10.48550/arXiv.2405.13499

Ibata, R., Irwin, M., Lewis, G. F., & Stolte, A. 2001, , 547, L133, DOI: 10.1086/318894

Iliadis, C., Karakas, A. I., Prantzos, N., Lattanzio, J. C., & Doherty, C. L. 2016, *ApJ*, 818, 98, DOI: 10.3847/0004-637X/818/1/98

Ishigaki, M. N., Aoki, W., Arimoto, N., & Okamoto, S. 2014, *A&A*, 562, A146, DOI: 10.1051/0004-6361/201322796

Jenkins, A., Frenk, C. S., White, S. D. M., et al. 2001, Monthly Notices of the Royal Astronomical Society, 321, 372, DOI: 10.1046/j.1365-8711.2001.04029.x

Jenkins, S. A., Li, T. S., Pace, A. B., et al. 2021, *ApJ*, 920, 92, DOI: 10.3847/1538-4357/ac1353

Jensen, J., Hayes, C. R., Sestito, F., et al. 2024, *MNRAS*, 527, 4209, DOI: 10.1093/mnras/stad3322

Jensen, J., Thomas, G., McConnachie, A. W., et al. 2021, *MNRAS*, 507, 1923, DOI: 10.1093/mnras/stab2325

Jeon, M., Besla, G., & Bromm, V. 2021, *MNRAS*, 506, 1850, DOI: 10.1093/mnras/stab1771

Jerjen, H., Conn, B., Kim, D., & Schirmer, M. 2018a, arXiv e-prints, arXiv:1809.02259, DOI: 10.48550/arXiv.1809.02259

—. 2018b, arXiv e-prints, arXiv:1809.02259, DOI: 10.48550/arXiv.1809.02259

Ji, A. P., Frebel, A., & Bromm, V. 2015, *MNRAS*, 454, 659, DOI: 10.1093/mnras/stv2052

Ji, A. P., Frebel, A., Ezzeddine, R., & Casey, A. R. 2016, , 832, L3, DOI: 10.3847/2041-8205/832/1/L3

Ji, A. P., Simon, J. D., Frebel, A., Venn, K. A., & Hansen, T. T. 2019, *ApJ*, 870, 83, DOI: 10.3847/1538-4357/aaf3bb

Ji, A. P., Li, T. S., Hansen, T. T., et al. 2020a, *AJ*, 160, 181, DOI: 10.3847/1538-3881/abacb6

—. 2020b, *AJ*, 160, 181, DOI: 10.3847/1538-3881/abacb6

Johnston, K. V., Bullock, J. S., Sharma, S., et al. 2008, *ApJ*, 689, 936, DOI: 10.1086/592228

Kalari, V. M., Diaz, R. J., Robertson, G., et al. 2024, *AJ*, 168, 208, DOI: 10.3847/1538-3881/ad72ed

Kielty, C. L., Venn, K. A., Sestito, F., et al. 2021, *MNRAS*, 506, 1438, DOI: 10.1093/mnras/stab1783

Kim, D., & Jerjen, H. 2015, The Astrophysical Journal, 799, 73, DOI: 10.1088/0004-637x/799/1/73

Kim, D., Jerjen, H., Mackey, D., Da Costa, G. S., & Milone, A. P. 2016, *ApJ*, 820, 119, DOI: 10.3847/0004-637X/820/2/119

Kim, D., Jerjen, H., Milone, A. P., Mackey, D., & Da Costa, G. S. 2015a, *ApJ*, 803, 63, DOI: 10.1088/0004-637X/803/2/63

—. 2015b, *ApJ*, 803, 63, DOI: 10.1088/0004-637X/803/2/63

Kirby, E. N., Boylan-Kolchin, M., Cohen, J. G., et al. 2013a, *ApJ*, 770, 16, DOI: 10.1088/0004-637X/770/1/16

Kirby, E. N., Cohen, J. G., Guhathakurta, P., et al. 2013b, *ApJ*, 779, 102, DOI: 10.1088/0004-637X/779/2/102

Kirby, E. N., Cohen, J. G., Simon, J. D., et al. 2017, The Astrophysical Journal, 838, 83, DOI: 10.3847/1538-4357/aa6570

Kirby, E. N., Ji, A. P., & Kovalev, M. 2023, The Astrophysical Journal, 958, 45, DOI: 10.3847/1538-4357/acf309

Kirby, E. N., Simon, J. D., & Cohen, J. G. 2015, *ApJ*, 810, 56, DOI: 10.1088/0004-637X/810/1/56

Kobayashi, C., Karakas, A. I., & Lugaro, M. 2020, *ApJ*, 900, 179, DOI: 10.3847/1538-4357/abae65

Kobayashi, C., Umeda, H., Nomoto, K., Tominaga, N., & Ohkubo, T. 2006, *ApJ*, 653, 1145, DOI: 10.1086/508914

Koch, A. 2009, Astronomische Nachrichten, 330, 675, DOI: 10.1002/asna.200911231

Koch, A., McWilliam, A., Grebel, E. K., Zucker, D. B., & Belokurov, V. 2008, , 688, L13, DOI: 10.1086/595001

Koposov, S., de Jong, J. T. A., Belokurov, V., et al. 2007, The Astrophysical Journal, 669, DOI: 10.1086/521422

Koposov, S. E., Yoo, J., Rix, H.-W., et al. 2009, *ApJ*, 696, 2179, DOI: 10.1088/0004-637X/696/2/2179

Kravtsov, A., & Manwadkar, V. 2022, Monthly Notices of the Royal Astronomical Society, 514, 2667, DOI: 10.1093/mnras/stac1439

Kravtsov, A. V., & Gnedin, O. Y. 2005, *ApJ*, 623, 650, DOI: 10.1086/428636

Kruijssen, J. M. D. 2015, *MNRAS*, 454, 1658, DOI: 10.1093/mnras/stv2026

Labrie, K., Simpson, C., Cardenes, R., et al. 2023, Research Notes of the American Astronomical Society, 7, 214, DOI: 10.3847/2515-5172/ad0044

Laevens, B. P. M., Martin, N. F., Bernard, E. J., et al. 2015, *ApJ*, 813, 44, DOI: 10.1088/0004-637X/813/1/44

Lamers, H. J. G. L. M., Baumgardt, H., & Gieles, M. 2010, Monthly Notices of the Royal Astronomical Society, 409, 305, DOI: 10.1111/j.1365-2966.2010.17309.x

Larsen, S. S., Romanowsky, A. J., Brodie, J. P., & Wasserman, A. 2020, Science, 370, 970–973, DOI: 10.1126/science.abb1970

Leaman, R. 2012, *AJ*, 144, 183, DOI: 10.1088/0004-6256/144/6/183

Leaman, R., VandenBerg, D. A., & Mendel, J. T. 2013, Monthly Notices of the Royal Astronomical Society, 436, 122, DOI: 10.1093/mnras/stt1540

Li, H., Tan, K., & Zhao, G. 2018, *ApJS*, 238, 16, DOI: 10.3847/1538-4365/aada4a

Li, T. S., Simon, J. D., Pace, A. B., et al. 2018a, The Astrophysical Journal, 857, 145, DOI: 10.3847/1538-4357/aab666

Li, T. S., Simon, J. D., Kuehn, K., et al. 2018b, The Astrophysical Journal, 866, 22, DOI: 10.3847/1538-4357/aadf91

Li, T. S., Koposov, S. E., Zucker, D. B., et al. 2019, *MNRAS*, 490, 3508, DOI: 10.1093/mnras/stz2731

Li, T. S., Ji, A. P., Pace, A. B., et al. 2022a, *ApJ*, 928, 30, DOI: 10.3847/1538-4357/ac46d3

—. 2022b, *ApJ*, 928, 30, DOI: 10.3847/1538-4357/ac46d3

Lind, K., Asplund, M., Barklem, P. S., & Belyaev, A. K. 2011, *A&A*, 528, A103, DOI: 10.1051/0004-6361/201016095

Longeard, N., Martin, N., Ibata, R. A., et al. 2019, Monthly Notices of the Royal Astronomical Society, 490, 1498–1508, DOI: 10.1093/mnras/stz2592

Longeard, N., Martin, N., Starkenburg, E., et al. 2018, Monthly Notices of the Royal Astronomical Society, 480, 2609, DOI: 10.1093/mnras/sty1986

Longeard, N., Martin, N., Starkenburg, E., et al. 2020, *MNRAS*, 491, 356, DOI: 10.1093/mnras/stz2854

Longeard, N., Martin, N., Starkenburg, E., et al. 2020, Monthly Notices of the Royal Astronomical Society, 491, 356–377, DOI: 10.1093/mnras/stz2854

Longeard, N., Martin, N., Ibata, R. A., et al. 2021, Monthly Notices of the Royal Astronomical Society, 503, 2754–2762, DOI: 10.1093/mnras/stab604

Lucatello, S., Beers, T. C., Christlieb, N., et al. 2006, The Astrophysical Journal, 652, L37, DOI: 10.1086/509780

Lucchesi, R., Lardo, C., Jablonka, P., et al. 2022, *MNRAS*, 511, 1004, DOI: 10.1093/mnras/stab3721

Lucchesi, R., Jablonka, P., Skúladóttir, Á., et al. 2024, *A&A*, 686, A266, DOI: 10.1051/0004-6361/202348093

Lujan, N., Gebhardt, K., Anantua, R., et al. 2025, The "Dark-Matter Dominated" Galaxy Segue 1 Modeled with a Black Hole and no Dark Halo. https://arxiv.org/abs/2505.06198

Luque, E., Pieres, A., Santiago, B., et al. 2017, *MNRAS*, 468, 97, DOI: 10.1093/mnras/stx405

Luque, E., Santiago, B., Pieres, A., et al. 2018, *MNRAS*, 478, 2006, DOI: 10.1093/mnras/sty1039

Maccarone, T. J., Kundu, A., Zepf, S. E., & Rhode, K. L. 2007, *Nature*, 445, 183, DOI: 10.1038/nature05434

Mackey, A. D., & van den Bergh, S. 2005, *MNRAS*, 360, 631, DOI: 10.1111/j.1365-2966.2005.09080.x

Madrid, J. P., Leigh, N. W. C., Hurley, J. R., & Giersz, M. 2017, Monthly Notices of the Royal Astronomical Society, 470, 1729, DOI: 10.1093/mnras/stx1350

Majewski, S. R., Schiavon, R. P., Frinchaboy, P. M., et al. 2017, The Astronomical Journal, 154, 94, DOI: 10.3847/1538-3881/aa784d

Malhan, K., & Ibata, R. A. 2018, *MNRAS*, 477, 4063, DOI: 10.1093/mnras/sty912

Malhan, K., Ibata, R. A., Sharma, S., et al. 2022, The Astrophysical Journal, 926, 107, DOI: 10.3847/1538-4357/ac4d2a

Mallinson, J. W. E., Lind, K., Amarsi, A. M., et al. 2022, *A&A*, 668, A103, DOI: 10.1051/0004-6361/202244788

Mallinson, J. W. E., Lind, K., Amarsi, A. M., & Youakim, K. 2024, *A&A*, 687, A5, DOI: 10.1051/0004-6361/202347698

Manwadkar, V., & Kravtsov, A. 2024

Manwadkar, V., & Kravtsov, A. V. 2022, *MNRAS*, 516, 3944, DOI: 10.1093/mnras/stac2452

Manwadkar, V., & Kravtsov, A. V. 2022, Monthly Notices of the Royal Astronomical Society, 516, 3944, DOI: 10.1093/mnras/stac2452

Marigo, P., Girardi, L., Bressan, A., et al. 2008, *A&A*, 482, 883, DOI: 10.1051/0004-6361:20078467

Marshall, J. L., Hansen, T., Simon, J. D., et al. 2019, The Astrophysical Journal, 882, 177, DOI: 10.3847/1538-4357/ab3653

Martin, N. F., Ibata, R. A., Collins, M. L. M., et al. 2016a, *ApJ*, 818, 40, DOI: 10.3847/0004-637X/818/1/40

Martin, N. F., Geha, M., Ibata, R. A., et al. 2016b, *MNRAS*, 458, L59, DOI: 10.1093/mnrasl/slw013

Martin, N. F., Jungbluth, V., Nidever, D. L., et al. 2016c, , 830, L10, DOI: 10.3847/2041-8205/830/1/L10

Martin, N. F., Venn, K. A., Aguado, D. S., et al. 2022, *Nature*, 601, 45, DOI: 10.1038/s41586-021-04162-2

Martinez, G. D. 2015, *MNRAS*, 451, 2524, DOI: 10.1093/mnras/stv942

Mashonkina, L., Jablonka, P., Pakhomov, Y., Sitnova, T., & North, P. 2017, *A&A*, 604, A129, DOI: 10.1051/0004-6361/201730779

Mashonkina, L. I., & Belyaev, A. K. 2019, Astronomy Letters, 45, 341, DOI: 10.1134/S1063773719060033

Massari, D., Posti, L., Helmi, A., Fiorentino, G., & Tolstoy, E. 2017, *A&A*, 598, L9, DOI: 10.1051/0004-6361/201630174

Massari, D., Koppelman, H. H., & Helmi, A. 2019, AA, 630, L4, DOI: 10.1051/0004-6361/201936135

Mau, S., Drlica-Wagner, A., Bechtol, K., et al. 2019, *ApJ*, 875, 154, DOI: 10.3847/1538-4357/ab0bb8

Mau, S., Cerny, W., Pace, A. B., et al. 2020, *ApJ*, 890, 136, DOI: 10.3847/1538-4357/ab6c67

McConnachie, A. W. 2012, *AJ*, 144, 4, DOI: 10.1088/0004-6256/144/1/4

McConnachie, A. W., & Côté, P. 2010, , 722, L209, DOI: 10.1088/2041-8205/722/2/L209

McConnachie, A. W., & Venn, K. A. 2020, *AJ*, 160, 124, DOI: 10.3847/1538-3881/aba4ab

McConnachie, A. W., Hayes, C. R., Robertson, J. G., et al. 2024, , 136, 035001, DOI: 10.1088/1538-3873/ad1ed4

McKenzie, M., & Bekki, K. 2021, *MNRAS*, 507, 834, DOI: 10.1093/mnras/stab2171

Mészáros, S., Martell, S. L., Shetrone, M., et al. 2015, The Astronomical Journal, 149, 153

Meylan, G., & Heggie, D. C. 1997, , 8, 1, DOI: 10.1007/s001590050008

Monty, S., Venn, K. A., Lane, J. M. M., Lokhorst, D., & Yong, D. 2020, *MNRAS*, 497, 1236, DOI: 10.1093/mnras/staa1995

Monty, S., Belokurov, V., Sanders, J. L., et al. 2024, *MNRAS*, 533, 2420, DOI: 10.1093/mnras/stae1895

Moody, K., & Sigurdsson, S. 2008, The Astrophysical Journal, 690, 1370–1377, DOI: 10.1088/0004-637x/690/2/1370

Moore, B., Ghigna, S., Governato, F., et al. 1999, The Astrophysical Journal, 524, L19, DOI: 10.1086/312287

Muñoz, R. R., Geha, M., Côté, P., et al. 2012, , 753, L15, DOI: 10.1088/2041-8205/753/1/L15

Mucciarelli, A., & Bellazzini, M. 2020, Research Notes of the American Astronomical Society, 4, 52, DOI: 10.3847/2515-5172/ab8820

Mucciarelli, A., Bellazzini, M., Ibata, R., et al. 2012, *MNRAS*, 426, 2889, DOI: 10.1111/j.1365-2966.2012.21847.x

Mutlu-Pakdil, B., Sand, D. J., Carlin, J. L., et al. 2018, The Astrophysical Journal, 863, 25, DOI: 10.3847/1538-4357/aacd0e

Mutlu-Pakdil, B., Sand, D. J., Walker, M. G., et al. 2019, *ApJ*, 885, 53, DOI: 10.3847/1538-4357/ab45ec

Myeong, G. C., Evans, N. W., Belokurov, V., Sand ers, J. L., & Koposov, S. E. 2018, , 863, L28, DOI: 10.3847/2041-8213/aad7f7

Nadler, E. O. 2025, The Astrophysical Journal Letters, 983, L23, DOI: 10.3847/2041-8213/adbc6e

Nadler, E. O., Drlica-Wagner, A., Bechtol, K., et al. 2021, , 126, 091101, DOI: 10.1103/PhysRevLett.126.091101

Nagasawa, D. Q., Marshall, J. L., Li, T. S., et al. 2018, The Astrophysical Journal, 852, 99, DOI: 10.3847/1538-4357/aaa01d

Navarro, J. F., Frenk, C. S., & White, S. D. M. 1996, *ApJ*, 462, 563, DOI: 10.1086/177173

Niederste-Ostholt, M., Belokurov, V., Evans, N. W., et al. 2010, Monthly Notices of the Royal Astronomical Society: Letters, 408, L66, DOI: 10.1111/j.1745-3933.2010.00931.x

Nissen, P. E., & Schuster, W. J. 2010, *A&A*, 511, L10, DOI: 10.1051/0004-6361/200913877

Nomoto, K., Kobayashi, C., & Tominaga, N. 2013, *ARA&A*, 51, 457, DOI: 10.1146/annurev-astro-082812-140956

Norris, J. E., Wyse, R. F. G., Gilmore, G., et al. 2010, *ApJ*, 723, 1632, DOI: 10.1088/0004-637X/723/2/1632

Norris, J. E., Yong, D., Venn, K. A., et al. 2017, *ApJS*, 230, 28, DOI: 10.3847/1538-4365/aa755e

Norris, J. E., Yong, D., Bessell, M. S., et al. 2013, *ApJ*, 762, 28, DOI: 10.1088/0004-637X/762/1/28

Ortolani, S., Bica, E., & Barbuy, B. 2013, Monthly Notices of the Royal Astronomical Society, 433, 1966, DOI: 10.1093/mnras/stt865

O'Leary, J. A., Steinwandel, U. P., Moster, B. P., Martin, N., & Naab, T. 2023, Monthly Notices of the Royal Astronomical Society, 520, 897, DOI: 10.1093/mnras/stad166

Pace, A. B., Erkal, D., & Li, T. S. 2022, arXiv e-prints, arXiv:2205.05699. https://arxiv.org/abs/2205.05699

Pace, A. B., Kaplinghat, M., Kirby, E., et al. 2020, *MNRAS*, 495, 3022, DOI: 10.1093/mnras/staa1419

Palma, T., Gramajo, L. V., Clariá, J. J., et al. 2016, *A&A*, 586, A41, DOI: 10.1051/0004-6361/201527305

Parker, R. J., & Goodwin, S. P. 2015, Monthly Notices of the Royal Astronomical Society, 449, 3381, DOI: 10.1093/mnras/stv539

Patel, E., Kallivayalil, N., Garavito-Camargo, N., et al. 2020, The Astrophysical Journal, 893, 121, DOI: 10.3847/1538-4357/ab7b75

Paust, N., Wilson, D., & van Belle, G. 2014, *AJ*, 148, 19, DOI: 10.1088/0004-6256/148/1/19

Peñarrubia, J., Errani, R., Vitral, E., & Walker, M. G. 2025, arXiv e-prints, arXiv:2506.03904, DOI: 10.48550/arXiv.2506.03904

Pereira-Wilson, M., Navarro, J. F., Benítez-Llambay, A., & Santos-Santos, I. 2022, Monthly Notices of the Royal Astronomical Society, 519, 1425, DOI: 10.1093/mnras/stac3633

Peuten, M., Zocchi, A., Gieles, M., Gualandris, A., & Hénault-Brunet, V. 2016, Monthly Notices of the Royal Astronomical Society, 462, 2333, DOI: 10.1093/mnras/stw1726

Pfeffer, J., Lardo, C., Bastian, N., Saracino, S., & Kamann, S. 2021, *MNRAS*, 500, 2514, DOI: 10.1093/mnras/staa3407

Piatti, A. E., & Lucchini, S. 2022, *MNRAS*, 515, 4005, DOI: 10.1093/mnras/stac1980

Placco, V. M., Frebel, A., Beers, T. C., & Stancliffe, R. J. 2014, *ApJ*, 797, 21, DOI: 10.1088/0004-637X/797/1/21

Placco, V. M., Sneden, C., Roederer, I. U., et al. 2021, Research Notes of the American Astronomical Society, 5, 92, DOI: 10.3847/2515-5172/abf651

Prantzos, N., Abia, C., Limongi, M., Chieffi, A., & Cristallo, S. 2018, *MNRAS*, 476, 3432, DOI: 10.1093/mnras/sty316

Ramírez, I., Meléndez, J., Bean, J., et al. 2014, *A&A*, 572, A48, DOI: 10.1051/0004-6361/201424244

Read, J. I., Pontzen, A. P., & Viel, M. 2006, *MNRAS*, 371, 885, DOI: 10.1111/j.1365-2966.2006.10720.x

Reggiani, H., Amarsi, A. M., Lind, K., et al. 2019, *A&A*, 627, A177, DOI: 10.1051/0004-6361/201935156

Ritter, C., Andrassy, R., Côté, B., et al. 2018, *MNRAS*, 474, L1, DOI: 10.1093/mnrasl/slx126

Roederer, I. U. 2013, *AJ*, 145, 26, DOI: 10.1088/0004-6256/145/1/26

Roederer, I. U., & Kirby, E. N. 2014, *MNRAS*, 440, 2665, DOI: 10.1093/mnras/stu491

Roederer, I. U., Preston, G. W., Thompson, I. B., et al. 2014, The Astronomical Journal, 147, 136. http://stacks.iop.org/1538-3881/147/i=6/a=136

Roederer, I. U., Sakari, C. M., Placco, V. M., et al. 2018, *ApJ*, 865, 129, DOI: 10.3847/1538-4357/aadd92

Roederer, I. U., Lawler, J. E., Den Hartog, E. A., et al. 2022, *ApJS*, 260, 27, DOI: 10.3847/1538-4365/ac5cbc

Rossi, M., Salvadori, S., Skúladóttir, , & Vanni, I. 2023, Monthly Notices of the Royal Astronomical Society: Letters, 522, L1–L5, DOI: 10.1093/mnrasl/slad029

Sacchi, E., Richstein, H., Kallivayalil, N., et al. 2021, The Astrophysical Journal Letters, 920, L19, DOI: 10.3847/2041-8213/ac2aa3

Sakari, C. M., Venn, K. A., Irwin, M., et al. 2011, The Astrophysical Journal, 740, 106

Salvadori, S., Skúladóttir, Á., & Tolstoy, E. 2015, *MNRAS*, 454, 1320, DOI: 10.1093/mnras/stv1969

Santos-Santos, I. M. E., Sales, L. V., Fattahi, A., & Navarro, J. F. 2022, Monthly Notices of the Royal Astronomical Society, 515, 3685, DOI: 10.1093/mnras/stac2057

Schaye, J., Crain, R. A., Bower, R. G., et al. 2015, *MNRAS*, 446, 521, DOI: 10.1093/mnras/stu2058

Schiavon, R. P., Phillips, S. G., Myers, N., et al. 2023, The APOGEE Value Added Catalogue of Galactic globular cluster stars. https://arxiv.org/abs/2310.07764

Schlafly, E. F., & Finkbeiner, D. P. 2011, *ApJ*, 737, 103, DOI: 10.1088/0004-637X/737/2/103

Schultz, G. V., & Wiemer, W. 1975, *A&A*, 43, 133

Sestito, F., Roediger, J., Navarro, J. F., et al. 2023a, *MNRAS*, 523, 123, DOI: 10.1093/mnras/stad1417

Sestito, F., Zaremba, D., Venn, K. A., et al. 2023b, arXiv e-prints, arXiv:2301.13214, DOI: 10.48550/arXiv.2301.13214

Sestito, F., Hayes, C. R., Venn, K. A., et al. 2024, *MNRAS*, 528, 4838, DOI: 10.1093/mnras/stae244

Shanks, T., Metcalfe, N., Chehade, B., et al. 2015

Simmerer, J., Sneden, C., Cowan, J. J., et al. 2004, *ApJ*, 617, 1091, DOI: 10.1086/424504

Simon, J. D. 2019a, *ARA&A*, 57, 375, DOI: 10.1146/annurev-astro-091918-104453

—. 2019b, *ARA&A*, 57, 375, DOI: 10.1146/annurev-astro-091918-104453

Simon, J. D., Frebel, A., McWilliam, A., Kirby, E. N., & Thompson, I. B. 2010, *ApJ*, 716, 446, DOI: 10.1088/0004-637X/716/1/446

Simon, J. D., & Geha, M. 2007, *ApJ*, 670, 313, DOI: 10.1086/521816

Simon, J. D., Geha, M., Minor, Q. E., et al. 2011, *ApJ*, 733, 46, DOI: 10.1088/0004-637X/733/1/46

Simon, J. D., Drlica-Wagner, A., Li, T. S., et al. 2015, *ApJ*, 808, 95, DOI: 10.1088/0004-637X/808/1/95

Simon, J. D., Li, T. S., Drlica-Wagner, A., et al. 2017, *ApJ*, 838, 11, DOI: 10.3847/1538-4357/aa5be7

Simon, J. D., Li, T. S., Erkal, D., et al. 2020, The Astrophysical Journal, 892, 137, DOI: 10.3847/1538-4357/ab7ccb

Simon, J. D., Li, T. S., Ji, A. P., et al. 2024, *ApJ*, 976, 256, DOI: 10.3847/1538-4357/ad85dd

Simpson, J. D. 2018, *MNRAS*, 477, 4565, DOI: 10.1093/mnras/sty847

Sitnova, T. M., Mashonkina, L. I., Tatarnikov, A. M., et al. 2021a, *MNRAS*, 504, 1183, DOI: 10.1093/mnras/stab786

—. 2021b, *MNRAS*, 504, 1183, DOI: 10.1093/mnras/stab786

Smith, G. H. 1985, *ApJ*, 298, 249, DOI: 10.1086/163603

Smith, G. H., Sneden, C., & Kraft, R. P. 2002, *AJ*, 123, 1502, DOI: 10.1086/338855

Smith, S. E. T., Jensen, J., Roediger, J., et al. 2023, *AJ*, 166, 76, DOI: 10.3847/1538-3881/acdd77

Smith, S. E. T., Cerny, W., Hayes, C. R., et al. 2024, *ApJ*, 961, 92, DOI: 10.3847/1538-4357/ad0d9f

Sneden, C., Cowan, J. J., & Gallino, R. 2008, *ARA&A*, 46, 241, DOI: 10.1146/annurev.astro.46.060407.145207

Sneden, C., Kraft, R. P., Shetrone, M. D., et al. 1997, The Astronomical Journal, 114, 1964

Sneden, C., Pilachowski, C. A., & Kraft, R. P. 2000, The Astronomical Journal, 120, 1351

Sneden, C. A. 1973, PhD thesis, THE UNIVERSITY OF TEXAS AT AUSTIN.

Sobeck, J. S., Kraft, R. P., Sneden, C., et al. 2011, *AJ*, 141, 175, DOI: 10.1088/0004-6256/141/6/175

Sollima, A., Beccari, G., Ferraro, F. R., Fusi Pecci, F., & Sarajedini, A. 2007, Monthly Notices of the Royal Astronomical Society, 380, 781, DOI: 10.1111/j.1365-2966.2007.12116.x

Sollima, A., Martínez-Delgado, D., Valls-Gabaud, D., & Peñarrubia, J. 2011, *ApJ*, 726, 47, DOI: 10.1088/0004-637X/726/1/47

Spite, M., Spite, F., François, P., et al. 2018, *A&A*, 617, A56, DOI: 10.1051/0004-6361/201833548

Spitzer, L. 1987, Dynamical evolution of globular clusters

Spurzem, R., & Kamlah, A. 2023, Living Reviews in Computational Astrophysics, 9, 3, DOI: 10.1007/s41115-023-00018-w

Starkenburg, E., Hill, V., Tolstoy, E., et al. 2010, *A&A*, 513, A34, DOI: 10.1051/0004-6361/200913759

—. 2013, *A&A*, 549, A88, DOI: 10.1051/0004-6361/201220349

Strader, J., Chomiuk, L., Maccarone, T. J., Miller-Jones, J. C. A., & Seth, A. C. 2012, Nature, 490, 71, DOI: 10.1038/nature11490

Szigeti, L., Mészáros, S., Smith, V. V., et al. 2018, *MNRAS*, 474, 4810, DOI: 10.1093/mnras/stx3027

Tarumi, Y., Suda, T., van de Voort, F., et al. 2021, Monthly Notices of the Royal Astronomical Society, 505, 3755, DOI: 10.1093/mnras/stab1487

Tinker, J., Kravtsov, A. V., Klypin, A., et al. 2008, The Astrophysical Journal, 688, 709, DOI: 10.1086/591439

Tolstoy, E., Hill, V., & Tosi, M. 2009, *ARA&A*, 47, 371, DOI: 10.1146/annurev-astro-082708-101650

Torrealba, G., Belokurov, V., & Koposov, S. E. 2019, Monthly Notices of the Royal Astronomical Society, 484, 2181–2197, DOI: 10.1093/mnras/stz071

Torrealba, G., Koposov, S. E., Belokurov, V., et al. 2016, *MNRAS*, 463, 712, DOI: 10.1093/mnras/stw2051

Valenzuela, L. M., Remus, R.-S., McKenzie, M., & Forbes, D. A. 2024, *A&A*, 687, A104, DOI: 10.1051/0004-6361/202348010

VandenBerg, D. A., Brogaard, K., Leaman, R., & Casagrande, L. 2013, *ApJ*, 775, 134, DOI: 10.1088/0004-637X/775/2/134

Vargas, L. C., Geha, M., Kirby, E. N., & Simon, J. D. 2013, *ApJ*, 767, 134, DOI: 10.1088/0004-637X/767/2/134

Venn, K., Yuan, Z., Hayes, C.R., et al. 2025

Venn, K. A., Irwin, M., Shetrone, M. D., et al. 2004, *AJ*, 128, 1177, DOI: 10.1086/422734

Venn, K. A., Starkenburg, E., Malo, L., Martin, N., & Laevens, B. P. M. 2017a, *MNRAS*, 466, 3741, DOI: 10.1093/mnras/stw3198

—. 2017b, *MNRAS*, 466, 3741, DOI: 10.1093/mnras/stw3198

Venn, K. A., Shetrone, M. D., Irwin, M. J., et al. 2012, *ApJ*, 751, 102, DOI: 10.1088/0004-637X/751/2/102

Ventura, P., D'Antona, F., Di Criscienzo, M., et al. 2012, , 761, L30, DOI: 10.1088/2041-8205/761/2/L30

Vogelsberger, M., Genel, S., Springel, V., et al. 2014, *MNRAS*, 444, 1518, DOI: 10.1093/mnras/stu1536

Walker, M. G., Caldwell, N., Mateo, M., et al. 2023, *ApJS*, 268, 19, DOI: 10.3847/1538-4365/acdd79

Walker, M. G., & Peñarrubia, J. 2011, *ApJ*, 742, 20, DOI: 10.1088/0004-637X/742/1/20

Walker, M. G., Mateo, M., Olszewski, E. W., et al. 2016, *ApJ*, 819, 53, DOI: 10.3847/0004-637X/819/1/53

Waller, F., Venn, K. A., Sestito, F., et al. 2023, *MNRAS*, 519, 1349, DOI: 10.1093/mnras/stac3563

Wang, L. 2020, Monthly Notices of the Royal Astronomical Society, 491, 2413, DOI: 10.1093/mnras/stz3179

Wang, L., Gieles, M., Baumgardt, H., et al. 2024, *MNRAS*, 527, 7495, DOI: 10.1093/mnras/stad3657

Weatherford, N. C., Chatterjee, S., Rodriguez, C. L., & Rasio, F. A. 2018, The Astrophysical Journal, 864, 13, DOI: 10.3847/1538-4357/aad63d

Weatherford, N. C., Kıroğlu, F., Fragione, G., et al. 2023, The Astrophysical Journal, 946, 104, DOI: 10.3847/1538-4357/acbcc1

Webber, K. B., Hansen, T. T., Marshall, J. L., et al. 2023, *ApJ*, 959, 141, DOI: 10.3847/1538-4357/ad0385

Weisz, D. R., Koposov, S. E., Dolphin, A. E., et al. 2016, *ApJ*, 822, 32, DOI: 10.3847/0004-637X/822/1/32

White, S. D. M., & Rees, M. J. 1978, *MNRAS*, 183, 341, DOI: 10.1093/mnras/183.3.341

Willman, B., & Strader, J. 2012, *AJ*, 144, 76, DOI: 10.1088/0004-6256/144/3/76

Wolf, J., Martinez, G. D., Bullock, J. S., et al. 2010, *MNRAS*, 406, 1220, DOI: 10.1111/j.1365-2966.2010.16753.x

Worley, C. C., Hill, V., Sobeck, J., & Carretta, E. 2013, *A&A*, 553, A47, DOI: 10.1051/0004-6361/201321097

Wu, W., Kroupa, P., & Pflamm-Altenburg, J. 2024, Monthly Notices of the Royal Astronomical Society, 530, 5155, DOI: 10.1093/mnras/stae1174

Wu, W., Wang, L., Liu, S., et al. 2025, arXiv e-prints, arXiv:2504.20392, DOI: 10.48550/arXiv.2504.20392

Wu, W., & Zhao, G. 2021, The Astrophysical Journal, 908, 224, DOI: 10.3847/1538-4357/abd6b8

Yong, D., Norris, J. E., Bessell, M. S., et al. 2013, *ApJ*, 762, 26, DOI: 10.1088/0004-637X/762/1/26

Yong, D., Da Costa, G. S., Bessell, M. S., et al. 2021, *MNRAS*, 507, 4102, DOI: 10.1093/mnras/stab2001

York, D. G. 2000, Astron.J., 120, 1579, DOI: 10.1086/301513

Yu, L., Li, J., Wang, J., et al. 2024, Research in Astronomy and Astrophysics, 24, 035017, DOI: 10.1088/1674-4527/ad1047

Yuan, Z., Martin, N. F., Ibata, R. A., et al. 2022, arXiv e-prints, arXiv:2203.02512. https://arxiv.org/abs/2203.02512

Zhou, Y., Li, X., Huang, Y., & Zhang, H. 2023, The Astrophysical Journal, 946, 73, DOI: 10.3847/1538-4357/acadd9

Zonoozi, A. H., Rabiee, M., Haghi, H., & Kroupa, P. 2024, *ApJ*, 975, 266, DOI: 10.3847/1538-4357/ad7953